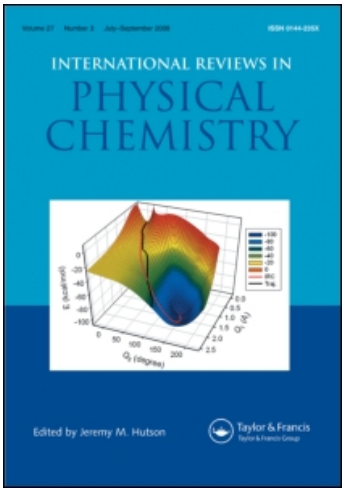

International Reviews in Physical Chemistry
Publication details, including instructions for authors and subscription information:
http://www.informaworld.com/smpp/title~content=t713724383

Multiphoton spectroscopy of NO?Rg (Rg = rare gas) van der Waals systems

Yangsoo Kim; Henning Meyer

Online publication date: 26 November 2010

To cite this Article Kim, Yangsoo and Meyer, Henning(2001) 'Multiphoton spectroscopy of NO?Rg (Rg = rare gas) van der Waals systems', International Reviews in Physical Chemistry, 20: 3, 219 — 282
To link to this Article: DOI: 10.1080/713863631
URL: http://dx.doi.org/10.1080/713863631

INT. REVIEWS IN PHYSICAL CHEMISTRY, 2001, VOL. 20, NO. 3, 219–282

Multiphoton spectroscopy of NO–Rg (Rg = rare gas) van der Waals systems

YANGSOO KIM and HENNING MEYER†

Department of Physics and Astronomy, The University of Georgia, Athens, GA 30602, USA

The spectroscopic characterization of the electronic ground and excited state interactions of NO with different rare gases is reviewed. In its electronic ground state, the NO molecule continues to serve as one of the most important benchmark systems for investigating van der Waals interactions involving open shell molecules. Combining high resolution infrared excitation with resonance enhanced multiphoton ionization (REMPI) detection, bound intermolecular bend–stretch levels have been detected for the complexes NO–Ar and NO–Ne for the first time. In parallel with these new experimental advances, new high-level *ab-initio* potential energy surfaces have been calculated very recently for several NO–Rg (Rg = rare gas) systems. Predictions for the bound states based on these potentials are in excellent agreement with the high resolution infrared spectra for NO–Ar and NO–Ne, demonstrating the great accuracy achieved with current *ab initio* methods. The large number of excited electronic states of NO provides ideal opportunities for studying molecular interactions in different excited states. The low lying Rydberg states are especially interesting because the Rydberg electron can reside in an orbital whose size is comparable with or larger than the van der Waals radius of the complexed atom. The existing set of experimental data on Rydberg states with $n = 3(l = 0, 1, 2)$ and $n = 4(l = 0)$ are reviewed critically. The excited states have been investigated employing mainly REMPI spectroscopy. The data provide detailed information about the bound levels of the associated intermolecular surfaces. Most of the work has concentrated on the complexes with Ar and Ne. Additional data for the states $\tilde{A}\,^2\Sigma$ and $\tilde{C}\,^2\Pi$ are available for complexes with Kr and Xe.

Contents

† Email: hmeyer@hal.physast.uga.edu

International Reviews in Physical Chemistry ISSN 0144–235X print/ISSN 1366–591X online © 2001 Taylor & Francis Ltd
http://www.tandf.co.uk/journals
DOI: 10.1080/01442350110036785

1. Introduction

The spectroscopy and dynamics of van der Waals systems have been the subject of intense research over the past decades. The interest in clusters stems from the prospect of understanding in detail the transition from the gas to the condensed phase. Properties of clusters due to their finite size are of particular interest. For many systems, cluster properties can be explained to a large extent in terms of pairwise interactions while three-body and other higher-order terms contribute only small corrections. Several excellent review articles have been published in recent years summarizing the progress [1–5]. While the emphasis has been mainly on complexes involving closed shell species, a few reviews have reported on systems involving open shell atoms and molecules [6–8]. These complexes are of special interest since most chemically active systems involve atoms or molecules with unpaired electrons. Van der Waals interactions involving open shell species will be most important at long range where chemical forces are relatively weak. Therefore, van der Waals interactions can be important for the entrance channel of a reaction where they can influence its stereodynamics. Systems involving the $^2\Pi$ radicals OH or NO have emerged as important benchmarks for the understanding and quantitative description of the collision dynamics and the bound state structure. Their complexes with rare gas atoms represent two extreme cases: the OH radical represents a system with a triply filled π-orbital. As a hydride, its rotational constant is comparable in magnitude with the intermolecular interaction. Therefore, to a first approximation, we might regard the OH as freely rotating with an approximately linear equilibrium structure. In contrast, NO represents the class of radicals with a single electron occupying an antibonding π^*-orbital. The rare gas complexes of NO are characterized by a near T-shaped configuration. Since the rotational energy of NO is much smaller than the binding energy of the complex, some aspects of the energy level pattern of the complex are well described using the concept of a near rigid symmetric top.

In the complex, the electronic degeneracy of the Π-state is lifted giving rise to two adiabatic potential surfaces of A' and A'' reflection symmetry. For systems involving diatoms in $^2\Pi$-states, the difference of the two potential surfaces is responsible for fine-structure changing collisions while the average potential mediates fine-structure conserving collisions. Since the semiclassical trajectory must evolve simultaneously and coherently on both surfaces, quantum interference effects and propensities are observed in the inelastic scattering cross sections. Similarly, the bound state structure

of the corresponding van der Waals complexes can be understood in terms of electrostatic and Coriolis type splittings of the degenerate rotational energy levels. Since the spectroscopy of different rare gas complexes involving the radicals OH and SH has been reviewed very recently [8], we concentrate in this review article on the different spectroscopic results for NO containing complexes.

Two different approaches for studying the interaction between molecules and rare gas atoms have been developed in our laboratory. The methods are complementary in the sense that they aim at exploring different parts of the potential surfaces governed dominantly by either attractive or repulsive interactions. The latter is responsible for the energy transfer in bimolecular collision processes. The associated scattering wavefunctions represent, in the language of quantum mechanics, solutions to the Schrödinger equation for positive energies and, thus, they give rise to the continuous spectrum of the associated Hamiltonian. Sensitive information about the anisotropy in the region of the repulsive wall is accessed in the form of quantum state resolved differential cross-sections. Using resonance enhanced multiphoton ionization (REMPI) for the state specific detection of scattered products in combination with ion time-of-flight (TOF) analysis, we are able to measure state specific angular distributions of the scattered molecules. In the case of a well defined initial state (for example, prepared in the adiabatic molecular beam expansion), fully state resolved differential cross sections can be extracted from the data. In order to enhance the signal levels, we developed the method of counterpropagating pulsed molecular beam scattering. The cylindrical symmetry realized in this set-up, enables us to integrate over the redundant azimuthal scattering angle without losing information about the physically relevant polar scattering angle. The resulting signals are sufficiently intense to employ higher order multiphoton processes such as $(2 + 1)$ REMPI or, in the case of CO, $(3 + 1)$ REMPI for the product detection [9]. Depending on the particular REMPI process employed, the dependence of the scattered intensity on the laser polarization can reveal detailed information about the collision-induced angular momentum alignment. For the first time, partially M-state resolved differential cross sections have been measured for several collision systems involving NH_3 [10–14], CO [9], or NO [15]. Details of the scattering experiments can be found in the original publications and in a recent review article [16].

The bound levels of the corresponding van der Waals complexes are studied through REMPI of the complex using the molecular fragment as a REMPI chromophore. So far this type of spectroscopy has been applied successfully to complexes of the molecules NO or acetaldehyde with different rare gas atoms [17,18]. Since the complexes are generated in a molecular beam expansion, only the vibrational ground state has a significant population and the spectroscopic information is limited to the bound levels of those potential surfaces which correlate with the excited monomer state involved in the REMPI process. In the case of NO containing complexes, we studied several states correlating with the low lying Rydberg states of NO. In particular, band systems involving the states $C\,^2\Pi(v' = 1\text{-}4)$, $F\,^2\Delta$, $E\,^2\Sigma$ and $H\,^2\Sigma$, $H'^2\Pi$ were investigated. Employing an infrared (IR)-REMPI double resonance scheme, we recently succeeded in detecting IR resonances which involve different intermolecular stretch and bend levels of the electronic ground state potential surfaces. In the case of NO, all bands are associated with the excitation of the first overtone of the NO subunit. Although strictly speaking the bound levels probed in these experiments do not belong to the vibrational ground state manifold

($v''_{NO} = 0$), we have strong indications that the levels associated with the ($v''_{NO} = 2$)-manifold are very similar to the ones correlating with the vibrational ground state of NO.

Among the various complexes involving NO, the NO–Ar system has served as the paradigm for understanding and characterizing the interaction of an open shell diatom with a closed shell atom for more than 20 years. The first theoretical study of the van der Waals interaction in its electronic ground state was performed by Nielson, Parker and Pack [19, 20]. These authors applied the electron gas model to calculate the first set of potential energy surfaces. They also emphasized the advantage of working with two adiabatic potential surfaces and thus keeping the electronic degree of freedom instead of introducing a single potential surface with an additional angle dependence [21]. A similar approach was also advocated later by Alexander [22] who showed that the potential surfaces relevant to the collision dynamics can be derived from the two Born–Oppenheimer surfaces in the form of a sum potential and a difference potential [23]. Alexander and co-workers studied extensively the dynamics for collisions of NO with different rare gas atoms and, in this context, the applicability of different decoupling approximations [24–28]. The angular momentum polarization or collision-induced alignment as a result of the bimolecular encounter was also investigated in a series of papers [29, 30]. While most of these earlier studies relied on semiempirical potential surfaces, high-level *ab-initio* calculations throughout the 1990s have produced multi-dimensional surfaces for several NO–rare gas systems [26, 27, 31–34]. Recent spectroscopic and collision studies have confirmed the great accuracy of these potential surfaces [15, 35 36].

Experimentally, the NO+ Ar system has been studied in a variety of collision experiments. Integral cross sections without final state resolution for the scattering of NO from different rare gas partners have been measured by Thuis *et al.* [37, 38]. These measurements established a near T-shaped equilibrium structure of the complex and they provided first quantitative information about the equilibrium distance. High-resolution differential cross-sections for the scattering of NO from He and Ar were reported by Keil *et al.* [39] and Casavecchia and co-workers [40, 41]. The latter workers used the observed damping of the diffraction oscillations in the total differential scattering cross section to determine an effective anisotropy for the interaction potential. Employing laser-induced fluorescence detection in combination with IR excitation in the first overtone region of NO, Sudbo and Loy were able to measure state-to-state relaxation rates [42]. In a pioneering experiment, Joswig and co-workers determined state-resolved integral cross-sections for the NO–Ar system for the first time [43, 44]. The cross sections were compared with the results of quantum mechanical scattering calculations based on the coupled state approximation. Using the potential of Nielsen *et al.*, good agreement was found for the fine-structure conserving collisions while fine structure changing collisions were noticeably underestimated. Jons *et al.* reported first state resolved differential scattering cross sections [45, 46] which were later compared with the results of a full quantum mechanical close coupling calculation by Alexander [26]. In this study, a new *ab-initio* CEPA potential energy surface was used yielding improved agreement with the experimental data. Remaining differences especially in the magnitude of the cross sections for fine-structure changing collisions motivated Alexander to determine improved *ab-initio* potential surfaces at the CCSTD(T) level of theory [31]. At this level of theory, the dispersion energy is reproduced more reliably while features of the repulsive region are affected only very little. Even with these latest improvements,

the earlier discrepancies with experimental scattering data are not completely removed. On the other hand, recent measurements of Λ doublet propensities [47] or steric asymmetries [48] are well reproduced by this new set of surfaces. Furthermore, calculated state specific rate constants for rotational energy transfer at low temperature are in excellent agreement with the recent experimental results of Smith and co-workers [28, 49]. In conclusion, we find that, although not all scattering data can be reproduced from the *ab-initio* treatment, the remaining discrepancies are most likely not related to deficiencies of the two *ab-initio* potential surfaces at the CEPA or CCSD(T) level. On the other hand, at the CCSD(T) level, we can expect more reliable results for the well region. Therefore, a true test of the quality of the surfaces will be the comparison of the bound states with corresponding experimental spectroscopic information.

In the past few years, several collision experiments for the NO+ He system have been reported. For this system, a complete set of final quantum state resolved cross sections was reported by Meyer [15]. Employing the method of counterpropagating pulsed molecular beam scattering, state-resolved differential cross sections were determined. Furthermore, the polarization dependence of the scattered intensity could be used to extract degeneracy averaged cross sections as well as the quadrupole moment of the angular momentum distributions as a simultaneous function of the final quantum state and the scattering angle. Excellent agreement with subsequent theoretical calculations by Yang and Alexander was found for the cross sections [27] and, very recently, also for the alignment data [50]. While in these experiments the λ doublets of the initial state could not be selected, using stimulated emission pumping Drabbels *et al.* were able to prepare a particular parity resolved and vibrationally excited initial state [51]. These workers reported integral state-to-state cross sections for rotational energy transfer in agreement with predictions based on the CEPA potential of Yang and Alexander [27]. Very recently an improved potential surface for the NO–He system has been calculated at the restricted coupled cluster level of theory [52]. In this study the binding energy is found to be $7\,\mathrm{cm}^{-1}$. The energies for the existing bound levels correlating with the free rotor states $j = \frac{1}{2}$ and $j = \frac{3}{2}$ were calculated as well. So far no experimental information on the NO–He complex in either its electronic ground state or its excited states has been reported.

In regards to the scattering dynamics, the systems NO + Ar and NO + He are very well characterized experimentally and theoretically in terms of potential energy surfaces and quantum scattering calculations. It is thus not surprising that the scattering of NO from Ar or He serves as an ideal test for new molecular beam scattering experiments or for the implementation of new techniques such as ion TOF analysis or ion imaging [53–55].

While numerous scattering experiments involving NO($X\,^2\Pi$) have been performed, until very recently, little information on the bound levels of the corresponding van der Waals complexes was known. Again most attention has been focused on the NO–Ar complex. The existence of the complex was first inferred from molecular beam deflection studies [56]. The first spectroscopic observation of the complex was reported by Langridge-Smith *et al.* [57]. In the laser-induced fluorescence (LIF) spectrum of an Ar molecular beam expansion containing NO, these authors found a broad feature to the blue of the band origin of the A-X transition in the monomer. This feature was attributed to transitions from the electronic ground state terminating on the repulsive wall of the excited state surface. Recently, also REMPI and LIF

spectra for the A–X transitions terminating in the bound region of the $\tilde{A}$-state have been reported by several groups for complexes with Ar [58–61], Kr [62], and Xe [62].

The first direct observation of bound rotational levels of the electronic ground state surface was accomplished by Mills *et al.* in their pioneering study using a molecular beam electric resonance spectrometer [63, 64]. The rotational structure of the observed spectrum was analysed by these authors assuming a rigid rotor Hamiltonian. This analysis provided precise structural information confirming the near T-shaped structure of the complex originally deduced from collision studies [37, 38]. Bound levels of the complex involving intermolecular vibrations have only very recently been observed in an IR-REMPI double resonance experiment [65]. The position of the observed bands and their rotational structure is extremely sensitive to different features of the potential surface. It is therefore not too surprising that these spectra reveal clearly deficiencies of the CEPA surfaces [35].

Subsequent to the study of Levy and co-workers, spectra correlating with low lying Rydberg states of NO have been observed by several groups. Among these, the different vibrational levels of the state $C\,^2\Pi$ have been the subject of most experimental studies. The first spectrum for NO($C\,^2\Pi$)–Ar was reported by Sato *et al.* applying (2 + 1) REMPI detection [66]. In later studies, Miller and Cheng extended these experiments towards higher vibrational levels of the C-state manifold and towards complexes with Ne, Kr, and Xe [67, 68]. Complex spectra correlating with the NO Rydberg states $D\,^2\Sigma$ [67, 69], $E\,^2\Sigma$ [17, 70, 71], $F\,^2\Delta$ [70], and $H\,^2\Sigma$, $H'\,^2\Pi$ [70] have been reported more recently.

Higher Rydberg states of NO have also been observed in Rg and N_2 matrices. The Rydberg transitions are blue shifted and substantially broadened in comparison with the gas phase spectra [72]. Interestingly, the matrix environment was shown to substantially influence the electronic state interactions of the NO monomer. For example, vibrational levels of the state $B\,^2\Pi$ appear unperturbed up to much larger values of v' than observed in the gas phase spectrum.

The present article is organized as follows: in section 2, we describe the experimental methods used in the REMPI and IR-REMPI double resonance spectroscopy of complexes of NO with Ar and Ne. These experiments provide detailed information on the bound levels of the electronically excited states and of the electronic ground state. The theoretical background for the analysis of these spectra is reviewed in section 3. Our goal is to provide a consistent framework for the theoretical description of the bound level structure and the intensity pattern for the different experimentally observed bands. This includes the derivation of the body-fixed representation of the quantum mechanical Hamiltonian appropriate for a van der Waals system involving an open shell diatom. The section includes also a discussion of the quantum mechanical Hamiltonian based on three angle embedding appropriate for complexes near the rigid rotor limit. Results for the states correlating with various Rydberg states of NO are summarized in section 5. Conclusions are given in section 6.

2. Experimental methods

2.1. *(2+1) REMPI spectroscopy*

Electronic spectra of small molecules such as CO, HCl and NH_3 typically lie in the vacuum ultraviolet region which is not easily accessible using commercially available laser systems. Alternatively, some of the involved excited states can be

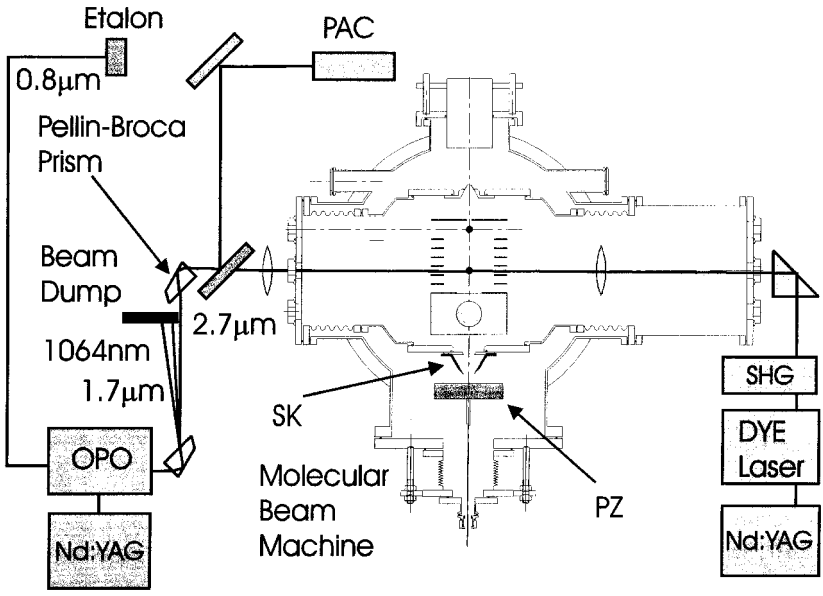

Figure 1. Set-up for the REMPI and IR-REMPI double resonance experiments. SK = skimmer, PZ = piezoelectric valve, PAC = photoacoustic cell.

accessed through non-resonant two-photon transitions. Resonances are detected through either LIF or through ionization detection in a so-called (2 + 1) REMPI process. In this process, the molecule undergoes a two-photon absorption process to a sufficiently long lived intermediate state from where it absorbs a third photon causing the ionization of the molecule. Although the effective transition probabilities are greatly reduced in comparison with allowed one-photon processes, two-photon transitions for several small molecules are strong enough to be useful for the state-specific product detection in various dynamic studies, e.g. scattering, photodissociation, predissociation and gas–surface scattering. The necessity for focusing the laser beam results in extremely small probe volumes; typically in the order of 10^{-6} cm^3. Since product densities in the experiments are in the order of 10^6–10^{10} cm^{-3} (quantum state)$^{-1}$, only the strongest two-photon transitions realizing detection efficiencies as high as 10% can be employed. This opens the interesting possibility that molecules with such a strong two-photon resonance might be used as a two-photon chromophore in a van der Waals complex. In this way, a particular van der Waals system can be studied through a scattering experiment as well as through its bound state spectroscopy. In particular, this approach opens the door to investigate the interaction of small molecules in electronically excited states. To date examples of complexes involving NO, HI [73], I_2 [74], and acetaldehyde [18] have been reported. Typically, the two-photon transition involves an excited Rydberg state that is characterized by a structure very similar to the electronic ground state.

All experiments in our laboratory are performed in a molecular beam scattering apparatus which has been described in detail previously [10, 11]. A schematic is shown in figure 1. The vacuum system consists of two differentially pumped chambers. Beam pulses of about 70 μs duration are generated in the source chamber with a home built piezoelectric molecular beam source at a repetition rate of 10 Hz. Gas mixtures of 5% NO in the appropriate rare gas and backing pressures up to 3

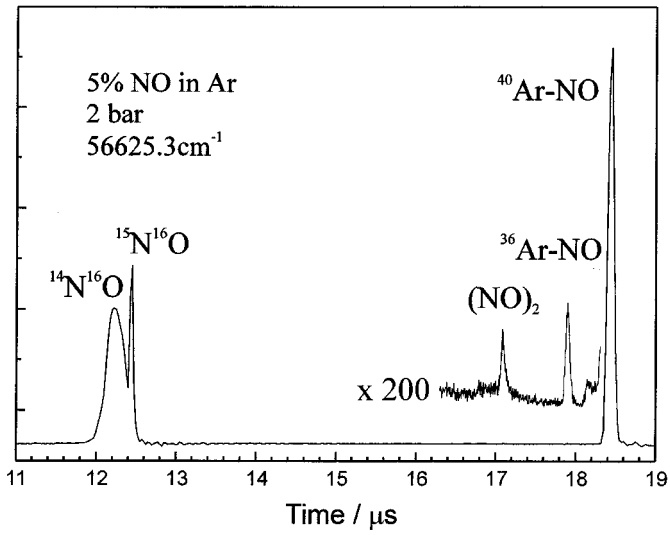

Figure 2. TOF mass spectrum taken at the indicated two-photon frequency. The inset represents a spectrum recorded with greatly increased sensitivity.

bar are used in these experiments. The gas pulses expand into vacuum from an opening with a 500 μm diameter. Typical operating pressures are 10^{-5} mbar for the source chamber and less than 10^{-6} mbar for the detection chamber. The molecular beam pulses pass through a skimmer from the source chamber into the detection chamber. The beam is intersected at right angle in the acceleration region of a TOF mass spectrometer by a focused laser beam. Complexes are excited and ionized via REMPI. The resulting ions are accelerated and mass analysed in the two-stage TOF mass spectrometer. Frequency spectra are recorded by monitoring the signal on a particular ion mass. Owing to the design of the acceleration and drift stages, the measured TOF distributions reflect directly a one-dimensional projection of the velocity distribution of the neutral particles on to the electric field direction. Since in a typical fragmentation process energy is released, a distribution of velocities results for the created fragments. Consequently, the presence of fragmentation processes is revealed as a broadening of the TOF distribution for the fragment mass. As an example, we display in figure 2 a TOF mass spectrum recorded at the indicated two-photon frequency. At this frequency, the spectrum is dominated by a sharp peak due to the normal $^{14}N^{16}O$–^{40}Ar complex. Near the TOF expected for the arrival of the NO cation, two features are observed: a sharp peak due to the isotope $^{15}N^{16}O$ and a broad distribution centred at the flight time expected for the normal NO isotope. The width of the distribution reflects the energy released as a consequence of the fragmentation process. The inset shows a mass spectrum recorded with greatly increased sensitivity. Small signals are attributed to the isotope $^{14}N^{16}O$–^{16}Ar and the NO dimer. While the dimer spectrum shows no frequency dependence, a typical C-state spectrum is measured for the NO–^{36}Ar isotope in this wavelength region. In figure 3, we compare the spectra for the complex involving the two different isotopes of Ar. Both spectra are dominated by a progression in the intermolecular stretch vibration labelled ν_s in figure 3. The small increase of the stretch frequency due to the isotope effect is clearly visible. Since the natural abundance of ^{36}Ar is only 0.36%,

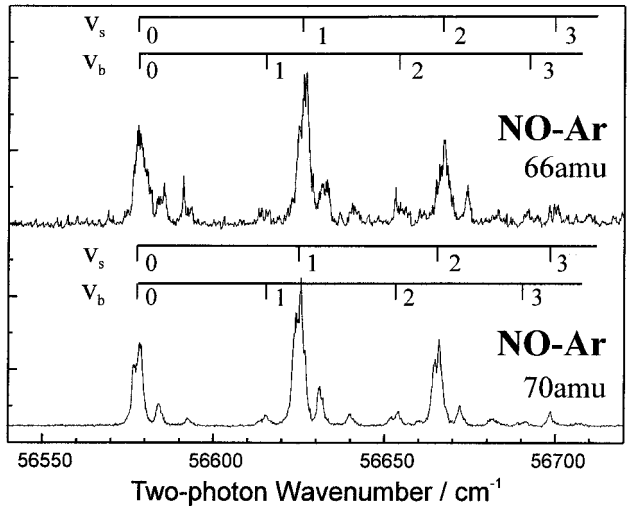

Figure 3. Comparison of spectra recorded on mass 66 and 70 amu in the wavelength region of the NO $C(v' = 2)$–$X(v'' = 0)$ transition.

the spectrum recorded for the isotope complex demonstrates the extreme sensitivity of the employed REMPI detection process.

2.2. *IR-REMPI double resonance spectroscopy*

In order to investigate the bound levels of the electronic ground state surfaces, we developed an IR-REMPI double resonance technique that uses the NO molecule in the complex both as an IR- and an ultraviolet (UV)-chromophore. In the IR excitation step, the NO molecule is excited to its first overtone level near 2.7 μm. Resonances are detected either by observing the depletion of the REMPI signal of the complex or by detecting the vibrationally excited complex. Narrow bandwidth IR radiation in this wavelength range is generated with an optical parametric oscillator (OPO) (Continuum Mirage 3000). Details of its layout and operation are described in [75, 76]. In brief, a near grazing incidence oscillator is pumped with the doubled output of an injection seeded Nd:YAG laser. Single longitudinal mode parameteric oscillation in a KTP crystal produces a first signal beam at 760 nm. The signal is amplified in a non-resonant cavity acting as a parametric amplifier. The resulting idler radiation at a wavelength of 1.7 μm acts as the signal for a final parameteric stage pumped by the delayed fundamental of the Nd:YAG laser. Typically, the output beam consists of 10–15 mJ of signal radiation and 2–5 mJ of idler radiation in the wavelength 2.1–4.0 μm.

In comparison with similar techniques based on LIF detection, the REMPI approach combined with mass spectroscopic analysis has the advantage of allowing us to discriminate against a possible strong monomer background. While the depletion scheme is applicable more generally, it often suffers from a poor signal-to-noise ratio. In contrast to double resonance schemes employing one-photon resonances [77, 78], REMPI signals involving a non-resonant two-photon absorption process exhibit considerably larger pulse-to-pulse fluctuations. Nevertheless, we have detected depletion signals larger than 10% without applying any noise reduction schemes. Our IR laser provides sufficient power to saturate vibrational overtone

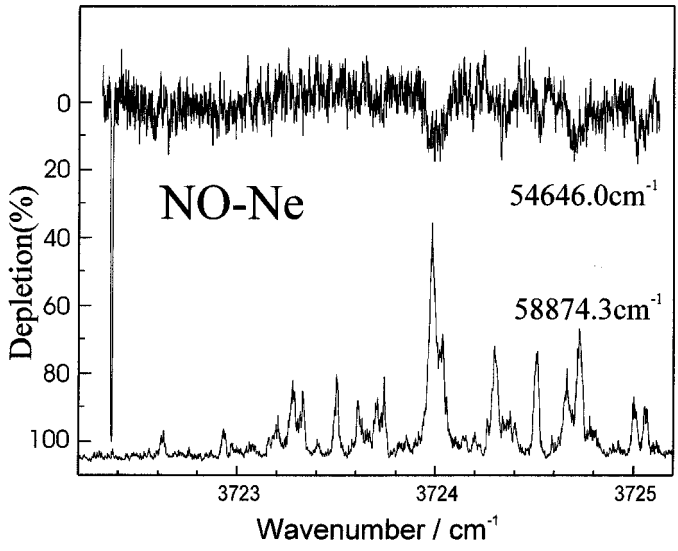

Figure 4. Spectra of band A for the NO–Ne complex taken in (top) depletion mode and (bottom) hotband mode detected at the indicated frequencies.

transitions in many molecules including NO. While this results in the expected near 50% depletion of the REMPI signal for the NO monomer, unfortunately, it does not apply to the cluster signal because of the mismatch in the linewidth of the IR laser and the employed UV laser. Since the effective resolution at the two-photon level is in the order of $0.5\,cm^{-1}$, complete rotational resolution is achieved for the NO monomer but not for the NO–X complexes. On the other hand, due to the better resolution of the IR laser, in many cases single rovibrational lines are resolved for the complex. Consequently, the UV laser probes additional states of the complex which are not depleted by the IR laser. This feature becomes an advantage if vibrationally excited complexes are detected through hotband transitions. In the particular IR-REMPI double resonance spectroscopy used in the work reviewed here, the vibrationally excited complex lives long enough to allow for the background free detection of the unfragmented complex on different electronc hotband transitions. To illustrate these two types of scan, we show in figure 4 the comparison of the depletion spectrum and the corresponding hotband spectrum of the NO–Ne complex. At this point it is important to realize that particular rotational lines of the IR spectrum can only be probed in the hotband spectrum if the UV laser is tuned to an apropriate resonance. Because of the high density of lines in many of the Rydberg state spectra (see section 5), the chance for such a coincidence is large but not certain. While most of the IR resonances are detected using a few UV resonances, the measured intensities must be considered with caution. But again, for several of the observed band systems for NO–Ar and NO–Ne, we find satisfactory agreement between calculated intensities and the intensities recorded for the hotband spectra. This fact is also confirmed in figure 4 where all strong features of the hotband spectrum correspond to a depletion of the ground state signal although characterized by a poor signal-to-noise ratio. Alternatively, we can scan both lasers simultaneously, thus ensuring that the UV laser always excites for

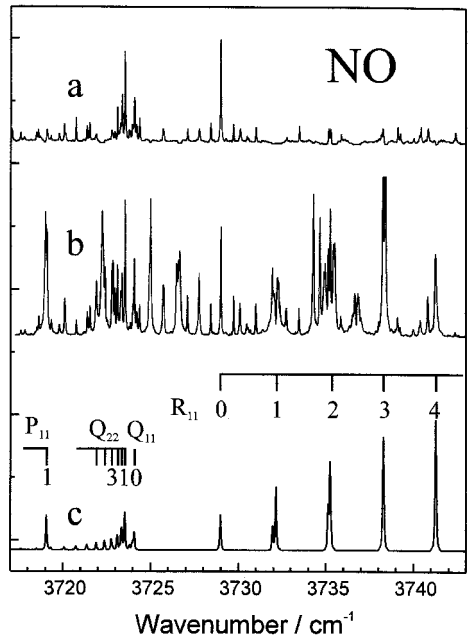

Figure 5. Room temperature photoacoustic spectra of NO (*a*) without and (*b*) with N_2-purging. (*c*) Trace calculated using the constants from [79]. Rotational lines are labelled with $j - \frac{1}{2}$.

example to a particular level of the Rydberg state. Obviously, this type of scan is very promising if the Rydberg spectrum is characterized by sharp unresolved Q-branches.

Another complication in these experiments arises from the strong water absorption in the region of the first NO overtone. Figure 5 shows room temperature photoacoustic spectra of NO recorded with and without purging of the laser beam path with N_2. The comparison with the calculated spectrum shown in the bottom part reveals that several NO lines are completely missing from the spectrum without purging due to the strong absorption in air. Intense purging with N_2 reduces the water content in the beam path sufficiently to allow the IR beam to reach the photoacoustic cell. Under these conditions, the missing NO lines are present while lines due to a small water impurity in the cell become much more prominent. In general, the photoacoustic spectrum is extremely useful in providing spectroscopic fingerprints for the identification of different features in the double resonance experiments. Furthermore, it is essential to verify the spatial alignment of the two focused laser beams under vacuum. Typically, the alignment is checked and optimized by searching for a double resonance signal for the NO monomer. Using the photoacoustic spectrum as a guide, the frequency of the IR laser is stabilized on to a particular transition of the NO overtone spectrum while the REMPI laser is tuned to a two-photon resonance of the corresponding hotband transition. The appropriate UV laser frequency is determined either from a discharge spectrum [81] or from a double resonance signal in a REMPI cell. For the cell experiment, the spatial alignment of the two laser beams is ensured by aligning both beams through a tiny aperture. Once the lasers are aligned, the UV laser is scanned through a wavelength region in which only small signals due to ground state NO are present.

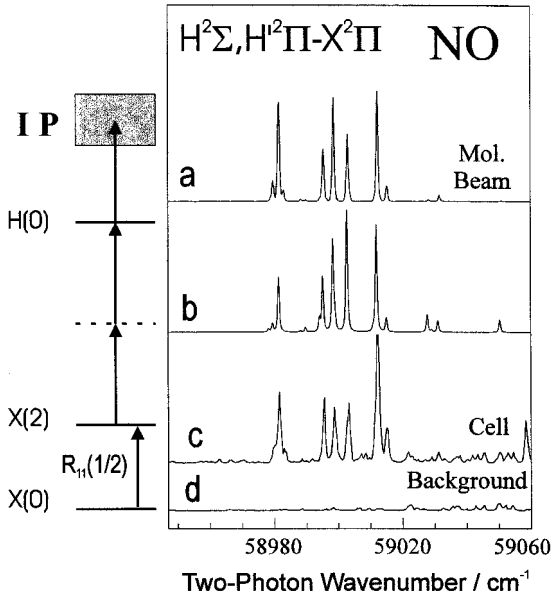

Figure 6. Double-resonance spectra of NO recorded under (*a*) molecular beam and (*c*) cell conditions. (*b*) Spectrum calculated using the procedure outlined in [80].

For our purposes, the region of the hotband transition to the Rydberg state $H\,^2\Sigma$, $H'\,^2\Pi$ is suitable since it is virtually free of transitions starting in NO ($v = 0$) even at room temperature. Trace (*c*) in figure 6 displays the REMPI spectrum recorded in the cell with the IR laser tuned to the $R_{11}(\frac{1}{2})$ line. The corresponding background spectrum, taken without the IR laser beam is shown as trace (*d*). Once the REMPI frequency for the hotband transition is determined, the spatial alignment under molecular beam conditions is verified by searching for a double resonance signal with the ion detector operating at its highest sensitivity. A small positive signal is usually detected even if the two laser beams have only minimal overlap. The double resonance spectrum recorded on the molecular beam is displayed as trace (*a*) in figure 6. Trace (*b*) represents a calculated spectrum assuming equal population for both λ-doublets of the $j = \frac{3}{2}$ level.

Another critical aspect of the present double resonance experiment is related to the possible occurrence of a strong AC-Stark shift caused by the presence of a strong non-resonant laser field. The OPO used in our experiments generates not only IR radiation around 2.7 μm, but it also generates simultaneously a much stronger output in the 1.7 μm range. When these beams are focused on to the molecular beam and when the OPO beam coincides also temporally with the UV laser beam, its resulting fields cause an AC-Stark shift of the molecular levels, i.e. the levels are shifted out of resonance with the UV laser. As can be seen in figure 7 in trace (*c*), up to 75% of the REMPI signal is lost due to the level shifts when the OPO signal beam is present. This situation is completely avoided by separating the two beams with the help of two Pellin Broca prisms. Trace (*b*) represents the depletion spectrum recorded with only the idler beam present. In this case, the maximum depletion coincides with the photoacoustic $R_{11}(\frac{1}{2})$ line. Similar effects are observed when vibrationally excited molecules are detected. The corresponding hotband spectra are displayed in figure 8.

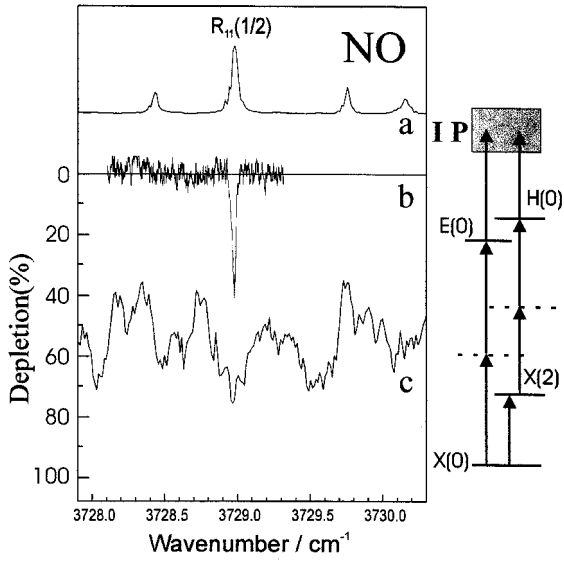

Figure 7. (*a*) Photoacoustic and (*b*) depletion spectra recorded with the UV laser fixed to the $Q_{21d}(\frac{3}{2})$ line. For trace (*b*), only the idler beam (at 2.7 μm) is present while trace (*c*) is recorded with the idler and the signal present.

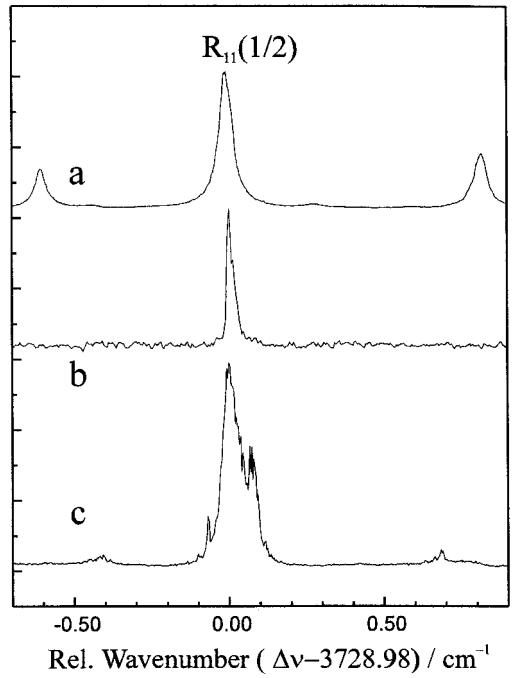

Figure 8. Double resonance spectra of NO recorded (*c*) without and (*b*) with separating the different wavelengths of the OPO output. Trace (*a*) represents the simultaneously recorded photoacoustic spectrum.

In the presence of the focused non-resonant signal field, the spectral line exhibits additional structures as well as several satellites. Unfortunately, owing to the large pulse-to-pulse fluctuations in the output of the OPO laser, these features are not well reproducible hindering a more quantitative analysis at present.

In the actual experiments, the difficulties mentioned above are avoided by (1) separating the signal from the idler beam and (2) by firing the UV laser after the IR laser. Under these circumstances, spectra are recorded with an effective resolution of about 700 MHz, mainly caused by power broadening. Examples are presented and discussed in section 4. Because the involved laser pulses have a duration of about 5 ns, their time delay must be optimized within several nanoseconds. The timing of the two lasers and the molecular beam source is controlled with two digital delay generators. In most experiments, the REMPI laser is fired about 10 ns after the IR laser. The double resonance signal decreases dramatically for delays larger than 30 ns. For these delays, vibrationally excited molecules have enough time to leave the probe volume.

3. Theoretical background

The theoretical description of van der Waals complexes involving open shell diatoms has been developed over many years by several groups [21–23, 63, 82–85]. According to Hutson, we can distinguish three limiting cases characterized by different types of interaction anisotropies [86]. For case (1), the anisotropy is so weak that the diatom is almost freely rotating within the complex. Since also the orbital angular momentum associated with the end-over-end rotation of the complex is well defined, it is convenient to use a space-fixed (sf) description. For stronger anisotropies (case (2)), the orbital angular momentum is not conserved any longer while the angular momentum of the diatom is an almost conserved quantity. In this case, it is convenient to use a body-fixed (bf) description in which the couplings due to the potential energy are minimized. On the other hand, the transformation of the kinetic energy operator to a bf frame causes additional couplings of the Coriolis type. In order to be able to use the eigenfunctions of the diatom, we use two-angle embedding for the body-fixed frame (bf(2)) which is defined with respect to a sf frame by two Euler angles α and β. The z-axis of the bf(2) frame coincides with the direction of **R** (see figure 9). The rotation of the diatom within the complex is then represented by a molecule-fixed frame (mf) whose orientation with respect to the

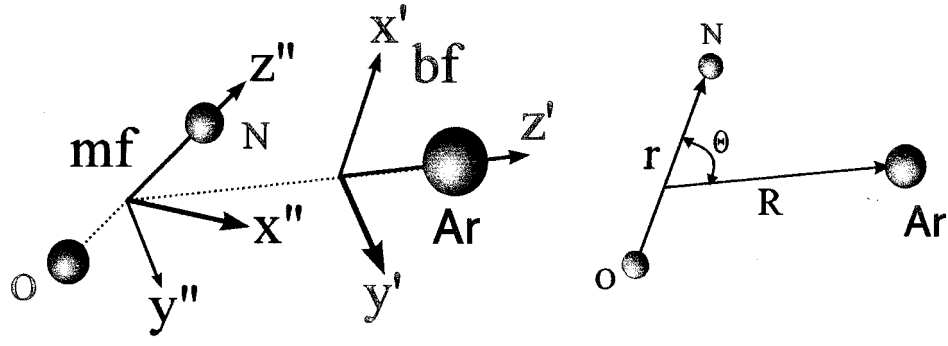

Figure 9. Definition of the coordinate frames bf(2) and (mf) and of the Jacobi coordinates used in the theoretical description of the NO–Rg complexes.

bf(2) frame is specified by the polar angles, denoted θ and ϕ, of the internuclear distance **r** in the bf(2) frame. For even larger anisotropies (case (3)) many different diatom rotor states will be coupled by the interaction potential. Obviously, systems falling in the transition region between these two cases can also be treated using the bf(2) formalism and an appropriate basis set. This treatment is used for describing the weakly bound complexes of NO–X in their electronic ground state.

The complexes become more rigid with increasing anisotropy. In this limit, the rotational structure for specific vibrational levels can be approximated by a rigid rotor Hamiltonian which is best derived using three-angle embedding. Under these circumstances the diatom will perform only small amplitude vibrations around a well defined equilibrium configuration. The bf(3) frame is defined with the vector **R** along the z axis and the (x, z) plane is chosen as the molecular plane. This approach has been successfully applied to the analysis of the rotational structure of the NO–X complexes in various strongly bound Rydberg states.

Although these limiting cases have been defined for closed shell van der Waals complexes, they can also be used to classify systems containing open shell diatoms [82, 83]. For diatoms in electronic states with $\lambda \neq 0$, the electronic degeneracy is lifted in the complex giving rise to two distinct electronic Born–Oppenheimer potential surfaces of A' and A'' symmetry. In the derivation of the appropriate quantum nechanical Hamiltonian, it is therefore necessary to include the electronic degrees of freedom for both fragments of the complex. For the description of complexes NO–Rg, we assume that the rate gas atom Rg is well described by a state $|^1S\rangle$ thus not contributing to the total angular momentum. The appropriate bf(2) Hamiltonian and relevant decoupling approximations are reviewed in the next two sections. The rigid rotor Hamiltonian suitable for open shell complexes is derived in section 3.3. By explicitly including the electronic degrees of freedom, it will be easy not only to derive but also to distinguish the different coordinate representations and basis sets.

3.1. *The body-fixed Hamiltonian: two-angle embedding*

The position of the three nuclei is described by the Jacobi coordinates r, R, θ as defined in figure 9. In the derivation of the Hamiltonian, we must distinguish three different coordinate frames: a space-fixed (sf), a body-fixed (bf) and a molecule-fixed (mf) frame. The sf frame represents an arbitrary reference frame whose origin coincides with the centre-of-mass (cm) of the nuclei. Note that, throughout the discussion, we neglect the mass polarization terms due to the difference between the location of the cm of all particles and the nuclear cm. The bf(2) frame is defined through two-angle embedding, i.e. by rotating the z axis of the sf frame through two Euler angles α and β on to the direction of **R**. The latter describes the position of the atom relative to the position of the cm of the diatom. In the bf(2) frame, the orientation of the diatom vector **r** is described by the polar angles θ and ϕ. The mf frame is defined through the rotation of the bf(2) frame through the angles θ and ϕ. The z-axes of these two frames lie along the directions of **R** and **r**, respectively. In the following, we shall assume a structureless atom. Therefore, we only need to include explicitly the N_{bc} electrons of the diatom in the total angular momentum. Their position is described with respect to frames centred at the cm of the diatom. In the sf and bf frames, they are described by vectors ξ_j and η_j.

The derivation of the Hamiltonian starts with the classical kinetic energy expressed in terms of the cm coordinates referring to the sf frames. The kinetic energy and the total angular momentum are determined as follows:

$$T = \frac{1}{2}\mu\dot{\mathbf{R}}_{\mathrm{sf}}^2 + \frac{1}{2}\mu_{\mathrm{bc}}\dot{\mathbf{r}}_{\mathrm{sf}}^2 + \frac{1}{2}\sum_{j_{\mathrm{e}}=1}^{N_{\mathrm{bc}}+N_{\mathrm{a}}} m_{\mathrm{e}}\dot{\xi}_{j_{\mathrm{e}}}^2$$

and

$$\mathbf{J}_{\mathrm{sf}} = \mu\mathbf{R}_{\mathrm{sf}} \times \dot{\mathbf{R}}_{\mathrm{sf}} + \mu_{\mathrm{bc}}\mathbf{r}_{\mathrm{sf}} \times \dot{\mathbf{r}}_{\mathrm{sf}} + m_{\mathrm{e}}\sum_{j_{\mathrm{bc}}}^{N_{\mathrm{bc}}} \xi_{j_{\mathrm{bc}}} \times \dot{\xi}_{j_{\mathrm{bc}}}. \tag{1}$$

Here μ and μ_{bc} refer to the reduced masses of the atom–diatom system and the diatom, respectively. The bf(2) representation is derived by transforming all coordinates to the bf frame as described above. If we choose as rotation angles the polar angles of $\mathbf{R}_{\mathrm{sf}}$, we find the following set of new coordinates:

$$\mathbf{R}_{\mathrm{bf}} = \tilde{\mathbf{C}}(\alpha,\beta)\mathbf{R}_{\mathrm{sf}} = \begin{pmatrix} 0 \\ 0 \\ R \end{pmatrix}, \quad \mathbf{r}_{\mathrm{bf}} = \tilde{\mathbf{C}}(\alpha,\beta)\mathbf{r}_{\mathrm{sf}}, \quad \text{and} \quad \eta_{j_{\mathrm{e}}} = \tilde{\mathbf{C}}(\alpha,\beta)\xi_{j_{\mathrm{e}}}. \tag{2}$$

The matrix $\tilde{\mathbf{C}}$ represents the product of two matrices describing the rotation through the indicated angles around the z axis and the new y axis [87]. Using the invariance of the dot product under orthogonal transformations, it is convenient to calculate velocity vectors projected on to bf(2) axes:

$$\tilde{\mathbf{C}}\dot{\mathbf{a}}_{\mathrm{sf}} = \dot{\mathbf{a}}_{\mathrm{bf}} + \tilde{\mathbf{C}}\dot{\tilde{\mathbf{C}}}^{\dagger}\dot{\mathbf{a}}_{\mathrm{bf}} = \dot{a}_{\mathrm{bf}} + \boldsymbol{\omega} \times \dot{\mathbf{a}}_{\mathrm{bf}},$$

with

$$\boldsymbol{\omega} = \begin{pmatrix} -\sin\beta\dot{\alpha} \\ \dot{\beta} \\ \cos\beta\dot{\alpha} \end{pmatrix}, \tag{3}$$

where we have introduced the familiar angular velocity vector $\boldsymbol{\omega}$ [87]. The resulting expressions for $\tilde{\mathbf{C}}\dot{\mathbf{R}}_{\mathrm{sf}}$ and $\tilde{\mathbf{C}}\dot{\mathbf{r}}_{\mathrm{sf}}$ are substituted into equation (1) yielding

$$T = \frac{\mu}{2}(\dot{R}^2 + R^2\dot{\beta}^2 + R^2\dot{\alpha}^2\sin^2\beta) + \frac{\mu_{\mathrm{bs}}}{2}(\dot{\mathbf{r}}_{\mathrm{bf}} + \boldsymbol{\omega} \times \mathbf{r}_{\mathrm{bf}})^2 + \sum_{j_{\mathrm{e}}=1}^{N_{\mathrm{bc}}+N_{\mathrm{a}}} \frac{m_{\mathrm{e}}}{2}(\dot{\boldsymbol{\eta}}_{j_{\mathrm{e}}} + \boldsymbol{\omega} \times \eta_{j_{\mathrm{e}}})^2. \tag{4}$$

The kinetic energy contribution to the classical Hamilton function is constructed by replacing in equation (4) the generalized velocities with the conjugate momenta. The latter are defined as the derivative of the kinetic energy (see equation (4)) with respect to the corresponding velocity. While the components of the momenta $\mathbf{p}_{\mathrm{r}}$ and $\mathbf{p}_{j_{\mathrm{e}}}$ are found by direct differentiation, the conjugate momenta J_α and J_β require the application of the chain rule since the components of $\boldsymbol{\omega}$ depend on the velocities $\dot{\alpha}$ and $\dot{\beta}$. In this context, it is important to realize that the total angular momentum projected on to bf axes, $\mathbf{J}^{\mathrm{bf}}$, is given by the gradient of the kinetic energy with respect to $\boldsymbol{\omega}$:

$$\nabla_{\boldsymbol{\omega}} T = \mu\mathbf{R}_{\mathrm{bf}} \times (\dot{\mathbf{R}}_{\mathrm{bf}} + \boldsymbol{\omega} \times \mathbf{R}_{\mathrm{bf}}) + (\mathbf{r}_{\mathrm{bf}} \times \mathbf{p}_r + \sum_{j_{\mathrm{e}}} \eta_{j_{\mathrm{e}}} \times \mathbf{p}_{j_{\mathrm{e}}}). \tag{5}$$

In order to show that this expression is equivalent to the total angular momentum calculated for the sf frame, but projected on to bf(2) axes, we start with equation (1) and apply the transformation to bf coordinates:

$$\mathbf{J}^{\mathrm{bf}} = \tilde{\mathbf{C}}\mathbf{J}^{\mathrm{sf}} = \mu\tilde{\mathbf{C}}\mathbf{R}_{\mathrm{sf}} \times \tilde{\mathbf{C}}\dot{\mathbf{R}}_{\mathrm{sf}} + \mu\tilde{\mathbf{C}}\mathbf{r}_{\mathrm{sf}} \times \tilde{\mathbf{C}}\dot{\mathbf{r}}_{\mathrm{sf}} + m_{\mathrm{e}} \sum_{j_{\mathrm{e}}} \tilde{\mathbf{C}}\xi_{j_{\mathrm{e}}} \times \tilde{\mathbf{C}}\dot{\xi}_{j_{\mathrm{e}}}$$

$$= \mathbf{R}_{\mathrm{bf}} \times \mathbf{P}_R + (\mathbf{r}_{\mathrm{bf}} \times \mathbf{p}_r + \sum_{j_{\mathrm{e}}} \eta_{j_{\mathrm{e}}} \times \mathbf{p}_{j_{\mathrm{e}}}) = \tilde{\mathbf{C}}\mathbf{L}^{\mathrm{sf}} + \tilde{\mathbf{C}}\mathbf{j}_{\mathrm{bc}}^{\mathrm{sf}} = \mathbf{L}^{\mathrm{bf}} + \mathbf{j}_{\mathrm{bc}}^{\mathrm{bf}}. \qquad (6)$$

Here, we have defined the sf and bf(2) representations of the components of the internal angular momentum $\mathbf{j}_{\mathrm{bc}}$ and the orbital angular momentum $\mathbf{L}$. The momenta conjugate to the generalized coordinates α and β are now calculated applying the chain rule and the definition of the internal angular momenta given in equation (6):

$$J_\alpha = \mu R^2 \sin^2\beta\dot{\alpha} - \sin\beta j_{\mathrm{bc}\,x}^{\mathrm{bf}} + \cos\beta j_{\mathrm{bc}\,z}^{\mathrm{bf}} \quad \text{and} \quad J_\beta = \mu R^2\dot{\beta} + j_{\mathrm{bc}\,y}^{\mathrm{bf}}. \qquad (7)$$

Solving these equations for the generalized velocities $\dot{\alpha}$ and $\dot{\beta}$, we find the bf(2) coordinate representation for the components of the total angular momentum vector:

$$J_x^{\mathrm{bf}} = -\operatorname{cosec}\beta J_\alpha + \cot\beta j_{\mathrm{bc}\,z}^{\mathrm{bf}}, \quad J_y^{\mathrm{bf}} = J_\beta, \quad \text{and} \quad J_z^{\mathrm{bf}} = j_{\mathrm{bc}\,z}^{\mathrm{bf}}. \qquad (8)$$

Similarly, the kinetic energy contribution to the classicial Hamilton function is found by expressing equation (4) in terms of generalized coordinates and conjugate momenta. The quantum mechanical Hamilton operator is found by applying the Podolsky formula [88, 89]. Choosing the volume element to be proportional to $R^2r^2\sin\theta\sin\beta$, only the operators involving R, r, θ, and β are non-hermitian. Effectively, when calculating products involving these operators, we must use the quantized form (e.g. $j_\theta = (\hbar/i)(\partial/\partial\theta)$) and its hermitian conjugate operator (e.g. $j_\theta^\dagger = (\hbar/i\sin\theta)(\partial/\partial\theta)\sin\theta$). In this way, the following quantum mechanical Hamiltonian is derived:

$$H = \frac{1}{2\mu R^2}\left(\left[J_x^{\mathrm{bf}} - j_{\mathrm{bc}\,x}^{\mathrm{bf}}\right]^2 + \frac{1}{\sin\beta}\left[J_y^{\mathrm{bf}} - j_{\mathrm{bc}\,y}^{\mathrm{bf}}\right]\sin\beta\left[J_y^{\mathrm{bf}} - j_{\mathrm{bc}\,y}^{\mathrm{bf}}\right]\right)$$

$$+ T_R + H_{\mathrm{BC}} + H_{\mathrm{A}} + V_{\mathrm{int}}(R, \theta, \mathbf{r}, \eta_{j_{\mathrm{bc}}}, \eta_{j_{\mathrm{a}}})$$

with

$$T_R = -\frac{\hbar^2}{2\mu R^2}\frac{\partial}{\partial R}R^2\frac{\partial}{\partial R}, \quad H_{\mathrm{BC}} = -\frac{\hbar^2}{2\mu_{\mathrm{bc}}}\nabla_{\mathbf{r}}^2 - \sum_{j_{\mathrm{bc}}}\frac{\hbar^2}{2m_{\mathrm{e}}}\nabla_{j_{\mathrm{bc}}}^2 + V_{\mathrm{BC}}(\mathbf{r}, \eta_{j_{\mathrm{bc}}}),$$

and

$$H_{\mathrm{A}} = -\sum_{j_{\mathrm{a}}}\frac{\hbar^2}{2m_{\mathrm{e}}}\nabla_{j_{\mathrm{a}}}^2 + V_{\mathrm{A}}(\eta_{j_{\mathrm{a}}}). \qquad (9)$$

In equation (9), the fragment Hamiltonians defined in terms of bf coordinates are denoted H_{BC} and $\mathrm{H_A}$. Note that we assume here a structureless atom with zero internal angular momentum, i.e. $\mathbf{j}_{\mathrm{a}} = 0$. The first term represents the energy contribution due to the end-over-end rotation of the complex while the last term represents the interaction potential which contains the various Coulomb terms due to pairs of particles from atom A and diatom BC. Since the Hamiltonian of the

diatomic fragment in equation (9) is given in terms of bf(2) coordinates, it cannot directly act in this form on the diatomic wavefunctions which are usually given in mf coordinates. Similarly, the components of the internal angular momentum occurring in the expression for the kinetic energy are given as projections on to bf axes. To ensure that the eigenfunctions of the complete Hamiltonian can be expanded in terms of the appropriate diatomic eigenfunctions, we introduce a mf frame (with origin in the cm of the diatom) through rotations by angles ϕ and θ around the bf z axis and the resulting new y axis. The polar angles ϕ and θ describe the orientation of the internuclear axis of the diatom with respect to the bf frame. Denoting the associated matrix $\tilde{\mathbf{C}}_{\mathrm{d}}(\phi,\theta)$, we define the transformation

$$\mathbf{r}_{\mathrm{mf}} = \tilde{\mathbf{C}}_{\mathrm{d}}(\phi,\theta)\mathbf{r}_{\mathrm{bf}} = \begin{pmatrix} 0 \\ 0 \\ 0 \end{pmatrix} \quad \text{and} \quad \rho_{j_{\mathrm{bc}}} = \tilde{\mathbf{C}}_{\mathrm{d}}(\phi,\theta)\eta_{j_{\mathrm{bc}}}. \tag{10}$$

While the electrostatic potential for the diatom does not change appearance when expressed in terms of these new coordinates, the interaction potential in equation (9) is defined in terms of bf coordinates which consequently must be expressed as transformed new coordinates involving the inverse transformation $\tilde{\mathbf{C}}_{\mathrm{d}}^{\dagger}(\phi,\theta)$:

$$\mathbf{r}_{\mathrm{bf}} = \tilde{\mathbf{C}}_{\mathrm{d}}^{\dagger}(\phi,\theta)\mathbf{r}_{\mathrm{mf}} \quad \text{and} \quad \eta_{j_{\mathrm{bc}}} = \tilde{\mathbf{C}}_{\mathrm{d}}^{\dagger}(\phi,\theta)\boldsymbol{\rho}_{j_{\mathrm{bc}}}. \tag{11}$$

In order to derive the modified Hamiltonian, we go back to the expression for the kinetic energy as a function of the generalized coordinates and their associated velocities. The contribution T_{BC} due to the diatomic molecule takes on the following form:

$$T_{\mathrm{BC}} = \frac{1}{2}\mu_{\mathrm{bc}}[\dot{\mathbf{r}}_{\mathrm{mf}} + (\boldsymbol{\omega}_{\mathrm{d}} + \tilde{\mathbf{C}}_{\mathrm{d}}\boldsymbol{\omega}) \times \mathbf{r}_{\mathrm{mf}}]^2 + \frac{1}{2}\sum_{j_{\mathrm{bc}}=1}^{N_{\mathrm{e}}} m_{\mathrm{e}}[\dot{\boldsymbol{\rho}}_{j_{\mathrm{bc}}} + (\boldsymbol{\omega}_{\mathrm{d}} + \tilde{\mathbf{C}}_{\mathrm{d}}\omega) \times \boldsymbol{\rho}_{j_{\mathrm{bc}}}]^2. \tag{12}$$

We see that the effect of the second transformation is to replace the original angular velocity $\boldsymbol{\omega}$ with the resultant $\boldsymbol{\omega}_r = \tilde{\mathbf{C}}_{\mathrm{d}}\boldsymbol{\omega} + \boldsymbol{\omega}_{\mathrm{d}}$. The projection of the bf diatomic angular momentum on to mf axes is given by an expression completely analogous to equations (5) and (6):

$$\mathbf{j}_{\mathrm{bc}}^{\mathrm{mf}} = \tilde{\mathbf{C}}_{\mathrm{d}}\mathbf{j}_{\mathrm{bc}}^{\mathrm{bf}} = \nabla_{\boldsymbol{\omega}_r} T_{\mathrm{BC}} = \mathbf{r}_{\mathrm{mf}} \times \mathbf{p}_r + \mathbf{l} \quad \text{with} \quad \mathbf{l} = \sum_{j_{\mathrm{bc}}} \boldsymbol{\rho}_{j_{\mathrm{bc}}} \times \mathbf{p}_{j_{\mathrm{bc}}}. \tag{13}$$

Here, $\mathbf{l}$ defines the orbital angular momentum of the electrons in terms of mf coordinates. Since only the diatomic contribution T_{BC} to the kinetic energy depends on the angular velocities $\dot{\phi}$ and $\dot{\theta}$, we find for the conjugate momenta after expressing the components of $\boldsymbol{\omega}_r$ in terms of the diatomic angular momentum:

$$j_\phi = -(j_x^{\mathrm{mf}} - l_x)\sin\theta - l_x \sin\theta + l_z \cos\theta \quad \text{and} \quad j_\theta = j_y^{\mathrm{mf}}. \tag{14}$$

Substituting these results into the expression for the kinetic energy T_{BC}, we find

$$\begin{aligned} T_{\mathrm{BC}} &= \frac{1}{2\mu_{\mathrm{bc}}}p_r^2 + \frac{1}{2\mu_{\mathrm{bc}}r^2}[(j_\theta - l_y)^2 + (\mathrm{cosec}\,\theta j_\phi + l_x - \cot\theta l_z)^2] + \frac{1}{2m_{\mathrm{e}}}\sum_{j_{\mathrm{bc}}}\mathbf{p}_{j_{\mathrm{bc}}}^2 \\ &= \frac{1}{2\mu_{\mathrm{bc}}}p_r^2 + \frac{1}{2\mu_{\mathrm{bc}}r^2}[(j_x^{\mathrm{mf}} - l_x)^2 + (j_y^{\mathrm{mf}} - l_y)^2] + \frac{1}{2m_{\mathrm{e}}}\sum_{j_{\mathrm{bc}}}\mathbf{p}_{j_{\mathrm{bc}}}^2. \end{aligned} \tag{15}$$

Since by modifying effectively the dependence of T_{BC}, and thus of T, on the angular velocity vector $\boldsymbol{\omega}$ through the introduction of the new set of generalized coordinates $\{R, \alpha, \beta, r, \phi, \theta, \boldsymbol{\rho}_{j_{bc}}, \eta_{j_a}\}$, we must replace in equations (7) and (8) the contribution of T_{BC} to the conjugate momentum J_α with the following expression:

$$J_\alpha = \cdots + \frac{\partial}{\partial \dot{\alpha}} T_{BC} = \cdots + \nabla_{\boldsymbol{\omega}_r} T_{BC} \cdot \frac{\partial}{\partial \dot{\alpha}} (\boldsymbol{\omega}_d + \tilde{\mathbf{C}}_d \boldsymbol{\omega}) = \cdots + (\tilde{\mathbf{C}}_d^\dagger \mathbf{j}_{bc}^{mf}) \cdot \frac{\partial}{\partial \dot{\alpha}} \boldsymbol{\omega}. \quad (16)$$

In the last step, we have exploited the property of the dot product with respect to the definition of the transpose real matrix $\tilde{\mathbf{C}}_d^\dagger$. Therefore, the use of mf coordinates has simply the effect of replacing in equations (7) and (8) the bf representation of the angular momentum of the diatom with its mf representation transformed to the bf frame:

$$J_\alpha = \mu R^2 \dot{\alpha} \sin^2 \beta - \sin \beta (\tilde{\mathbf{C}}_d^\dagger \mathbf{j}_{bc}^{mf})_x + \cos \beta (\tilde{\mathbf{C}}_d^\dagger \mathbf{j}_{bc}^{mf})_z, \quad J_\beta = \mu R^2 \dot{\beta} + (\tilde{\mathbf{C}}_d^\dagger \mathbf{j}_{bc}^{mf})_y$$

and

$$J_x^{bf} = -\mathrm{cosec}\, \beta J_\alpha + \cot \beta (\tilde{\mathbf{C}}_d^\dagger \mathbf{j}_{bc}^{mf})_z, \quad J_y^{bf} = K_\beta, \quad J_z^{bf} = (\tilde{\mathbf{C}}_d^\dagger \mathbf{j}_{bc}^{mf})_z. \quad (17)$$

The components of the diatomic angular momentum in the bf frame are calculated by applying the inverse transformation $\tilde{\mathbf{C}}_d^\dagger$:

$$j_{bc}^{bf} = \tilde{\mathbf{C}}_d^\dagger j_{bc}^{mf} = \begin{pmatrix} -\cot\theta\cos\phi j_\phi - \sin\phi j_\theta + \mathrm{cosec}\,\theta\cos\phi l_z \\ -\cot\theta\sin\phi j_\phi + \cos\phi j_\theta + \mathrm{cosec}\,\theta\sin\phi l_z \\ j_\phi \end{pmatrix}. \quad (18)$$

Modifying the classical Hamilton function and applying the canonical quantization rule in combination with the Podolsky formula, we derive the following representation for the quantum mechanical Hamiltonian of equation (9):

$$H = T_R + \frac{1}{2\mu R^2}\left((J_x^{bf} - j_{bc\,x}^{bf})^2 + \frac{1}{\sin\beta}(J_y^{bf} - j_{bc\,y}^{bf})\sin\beta(J_y^{bf} - j_{bc\,y}^{bf})\right) - \frac{\hbar^2}{2\mu_{bc} r^2}\frac{\partial}{\partial r} r^2 \frac{\partial}{\partial r}$$
$$+ \frac{1}{2\mu_{bc} r^2}\left((j_x^{mf} - l_x)^2 + \frac{1}{\sin\theta}(j_y^{mf} - l_y)\sin\theta(j_y^{mf} - l_y)\right) - \sum_{j_{bc}}^{N_{bc}} \frac{\hbar^2}{2m_e} \nabla_{j_{bc}}^2$$
$$+ V_{BC}(\mathbf{r}, \boldsymbol{\rho}_{j_{bc}}) + H_A + V_{int}(R, r, \theta, (\phi), \eta_{j_{bc}}, \eta_{j_a}) \quad \text{with} \quad \mathbf{j}_{bc}^{bf} = \tilde{\mathbf{C}}_d^\dagger \mathbf{j}_{bc}^{mf}. \quad (19)$$

In this form, we recognize again the fragment Hamiltonians H_A and H_{BC}. In contrast to equation (9), all diatomic coordinates are referred to the mf frame. Note also that the second term involves the transformed mf diatomic angular momentum with the components given in equation (18) while the diatom Hamiltonian H_{BC} involves directly the mf components. The quantum mechanical operators associated with the different angular momentum components are found again by applying the canonical quantization rule. It is important to realize that the components of $\mathbf{j}_{bc}^{bf}$ obey normal commutation rules while the components of $\mathbf{J}^{bf}$ and $\mathbf{j}_{bc}^{mf}$ do not follow either normal or anomalous commutation rules. This unsatisfactory situation is remedied by introducing an isomorphic Hamiltonian [90–92] which is derived from the original Hamiltonian by applying two unitary transformations

$$U = \exp\left[\frac{i}{\hbar} j^{\mathrm{bf}}_{\mathrm{bc}\,z}\chi\right] \quad \text{and} \quad U_{\mathrm{d}} = \exp\left[\frac{i}{\hbar} l_z \chi_{\mathrm{d}}\right]. \tag{20}$$

These transformations introduce additional angles χ and χ_{d} causing the isomorphic Hamiltonian to have a larger number of eigenfunctions than the original. For example, among the possible eigenfunctions $\tilde{\psi}$ of the isomorphic Hamiltonian $\tilde{H}$, only those represent transformed eigenfunctions of the true Hamiltonian for which the actions of the operators $j^{\mathrm{bf}}_{\mathrm{bc}\,z}$ and j_χ are identical. This condition implies that the projection P of the total angular momentum $\mathbf{J}^{\mathrm{bf}}$ on to the bf z axis is identical to the projection of $\mathbf{j}^{\mathrm{bf}}_{\mathrm{bc}}$ on to the same axis. The isomorphic Hamiltonian $\tilde{H}$ can be cast into a form which involves a total angular momentum vector $\mathbf{J}'^{\mathrm{bf}}$ whose components obey the usual anomalous commutation rules:

$$\tilde{H} = T_R + \frac{(J'^{\mathrm{bf}}_x - j^{\mathrm{bf}}_{\mathrm{bc}\,x})^2 + (J'^{\mathrm{bf}}_y - j^{\mathrm{bf}}_{\mathrm{bc}\,y})^2}{2\mu R^2} + V_{\mathrm{int}}(R, r, \theta, \eta_{j_{\mathrm{bc}}}, \eta_{j_{\mathrm{a}}}) + H_{\mathrm{A}} + \tilde{H}_{\mathrm{BC}}. \tag{21}$$

The isomorphic Hamiltonian $\tilde{H}_{\mathrm{BC}}$ of the diatom is generated in a completely analogous manner by applying the unitary transformation U_{d} which involves the z-component of the electronic orbital angular momentum and an angle χ_{d}. In the case of an open shell diatom, the resultant electron spin is taken into account by replacing the components of $\mathbf{l}$ with $\mathbf{l}+\mathbf{s}$. Depending on the type of diatom, additional terms describing spin–orbit and spin–rotation interaction might have to be added to the Hamiltonian. Only those eigenfunctions of $\tilde{H}_{\mathrm{BC}}$ are used for which the projection ω of the diatom's total angular momentum on to the z axis of the mf frame is identical to the sum of the projections λ of the orbital angular momentum and σ of the spin on to the same axis, i.e. $\omega = \lambda + \sigma$. Therefore, we can expand the eigenfunctions for the original Hamiltonian (see equation (19)) in terms of products of diatom states and eigenfunctions of the total angular momentum:

$$\Psi^{JM}_{Pj\omega}(\alpha, \beta, \phi, \theta, r, \boldsymbol{\rho}_{j_{\mathrm{e}}}) = \sqrt{\frac{2J+1}{4\pi}} D^{(J)*}_{MP}(\alpha, \beta, 0) \sqrt{\frac{2j+1}{4\pi}} D^{(j)*}_{P\omega}(\phi, \theta, o) \psi^{\mathrm{el}}_{n\lambda}(r, \boldsymbol{\rho}_{j_{\mathrm{bc}}}) \chi_{s\sigma}$$

or in short form

$$|JMPj\omega\rangle = |JMP\rangle |jP\omega\rangle |n\lambda\rangle |s\sigma\rangle \quad \text{with} \quad \omega = \lambda + \sigma. \tag{22}$$

Note that we use here signed values for the various projection quantum numbers and that we did not include explicitly the eigenfunction of the atom which is assumed to be in a $|^1S\rangle$-state.

In an electronic structure calculation, eigenfunctions to the electronic Hamiltonian H_{el} of the complex are determined. This implies the partitioning of the Hamiltonian in the form

$$H = \frac{1}{2\mu R^2}\left(\left[J^{\mathrm{bf}}_x - j^{\mathrm{bf}}_{\mathrm{bc}\,x}\right]^2 + \frac{1}{\sin\beta}[J^{\mathrm{bf}}_y - j^{\mathrm{bf}}_{\mathrm{bc}\,y}] \sin\beta [J^{\mathrm{bf}}_y - j^{\mathrm{bf}}_{\mathrm{bc}\,y}] \right)$$

$$+ T_R - \frac{\hbar^2}{2\mu_{\mathrm{bc}}} \nabla^2_{\mathbf{r}} + H_{\mathrm{el}}$$

with

$$H_{\mathrm{el}} = -\frac{\hbar}{2m_{\mathrm{e}}}\left(\sum_{j_{\mathrm{bc}}}\nabla^2_{j_{\mathrm{bc}}} + \sum_{j_{\mathrm{a}}}\nabla^2_{j_{\mathrm{a}}}\right) + V_{\mathrm{A}}(\eta_{j_{\mathrm{a}}}) + V_{\mathrm{BC}}(r, \rho_{j_{\mathrm{bc}}}) + V_{\mathrm{int}}(R, \theta, r, \eta_{j_{\mathrm{bc}}}, \eta_{j_{\mathrm{a}}}). \tag{23}$$

The eigenvalues of the electronic Hamiltonian H_{el} define two potential surfaces of A′ and A″ reflection symmetry which are related to the matrix elements of the electrostatic potential in equation (19) involving the electronic wavefunctions $|n\lambda'\rangle$ and $|n\lambda\rangle$ (e.g. $\lambda = \pm 1$ for a diatom in a Π-state) [23]:

$$\langle n+1|V_{\mathrm{int}}|n+1\rangle = \langle n-1|V_{\mathrm{int}}|n-1\rangle = \tfrac{1}{2}(V^{\mathrm{int}}_{\Pi}(\mathrm{A}'; R, r, \theta) + V^{\mathrm{int}}_{\Pi}(\mathrm{A}''; R, r, \theta))$$

$$\langle n+1|V_{\mathrm{int}}|n-1\rangle = \langle n-1|V_{\mathrm{int}}|n+1\rangle = \tfrac{1}{2}(V^{\mathrm{int}}_{\Pi}(\mathrm{A}'; R, r, \theta) - V^{\mathrm{int}}_{\Pi}(\mathrm{A}''; R, r, \theta)). \tag{24}$$

As shown by Alexander, these matrix elements can be expanded in terms of rotation matrix elements [23]. The diagonal elements ($\lambda = \lambda'$) represent the average of the two adiabatic potentials of A′ and A″ reflection symmetry. They are given as an expansion in terms of Legendre polynomials. On the other hand, the off-diagonal elements are related to the difference of the adiabatic potentials involving an expansion in terms of associated Legendre polynomials:

$$\langle n\lambda|V_{\mathrm{int}}|n\lambda'\rangle = \sum_{\tilde{l}} D^{(\tilde{l})*}_{0\lambda-\lambda'}(0, \theta, 0)\, V_{\tilde{l}\lambda-\lambda'}(R, r). \tag{25}$$

3.2. *Energy level pattern and decoupling approximations*

The energy level pattern as well as various decoupling approximations are best discussed defining a bender Hamiltonian by retaining only those terms of the original Hamiltonian (see equation (21)) which are diagonal in the projection P of the total angular momentum on to the z axis of the bf(2) system [86, 93, 94]

$$H_{\mathrm{bend}} = B(R)(\mathbf{J}^{\mathrm{bf2}} - J^{\mathrm{bf2}}_z + \mathbf{j}^{\mathrm{bf2}} - j^{\mathrm{bf2}}_z) + H^{(0)}_{\mathrm{BC}} + V_{\mathrm{int}}$$

with

$$H^{(0)}_{\mathrm{BC}} = -b(r)\left\{\frac{1}{\sin\theta}\frac{\partial}{\partial\theta}\sin\theta\frac{\partial}{\partial\theta} + \frac{1}{\sin^2\theta}\frac{\partial^2}{\partial\phi^2}\right\} - \sum_{j_{\mathrm{bc}}}^{N_{\mathrm{bc}}}\frac{\hbar^2}{2m_{\mathrm{e}}}\nabla^2_{j_{\mathrm{bc}}} + V_{\mathrm{BC}}(\mathbf{r}, \rho_{j_{\mathrm{bc}}}). \tag{26}$$

Note that we still retain the dependence on the electronic coordinates. Potential terms depending on the internuclear coordinates are recovered forming matrix elements according to equation (25). Since the different couplings do not involve the stretch coordinates r and R, we might consider the zeroth order bender Hamiltonian as vibrationally averaged over these degrees of freedom. The energy associated with the bending and rotational degrees of freedom can be estimated from the diagonal matrix elements of the bender Hamiltonian. Using the basis set of equation (22), the energy including the correction due to the electrostatic potential of equation (24) plus the energy due to the stretch vibration is determined in first order:

$$E^{JPv_{\mathrm{s}}}_{\mathrm{tot}\,j\omega} = E^{(0)}_{\mathrm{vib}\,v_{\mathrm{s}}} + E^{(\mathrm{BC})}_{j\omega} + B(J(J+1) + j(j+1) - 2P^2)$$
$$+ (2j+1)\sum_{\tilde{l}\neq 0}(-)^{P-\omega}\begin{pmatrix} j & \tilde{l} & j \\ -P & 0 & P\end{pmatrix}\begin{pmatrix} j & \tilde{l} & j \\ -\omega & 0 & \omega\end{pmatrix}\langle v_{\mathrm{s}}|V_{\tilde{l}0}(R)|v_{\mathrm{s}}\rangle. \tag{27}$$

For a weakly anisotropic system, the last term makes only a small contribution and j, ω, and P are approximately good quantum numbers. This situation corresponds to case (2) defined by Hutson [86]. For stronger anisotropies, case (3) in the notation of Hutson, free rotor states with different j are strongly mixed by the different expansion terms of the interaction potential leaving only P and ω as useful quantum numbers. Furthermore, the energy levels which are degenerate in the free rotor limit are split into sublevels corresponding to different combinations of P and ω. While the lowest expansion terms of even and odd order determine the magnitude of the splittings, they also must reflect directly the equlilibrium structure of the complex. A linear structure requires the term V_{20} to be negative resulting in a potential surface with possible minima at $\theta = 0^\circ$ and $\theta = 180^\circ$. The minima will be identical only for a homonuclear diatom. As a result, the simultaneous presence of a negative V_{20} term and a V_{10} term in a linear complex removes the degeneracies in P and ω. For small values of θ, we can approximate the bender Hamiltonian with the Hamiltonian of a two-dimensional harmonic oscillator [86]:

$$H_{\mathrm{BC}}^{(0)}(\mathrm{lin}) = -b(r)\left\{\frac{\partial^2}{\partial\theta^2} + \frac{1}{\theta}\frac{\partial}{\partial\theta} + \frac{1}{\theta^2}\frac{\partial^2}{\partial\phi^2}\right\} - \sum_{j_{\mathrm{bc}}}^{N_{\mathrm{bc}}} \frac{\hbar^2}{2m_{\mathrm{e}}}\nabla_{j_{\mathrm{bc}}}^2 + V_{\mathrm{BC}}(\mathbf{r}, \boldsymbol{\rho}_{j_{\mathrm{bc}}}). \tag{28}$$

The bending motion and the ϕ-rotation are coupled through the kinetic energy operator. In the limit of small angles θ, this operator can be identified with the Laplacian in two dimensions. After forming the appropriate matrix elements, for example using the basis set defined in equation (22), the resulting potential terms will depend only on the bending angle θ and not on ϕ. For small amplitudes, this term can be approximated by a term quadratic in θ providing us with a Hamiltonian for a two-dimensional harmonic oscillator. For a T-shaped configuration, a positive V_{20} term must dominate over the odd expansion terms resulting in a weak electrostatic splitting of the ω levels. The bending Hamiltonian for $\theta = 90^\circ$ decouples into a purely vibrational and a purely rotational term

$$H_{\mathrm{BC}}^{(0)}(\mathrm{perp}) = -b(r)\left\{\frac{\partial^2}{\partial\theta^2} + \frac{\partial^2}{\partial\phi^2}\right\} - \sum_{j_{\mathrm{bc}}}^{N_{\mathrm{bc}}} \frac{\hbar^2}{2m_{\mathrm{e}}}\nabla_{j_{\mathrm{bc}}}^2 + V_{\mathrm{BC}}(\mathbf{r}, \boldsymbol{\rho}_{j_{\mathrm{bc}}}). \tag{29}$$

Since the resulting potential matrix elements do not depend on ϕ, we find that the contribution to the rotational energy is approximately given by bP^2. In terms of a rigid rotor, this term represents the energy associated with the a-axis rotation.

Examples for open shell complexes with linear and T-shaped geometry are the rare gas complexes of OH and NO, respectively. In the case of a closed shell complex, i.e. a complex with a diatom in a $^1\Sigma$-state, j is integer, and ω vanishes. Therefore, only even terms in the potential expansion contribute to the energy in first order. Similarly, the odd expansion terms are absent for a homonuclear diatom since $\tilde{l}$ is restricted to even values.

For an almost freely rotating diatom, the first three terms in equation (27) are nearly degenerate in P and ω. The splitting of these degenerate levels due to the electrostatic potential is not necessarily complete for all combinations of P and ω. For example, if we consider the leading term of the potential anisotropy ($\tilde{l} = 1$), we find that the correction does only depend on the sign of the product ($P\omega$). If we replace in equation (27) P and ω with their respective negative values, we find that the product of the two 3j-symbols is invariant, i.e.

$$(-)^{-P+\omega}\begin{pmatrix} j & 1 & j \\ P & 0 & -P \end{pmatrix}\begin{pmatrix} j & 1 & j \\ \omega & 0 & -\omega \end{pmatrix} = (-)^{P-\omega+2\omega-2P+4j+2}\begin{pmatrix} j & 1 & j \\ -P & 0 & P \end{pmatrix}\begin{pmatrix} j & 1 & j \\ -\omega & 0 & \omega \end{pmatrix}. \tag{30}$$

Since, within this first-order perturbation scheme, levels corresponding to (P,ω) and $(-P,-\omega)$ are degenerate, it is advantageous to combine these states into two new basis states with well defined parity. The signed $(P\omega)$ basis set is defined as

$$\begin{aligned}\Psi^{JM}_{P\zeta j\omega}(\alpha,\beta,\phi,\theta,r,\boldsymbol{\rho}_{j_{bc}}) &= |JMP\zeta j\omega\rangle \\ &= \frac{1}{\sqrt{2}}\{|JMP\rangle|jP\omega\rangle|n\lambda\rangle|s\sigma\rangle \\ &\quad + \zeta|JM-P\rangle|j-P-\omega\rangle|n-\lambda\rangle|s-\sigma\rangle\}\end{aligned} \tag{31}$$

where the symmetry quantum number ζ takes on the values ±1. It is related to the overall parity η of the basis state: $\eta=\zeta(-)^{J-s}$. Ultimately, the degeneracy in ζ is removed by Coriolis interaction involving states with $P=\frac{1}{2}$. This phenomenon is referred to as P-type doubling in analogy to the λ-doubling in diatomic molecules [95].

For linear complexes near the free rotor limit, a convenient choice for the $(P\omega)$ basis set uses positive values for ω and signed ones for P [84]. For this configuration, ω is a nearly good quantum number while the energy levels can be regarded as split into different P-components. For a T-shaped complex, the main contribution of the rotational energy is determined by the term quadratic in P while the splitting of the different $(P\omega)$-states is expected to be small [82]. Therefore, it is advantageous to restrict P to positive values while ω is treated as a signed quantum number.

Neglecting the dependence on the intramolecular distance r, the complete wavefunction is expanded in terms of the signed $(P\omega)$ basis set:

$$\Psi^{JMv\zeta}_{\text{tot}} = \sum_{P'j'\omega'}\frac{1}{R}X^{Jv\zeta}_{P'j'\omega'}(R)|JMP'\zeta j'\omega'\rangle. \tag{32}$$

The radial coefficients $X^{Jv\zeta}_{P'j'\omega'}(R)$ satisfy the set of close coupled equations:

$$\begin{aligned}&\left\{-\frac{\hbar^2}{2\mu}\frac{\mathrm{d}^2}{\mathrm{d}R^2}+B(J(J+1)+j(j+1)-2P^2)-[E^{Jv\zeta}_{\text{tot}}-E^{(\text{BC})}_{j\omega}]\right\}X^{Jv\zeta}_{Pj\omega}(R) \\ &\quad = -\sum_{P'j'\omega'}X^{Jv\zeta}_{P'j'\omega'}(R)\langle JMP\zeta j\omega|H^{(1)}_{\text{rot}}+H^{(1)}_{\text{BC}}+V_{\text{int}}|JMP'\zeta'j'\omega'\rangle.\end{aligned} \tag{33}$$

On the right-hand side, we have collected the off-diagonal terms due to the Coriolis and spin-uncoupling operators and due to the interaction potential. Other perturbations, not explicitly included in the Hamiltonian of equation (21), are various spin interactions and centrifugal distortion effects. The operators, $H^{(1)}_{\text{rot}}$ and $H^{(1)}_{\text{BC}}$, are defined in terms of standard shift operators:

$$H^{(1)}_{\text{rot}} = -\frac{B}{\hbar^2}(j^{\text{bf}}_{+}J^{\text{bf}}_{-}+j^{\text{bf}}_{-}J^{\text{bf}}_{+}) \quad \text{and} \quad H^{(1)}_{\text{BC}} = -\frac{b}{\hbar^2}(j^{\text{mf}}_{+}s_{-}+j^{\text{mf}}_{-}s_{+}). \tag{34}$$

Because $\mathbf{j}^{\text{bf}}$ represents the transformed mf operator (see equation (18)), it obeys normal commutation rules. This implies that the associated ladder operators act on the angle associated with the first magnetic quantum number in $|jP\omega\rangle$, i.e. the

projection P on to the bf(2) z axis. On the other hand, the bf operator $\mathbf{J}^{\mathrm{bf}}$ follows anomalous commutation rules which imply that J_{+}^{bf} is actually a lowering operator while J_{-}^{bf} acts like a raising operator. Both operators act on the second magnetic quantum number in $|JMP\rangle$. Evaluating the matrix elements for the Coriolis coupling we find three contributions depending on the values of P and P':

$$\langle JMP\zeta j\omega|H_{\mathrm{rot}}^{(1)}|JMP'\zeta' j'\omega'\rangle = -\delta_{jj'}\delta_{\zeta\zeta'}B\{F(P')\delta_{PP'+1}\delta_{\omega\omega'} + F(P'-1)\delta_{PP'-1}\delta_{\omega\omega'} + \zeta F(P'-1)\delta_{P1-P'}\delta_{\omega-\omega'}\}$$
$$\text{with } F(P) = \{[J(J+1) - P(P+1)][j(j+1) - P(P+1)]\}^{1/2}. \quad (35)$$

The matrix representation of $H_{\mathrm{rot}}^{(1)}$ is diagonal in j. On the other hand, it is responsible for the coupling of states with $\Delta P = \pm 1$. Special care must be applied for the situation of $P = P' = \frac{1}{2}$. In this case, the selection rule $\omega' = \omega$ applies, i.e. $\Delta\omega \neq 0$ and $\Delta P = 0$. This last term is the only perturbation which depends on the quantum number ζ. Ultimately, it is this term which causes P-type doubling.

Because the spin coupling operator $H_{\mathrm{BC}}^{(1)}$ only acts on the diatom part of the wavefunction, its matrix representation is diagonal in P and ζ. Off-diagonal elements exist only for states which differ in the quantum numbers ω and σ by one unit:

$$\langle JMP\zeta j\omega|H_{\mathrm{BC}}^{(1)}|JMP'\zeta' j'\omega'\rangle = -\delta_{jj'}\delta_{PP'}\delta_{\zeta\zeta'}\delta_{\lambda\lambda'}b\{f(\omega'-1)\delta_{\omega\omega'-1}\delta_{\sigma\sigma'-1} + f(\omega')\delta_{\omega\omega'+1}\delta_{\sigma\sigma'+1}\}$$
$$\text{with} \quad f(\omega) = \{j(j+1) - \omega(\omega+1)\}^{1/2}. \quad (36)$$

For the ground states of the radicals NO and OH, we have $\omega = \pm\frac{1}{2}$ and $\pm\frac{3}{2}$, respectively. Of the possible basis states, the first term in equation (36) couples, for example, states with $(\omega, \lambda, \sigma) = (\frac{1}{2}, +1, -\frac{1}{2})$ and $(\omega', \lambda', \sigma') = (\frac{3}{2}, +1, +\frac{1}{2})$.

A third source for the coupling of different basis states is the electrostatic potential. Its matrix representation has off-diagonal elements involving the average potential ($\Delta j \neq 0$ and $\Delta\omega = 0$) or the difference potential ($\Delta j \neq 0$ and $\Delta\omega = \pm 2$)

$$\langle JMP\zeta j\omega|V_{\mathrm{int}}|JMP'\zeta' h'\omega'\rangle = \delta_{PP'}\delta_{\zeta\zeta'}[j][j']\sum_{\tilde{l}}(-)^{P-\omega}\begin{pmatrix} j & \tilde{l} & j' \\ -P & 0 & P \end{pmatrix}\begin{pmatrix} j & \tilde{l} & j' \\ -\omega & \lambda-\lambda' & \omega' \end{pmatrix}V_{\tilde{l}\lambda-\lambda'}(R). \quad (37)$$

For simplicity, we use the abbreviation $[j] = (2j+1)^{1/2}$. The potential matrix is diagonal in J, M, P, ζ and its elements do not even depend on J, M, and ζ. The average potential mixes different free rotor states with the same projection ω while the difference potential mixes states with $\Delta\omega = \pm 2$. The latter contributes to the parity splitting or P-type doubling.

3.2.1. *Centrifugal decoupling and adiabatic bender approximation*

Instead of working with the set of close coupled equations given in equation (33), the stretch motion is most efficiently decoupled from the rotation–bending motion in the so-called adiabatic bender approximation [93, 94]. In this approach, the complete wavefunction is expanded in terms of bender eigenfunctions which diagonalize the bender Hamiltonian defined in equation (26). While the matrix representation of H_{bend} is diagonal in P and independent of ζ, it depends parametrically on the stretch

coordinate R. Thus, when we expand its eigenfunctions in terms of the $(P\omega)$ basis set, the coefficients $W^{JPn}_{j'\omega'}(R)$ will be R-dependent:

$$\Psi^{JMP\zeta n}_{\text{bend}} = \sum_{j'\omega'} W^{JPn}_{j'\omega'}(R)|JMP\zeta j'\omega'\rangle. \tag{38}$$

The coefficients $W^{JPn}_{j'\omega'}(R)$ are determined by diagonalizing the R-dependent matrix associated with the following eigenvalue problem:

$$\sum_{j'\omega'}\{[B(R)(J(J+1)+j(j+1)-2P^2)+E^{(\text{BC})}_{j\omega}]\delta_{jj'}\delta_{\omega\omega'} + \langle JMP\zeta j\omega|V^{\text{e.s.}}_{\text{int}}|JMP\zeta j'\omega'\rangle\}W^{JPn}_{j'\omega'}(R) = E^{JPn}_{\text{bend}}(R)W^{JPn}_{j\omega}(R). \tag{39}$$

The potential matrix is diagonal in P and independent of J and ζ. In principle, the contribution due to the end-over-end rotation of the complex still depends on the total angular momentum quantum number J. On the other hand, the rotational energy is much smaller than the energy associated with the intermolecular vibrations of the fragments. Therefore, we neglect in a first approximation this dependence by replacing the true centrifugal barrier with an effective value independent of J:

$$B(R)J(J+1) = B(R)\bar{l}(\bar{l}+1). \tag{40}$$

The R-dependent eigenvalues $E^{Pn}_{\text{bend}}(R)$ represent the total energy of the system except for the energy associated with the stretch vibration and the end-over-end rotation. For large separations, $R \to \infty$, contributions due to the bending vibrations must vanish and the eigenvalue represents the energy associated with a free rotor state of the diatom: $E^{(\text{BC})}_{j\omega}$. For example, the level $j = \frac{1}{2}, |\omega| = \frac{1}{2}$, will split into two levels with $P\omega = \frac{1}{4}$ and $P\omega = -\frac{1}{4}$ owing to the influence of the approaching atom. Each level is still degenerate in the symmetry quantum number $\zeta = \pm 1$. Taking advantage of this correlation, we define adiabatic bender potentials $V^{Pn}_{\text{bend}}(R)$ which provide the potential energy for the intermolecular stretch vibration:

$$V^{Pn}_{\text{bend}}(R) = E^{Pn}_{\text{bend}}(R) - E^{(\text{BC})}_{j\omega} - B(R)\bar{l}(\bar{l}+1). \tag{41}$$

Expanding the complete eigenfunction in terms of bender functions

$$\Psi^{JM\nu\zeta}_{\text{tot}} = \sum_{Pn}\frac{1}{R}U^{J\nu\zeta}_{Pn}(R)\Psi^{JMP\zeta n}_{\text{bend}} = \sum_{Pn}\sum_{j'\omega'}\frac{1}{R}U^{J\nu\zeta}_{Pn}(R)W^{Pn}_{j'\omega'}(R)|JMP\zeta j'\omega'\rangle \tag{42}$$

and substituting it into the complete Schrödinger equation, we recover a set of close coupled equations:

$$\begin{aligned}\{T_R + H_{\text{bend}} + B(R)(J^{\text{bf}^2} - \bar{l}(\bar{l}+1)) - E^{J\bar{\nu}}_{\text{tot}}\}\Psi^{JM\nu\zeta}_{\text{tot}} &= -H^{(1)}_{\text{rot}}\Psi^{JM\nu\zeta}_{\text{tot}} \Leftrightarrow \sum_{Pn}\left\{T_R\frac{1}{R}U^{J\nu\zeta}_{Pn}(R)\Psi^{JMPn}_{\text{bend}} + \frac{1}{R}U^{J\nu\zeta}_{Pn}(R)\Psi^{JMPn}_{\text{bend}}\right. \\ &\quad \left.\times[E^{Pn}_{\text{bend}}(R) - B(R)\bar{l}(\bar{l}+1) + B(R)J(J+1) - E^{J\nu\zeta}_{\text{tot}}]\right\} \\ &= -\sum_{Pn}H^{(1)}_{\text{rot}}\frac{1}{R}U^{J\nu\zeta}_{Pn}(R)\Psi^{JMPn}_{\text{bend}}.\end{aligned} \tag{43}$$

Note that we have neglected here the spin-uncoupling operator for the diatomic molecule. Its effect is easily taken into account by representing the diatomic part of

the basis states as a linear combination of states with different absolute values of ω. Expressing the total energy as a sum of fragment energy $E_{j\omega}^{(\mathrm{BC})}$ and the rovibrational energy $E_{Jv\zeta}^{vr}$ associated with the intermolecular vibrational modes, $E_{\mathrm{tot}}^{Jv\zeta} = E_{Jv\zeta}^{vr} + E_{j\omega}^{(\mathrm{BC})}$, we can introduce the adiabatic potential into equation (43):

$$\sum_{Pn}\left\{T_R\frac{1}{R}U_{Pn}^{Jv\zeta}(R)\Psi_{\mathrm{bend}}^{JMPn}+\frac{1}{R}U_{Pn}^{Jv\zeta}(R)\Psi_{\mathrm{bend}}^{JMPn}\left[V_{\mathrm{bend}}^{Pn}(R)+B(R)J(J+1)-E_{Jv\zeta}^{vr}\right]\right\}$$
$$=-\sum_{Pn}H_{\mathrm{rot}}^{(1)}\frac{1}{R}U_{Pn}^{Jv\zeta}(R)\Psi_{\mathrm{bend}}^{JMPn}. \tag{44}$$

Obviously, the Coriolis coupling term on the right-hand side is responsible for mixing states that differ in P. This coupling term is neglected in the 'centrifugal decoupling (CD) approximation'. At this level of approximation, P becomes a good quantum number. Because the P-type doubling results from the Coriolis coupling term, energy levels at the CD level must be degenerate in the symmetry quantum number ζ. The complete CD wavefunction is given in the form

$$\Psi_{\mathrm{tot}}^{JMPv\zeta}=\sum_{n}\frac{1}{R}U_{Pn}^{Jv}(R)\Psi_{\mathrm{bend}}^{JMP\zeta n}=\sum_{nj'\omega'}\frac{1}{R}U_{Pn}^{Jv}(R)W_{j'\omega'}^{Pn}(R)|JMP\zeta j'\omega'\rangle. \tag{45}$$

In addition to Coriolis coupling, we find in equation (44) non-adiabatic couplings between different bender states due to the operator T_R:

$$\frac{1}{R}U_{P\eta}^{Jv}(R)\langle\Psi_{\mathrm{bend}}^{JMPn}|T_R|\Psi_{\mathrm{bend}}^{JMPn'}\rangle_{\theta,\eta}. \tag{46}$$

The matrix element represents integration over all coordinates except the stretch coordinate. Within the 'adiabatic bender approximation', these non-adiabatic couplings as well as the Coriolis terms are neglected. Therefore, the complete wavefunction is approximated as a product of a bender and a stretch wavefunction

$$\Psi_{\mathrm{tot}\ v}^{JMPn\zeta}=\frac{1}{R}U_{Pn}^{Jv}(R)\Psi_{\mathrm{bend}}^{JMPn\zeta}(R,\theta,\eta_{je}) \tag{47}$$

where the stretch wavefunction is a solution to the one-dimensional Schrödinger equation:

$$\frac{-\hbar^2}{2\mu}\frac{\mathrm{d}^2}{\mathrm{d}R^2}U_{Pn}^{Jv}(R)+(V_{\mathrm{bend}}^{Pn}(R)+B(R)J(J+1))U_{Pn}^{Jv}(R)=E_{vJ}^{vr}(R). \tag{48}$$

Note that the energy eigenvalue to this equation contains the energy due to intermolecular stretch and bending vibration. The reason is that the bending potentials correlate with different diatom states (i.e. well-defined j and ω) while the minimum is determined by the value of P. For example, the potentials correlating with $j=\frac{3}{2}$ and $\omega=\pm\frac{1}{2}$ split under the electrostatic potential into bender potentials with $P=\frac{1}{2}$ and $P=\frac{3}{2}$. Because the main contribution to the rotational energy is given by a term depending on P, the bender potentials corresponding to a particular value of P are expected to lie close to each other.

3.3. *The body-fixed Hamiltonian: three-angle embedding*

The Hamiltonian for the three-angle embedding case is derived by transforming equation (1) to bf(3) coordinates defined by rotations through three Euler angles α,

β, and γ. Denoting the resulting rotation matrix $\mathbf{C}(\alpha, \beta, \gamma)$, the bf(3) coordinates are given by the equations

$$\mathbf{R}_{\mathrm{bf}} = \mathbf{C}\mathbf{R}_{\mathrm{sf}} = \begin{pmatrix} 0 \\ 0 \\ R \end{pmatrix}, \quad \mathbf{r}_{\mathrm{bf}} = \mathbf{C}\mathbf{r}_{\mathrm{sf}} = \begin{pmatrix} r\sin\theta \\ 0 \\ r\cos\theta \end{pmatrix}, \quad \text{and} \quad \eta_{j_{\mathrm{e}}} = \mathbf{C}\xi_{j_{\mathrm{e}}}. \tag{49}$$

Projecting the velocities onto the bf(3) axes, we introduce the angular velocity vector $\boldsymbol{\omega}$

$$\mathbf{C}\dot{\mathbf{a}}_{\mathrm{sf}} = \dot{\mathbf{a}}_{\mathrm{bf}} + \mathbf{C}\dot{\mathbf{C}}^{\dagger}\mathbf{a}_{\mathrm{bf}} = \dot{\mathbf{a}}_{\mathrm{bf}} + \boldsymbol{\omega} \times \mathbf{a}_{\mathrm{bf}}, \quad \text{with} \quad \boldsymbol{\omega} = \begin{pmatrix} -\cos\gamma\sin\beta\dot{\alpha} + \sin\gamma\dot{\beta} \\ \sin\gamma\sin\beta\dot{\alpha} + \cos\gamma\dot{\beta} \\ \cos\beta\dot{\alpha} + \dot{\gamma} \end{pmatrix}. \tag{50}$$

With these definitions, the kinetic energy now reads:

$$\begin{aligned} T = {} & \frac{\mu}{2}(\dot{R}^2 + R^2(\omega_x^2 + \omega_y^2)) + \frac{\mu_{\mathrm{bc}}}{2}(\dot{r}^2 + r^2((\omega_y + \dot{\theta})^2 + (\omega_z\sin\theta - \omega_x\cos\theta)^2)) \\ & + \frac{m_{\mathrm{e}}}{2}\sum_{j_{\mathrm{bc}}=1}^{N_{\mathrm{bc}}}(\dot{\eta}_{j_{\mathrm{bc}}} + \boldsymbol{\omega} \times \eta_{j_{\mathrm{bc}}})^2 + \frac{m_{\mathrm{e}}}{2}\sum_{j_{\mathrm{a}}=1}^{N_{\mathrm{a}}}(\dot{\boldsymbol{\rho}}_{j_{\mathrm{a}}} + \boldsymbol{\omega} \times \boldsymbol{\rho}_{j_{\mathrm{a}}})^2. \end{aligned} \tag{51}$$

In the usual way, the momenta conjugate to the generalized coordinates are determined as derivatives of the kinetic energy with respect to the corresponding velocities. The classicial Hamilton function is found by expressing the kinetic energy in terms of generalized coordinates and conjugate momenta:

$$\begin{aligned} H = {} & \frac{P_R^2}{2\mu} + \frac{P_r^2}{2\mu_{\mathrm{bc}}} + \frac{1}{2\mu R^2}((J_x^{\mathrm{bf}} - l_x^{\mathrm{bf}})^2 + (J_y^{\mathrm{bf}} - l_x^{\mathrm{bf}})^2 + 2\cot\theta(J_x^{\mathrm{bf}} - l_x^{\mathrm{bf}})(J_z^{\mathrm{bf}} - l_z^{\mathrm{bf}}) \\ & - 2(J_y^{\mathrm{bf}} - l_y^{\mathrm{bf}})j_\theta^{\mathrm{bf}} + j_\theta^{\mathrm{bf}^2} + \cot\theta(J_z^{\mathrm{bf}} - l_z^{\mathrm{bf}})^2) + \frac{1}{2\mu_{\mathrm{bc}}r^2}(j_\theta^{\mathrm{bf}^2} + \mathrm{cosec}^2\,\theta(J_z^{\mathrm{bf}} - l_z^{\mathrm{bf}})^2) \\ & + \sum_{j_{\mathrm{bc}}}\frac{\mathbf{p}_{j_{\mathrm{bc}}}^2}{2m_{\mathrm{e}}} + V_{\mathrm{BC}}(r, \theta, \eta_{j_{\mathrm{bc}}}) + \sum_{j_{\mathrm{a}}}\frac{\mathbf{p}_{j_{\mathrm{a}}}^2}{2m_{\mathrm{e}}} + V_{\mathrm{A}}(\eta_{j_{\mathrm{a}}}) + V_{\mathrm{int}}(R, \theta, \mathbf{r}, \eta_{j_{\mathrm{bc}}}, \eta_{j_{\mathrm{a}}}). \end{aligned} \tag{52}$$

The quantum mechanical analogue of equation (52) is determined by applying the Podolsky formula [88]:

$$\begin{aligned} H = {} & -\frac{\hbar^2}{2\mu R^2}\frac{\partial}{\partial R}R^2\frac{\partial}{\partial R} - \frac{\hbar^2}{2\mu_{\mathrm{bc}}r^2}\frac{\partial}{\partial r}r^2\frac{\partial}{\partial r} + \frac{(J_x^{\mathrm{bf}} - l_x^{\mathrm{bf}})^2 + (J_y^{\mathrm{bf}} - l_y^{\mathrm{bf}})^2}{2\mu R^2} \\ & + \cot\theta\frac{(J_x^{\mathrm{bf}} - l_x^{\mathrm{bf}})(J_z^{\mathrm{bf}} - l_z^{\mathrm{bf}}) + (J_z^{\mathrm{bf}} - l_z^{\mathrm{bf}})(J_x^{\mathrm{bf}} - l_x^{\mathrm{bf}})}{2\mu R^2} \\ & + \left(\frac{\mathrm{cosec}^2\,\theta}{2\mu_{\mathrm{bc}}r^2} + \frac{\cot^2\theta}{2\mu R^2}\right)(J_z^{\mathrm{bf}} - l_z^{\mathrm{bf}})^2 - \frac{1}{2\mu R^2}(J_y^{\mathrm{bf}} - l_y^{\mathrm{bf}})\frac{\hbar}{\mathrm{i}}\left(\frac{1}{\sin\theta}\frac{\partial}{\partial\theta}\sin\theta + \frac{\partial}{\partial\theta}\right) \\ & + \left(\frac{1}{2\mu_{\mathrm{bc}}r^2} + \frac{1}{2\mu R^2}\right)\left(\frac{-\hbar^2}{\sin\theta}\frac{\partial}{\partial\theta}\sin\theta\frac{\partial}{\partial\theta}\right) + V_{\mathrm{int}}(R, \theta, r, \eta_{j_{\mathrm{bc}}}, \eta_{j_{\mathrm{a}}}) \\ & - \sum_{j_{\mathrm{bc}}}\frac{\hbar^2}{2m_{\mathrm{e}}}\nabla_{j_{\mathrm{bc}}}^2 + V_{\mathrm{BC}}(r, \theta, \eta_{j_{\mathrm{bc}}}) - \sum_{j_{\mathrm{a}}}\frac{\hbar^2}{2m_{\mathrm{e}}}\nabla_{j_{\mathrm{a}}}^2 + V_{\mathrm{A}}(\eta_{j_{\mathrm{a}}}). \end{aligned} \tag{53}$$

Here, $\mathbf{J}^{\mathrm{bf}}$ represents the operator for the total angular momentum vector projected on to bf(3) axes. Its components obey anomalous commutation rules. The orbital angular momentum of the electrons $\mathbf{l}^{\mathrm{bf}}$ also refers to the bf(3) frame. It must be replaced with the total angular momentum $\mathbf{j}^{\mathrm{bf}}$ of the electrons, if the system has an odd number of electrons. The overall rotation of the complex and its bending vibration are coupled through terms involving the Jacobi angle θ and its conjugate operator. Since the bf(3) axes do not coincide with the principal axis system, we find cross terms involving the x and z components of the rotational angular momentum $\mathbf{J}^{\mathrm{bf}} - \mathbf{l}^{\mathrm{bf}}$ or in the case of non-vanishing spin $\mathbf{J}^{\mathrm{bf}} - \mathbf{j}^{\mathrm{bf}}$. This Hamiltonian was first derived for closed shell systems [96, 97] and later adapted for the calculation of the lower bound states ($J = \frac{1}{2}$) of the NO–Ar complex [98]. Since in this form all electronic coordinates are referred to the bf(3) frame, it is not possible to use directly a basis set which involves the eigenfunctions for the diatom. Therefore, it is more convenient to introduce a molecule-fixed frame attached to the diatom. The changes are completely analogous to the procedure outlined in section 3.1. In this case, the mf frame is connected to the bf(3) frame by a single rotation around the y-axis through the Jacobi angle θ. The additional rotation to the mf frame introduces the rotation angle θ and its time derivative into the expression for the kinetic energy of the electrons. Consequently, the correct form of the classical Hamiltonian function is derived by replacing in equation (52) the conjugate momentum j_θ^{mf} with $j_\theta^{\mathrm{mf}} = j_\theta^{\mathrm{bf}} + l_y$ and regarding the bf components of the electronic angular momentum as transformed mf components (note that in the transformation the y component is not affected):

$$
\begin{aligned}
H = {} & \frac{P_R^2}{2\mu} + \frac{P_r^2}{2\mu_{\mathrm{bc}}} + \frac{1}{2\mu R^2}\left((J_x^{\mathrm{bf}} - l_x^{\mathrm{bf}})^2 + (J_y^{\mathrm{bf}} - l_y^{\mathrm{bf}})^2 + 2\cot\theta (J_x^{\mathrm{bf}} - l_x^{\mathrm{bf}})(J_z^{\mathrm{bf}} - l_z^{\mathrm{bf}})\right. \\
& \left. - 2(J_y^{\mathrm{bf}} - l_y^{\mathrm{bf}})(j_\theta^{\mathrm{mf}} - l_y) + (j_\theta^{\mathrm{mf}} - l_y)^2 + \cot\theta (J_z^{\mathrm{bf}} - l_z^{\mathrm{bf}})^2\right) \\
& + \frac{1}{2\mu_{\mathrm{bc}} r^2}\left((j_\theta^{\mathrm{mf}} - l_y)^2 + \operatorname{cosec}^2\theta (J_z^{\mathrm{bf}} - l_z^{\mathrm{bf}})^2\right) \\
& + \sum_{j_{\mathrm{e}}} \frac{\mathbf{p}_{j_{\mathrm{e}}}^2}{2m_{\mathrm{e}}} + V_{\mathrm{BC}}(r, \boldsymbol{\rho}_{j_{\mathrm{bc}}}) + \sum_{j_{\mathrm{a}}} \frac{\mathbf{p}_{j_{\mathrm{a}}}^2}{2m_{\mathrm{e}}} + V_{\mathrm{A}}(\boldsymbol{\eta}_{j_{\mathrm{a}}}) + V_{\mathrm{int}}(R, \theta, \mathbf{r}, \boldsymbol{\eta}_{j_{\mathrm{bc}}}, \boldsymbol{\eta}_{j_{\mathrm{a}}})
\end{aligned}
$$

with

$$
\mathbf{l}^{\mathrm{bf}} = \mathbf{C}_{\mathrm{d}}^{-1}\mathbf{l}^{\mathrm{mf}} \quad \text{and} \quad \boldsymbol{\eta}_{j_{\mathrm{bc}}} = \mathbf{C}_{\mathrm{d}}^{-1}\boldsymbol{\rho}_{j_{\mathrm{bc}}}. \tag{54}
$$

The corresponding rigid rotor Hamiltonian is derived by introducing the conditions $\dot{r} = \dot{R} = \dot{\theta} = 0$. The first two imply simply the vanishing of the corresponding conjugate momenta. The last condition is equivalent to

$$
J_y^{\mathrm{bf}} - l_y = \left(1 + \frac{\mu R^2}{\mu_{\mathrm{bc}} r^2}\right) j_\theta^{\mathrm{bf}} = \left(1 + \frac{\mu R^2}{\mu_{\mathrm{bc}} r^2}\right)(j_\theta^{\mathrm{mf}} - l_y). \tag{55}
$$

On substituting this condition into the classical Hamiltonian function, we find the rigid rotor part of the Hamiltonian:

$$H_{\mathrm{rr}} = \frac{A'}{\hbar^2}(J_z^{\mathrm{bf}} - l_z^{\mathrm{bf}})^2 + \frac{B'}{\hbar^2}(J_x^{\mathrm{bf}} - l_x^{\mathrm{bf}})^2 + \frac{C'}{\hbar^2}(J_y^{\mathrm{bf}} - l_y^{\mathrm{bf}})^2 + \frac{D'}{\hbar^2}\left((J_x^{\mathrm{bf}} - l_x^{\mathrm{bf}})(J_z^{\mathrm{bf}} - l_x^{\mathrm{bf}}) + (J_z^{\mathrm{bf}} - l_z^{\mathrm{bf}})(J_x^{\mathrm{bf}} - l_x^{\mathrm{bf}})\right)$$

with

$$A' = \frac{\hbar^2 \cot^2\theta}{2\mu R^2} + \frac{\hbar^2 \mathrm{cosec}^2\theta}{2\mu_{\mathrm{bc}} r^2},\ B' = \frac{\hbar^2}{2\mu R^2},$$
$$C' = \frac{\hbar^2}{2}\frac{1}{\mu R^2 + \mu_{\mathrm{bc}} r^2}, \quad \text{and} \quad D' = \frac{\hbar^2 \cot\theta}{2\mu R^2}. \tag{56}$$

Since, in the present form, we have introduced electronic coordinates referring to the mf frame, we can define a basis set which makes use of the eigenfunctions of the diatom. On the other hand, we know that the interaction potential in equation (54) will be responsible for the coupling of different diatomic eigenstates, e.g. those states corresponding to $\lambda = \pm 1$ in the case of a diatom in a Π-state. This effective quenching of the electronic angular momentum can be mimicked by adding a term defining a quenching parameter ε:

$$H_{\mathrm{q}} = \varepsilon((l_+^{\mathrm{mf}})^{2\lambda} + (l_-^{\mathrm{mf}})^{2\lambda}). \tag{57}$$

Since the interaction potential does not act on the spin coordinates, the quenching remains unchanged when the electron spin is introduced. On the other hand, the rigid rotor term will involve the total electronic angular momentum $\mathbf{j}^{\mathrm{mf}}$ instead of the orbital angular momentum $\mathbf{l}^{\mathrm{mf}}$. Therefore, we introduce the electron spin by replacing $\mathbf{l}^{\mathrm{bf}}$ with $\mathbf{l}^{\mathrm{bf}} + \mathbf{s}^{\mathrm{bf}}$. In this form, the rigid rotor structure is defined directly in terms of the Jacobi coordinates R, r, and θ. On the other hand, complications in the calculation of the energy levels due to the cross term in D' are avoided, if we transform the rigid rotor part of equation (56) to the principal axis frame introducing the principal moments of inertia A, B, and C. The complete model Hamiltonian takes on the following form:

$$H = H_{\mathrm{rr}} + H_{\mathrm{q}} + H_{\mathrm{so}}$$
$$\text{with} \quad H_{\mathrm{rr}} = \frac{A}{\hbar^2}(J_x^{\mathrm{bf}} - l_z^{\mathrm{bf}} - s_z^{\mathrm{bf}})^2 + \frac{B}{\hbar^2}(J_x^{\mathrm{bf}} - l_x^{\mathrm{bf}} - s_x^{\mathrm{bf}})^2 + \frac{C}{\hbar^2}(J_y^{\mathrm{bf}} - l_y^{\mathrm{bf}} - s_y^{\mathrm{bf}})^2$$
$$\text{and} \quad \mathbf{l}^{\mathrm{bf}} = \mathbf{C}_{\mathrm{d}}^{-1}\mathbf{l}^{\mathrm{mf}}, \mathbf{s}^{\mathrm{bf}} = \mathbf{C}_{\mathrm{d}}^{-1}\mathbf{s}^{\mathrm{mf}} \tag{58}$$

where H_{q} has been defined in equation (57). The above Hamiltonian contains also a term H_{so} representing the spin–orbit interaction in the diatom:

$$H_{\mathrm{so}} = a_{\mathrm{so}}\mathbf{l}^{\mathrm{mf}} \cdot \mathbf{s}^{\mathrm{mf}}. \tag{59}$$

The Hamiltonian of equation (58) was first used by Mills *et al.* in their analysis of the microwave spectrum of the NO–Ar complex, i.e. for the excitation within a Π-state. These authors included additional terms into the Hamiltonian to account for various nuclear spin interactions. Since the resolution of our IR and UV spectra does not allow us to resolve any hyperfine structure, we will neglect these terms and refer the reader to the original literature [63, 64, 99]. Subsequently, this model was extended by Fawzy and Hougen to one-photon transitions involving different electronic states [100] and by Meyer to two-photon transitions [17].

When the components of the electronic angular momentum operators are expressed in terms of the corresponding mf components, we can derive a matrix representation of the approximate Hamiltonian by using as basis set products of the electronic part of the diatomic eigenfunctions $|n\lambda\rangle|s\sigma\rangle$ and eigenfunctions $|JMP\rangle$ of the total angular momentum operator, i.e. rotation matrix elements depending on the Euler angles α, β, and γ. They are characterized by the quantum number J of the total angular momentum and the projection quantum numbers M and P. The electronic wavefunction of the diatom is defined through the orbital angular momentum projection λ and the total spin quantum number s and its projection σ onto the mf z-axis. The action of the parity operator E^* is as follows:

$$E^*|JMP\rangle = (-)^{J-P}|JM-P\rangle, \quad E^*|s\sigma\rangle = (-)^{s-\sigma}|s-\sigma\rangle \quad \text{and}$$

$$E^*|n\lambda\rangle = (-)^{\lambda+h}|n-\lambda\rangle \quad (h = 1 \text{ for } \Sigma^- \text{ states}, h = 0 \text{ otherwise}). \tag{60}$$

Since the overall parity must be a good quantum number, we use basis states with a well defined parity η:

$$|JMP\omega\eta\rangle = \frac{1}{\sqrt{2}}(|JMP\rangle|n\lambda\rangle|s\sigma\rangle + \eta(-)^{J-P+\lambda+h+s-\sigma}|JM-P\rangle|n-\lambda\rangle|n-\lambda\rangle|s-\sigma\rangle)$$

$$\text{with} \quad \eta = \pm 1 \quad \text{and} \quad \omega = \lambda + \sigma. \tag{61}$$

This is the rigid rotor analogue of the $(P\omega)$-basis set defined in equation (31). As before, we restrict P to positive values while λ and σ are treated as signed quantum numbers. To see that η is indeed the parity of the basis state defined in equation (61), we apply the operator E^*:

$$E^*|JMP\lambda\sigma\eta\rangle = \frac{1}{\sqrt{2}}((-)^{J-P+\lambda+h+s-\sigma}|JM-P\rangle|n-\lambda\rangle|s-\sigma\rangle + \eta|JMP\rangle|n\lambda\rangle|s\sigma\rangle)$$

$$= \eta|JMP\lambda\sigma\eta\rangle. \tag{62}$$

Matrix elements of the model Hamiltonian for terms involving x and y components of the different angular momenta are more easily evaluated when we introduce shift operators. Let A_x, A_y, and A_z be operators which obey normal or anomalous angular momentum commutation rules:

$$A_+ = A_x + \mathrm{i}A_y, \quad A_- = A_x - \mathrm{i}A_y \quad \text{or} \quad A_x = \frac{1}{2}(A_+ + A_-), \quad A_y = \frac{1}{2\mathrm{i}}(A_+ - A_-). \tag{63}$$

Since we are mainly interested in the rotational structure, i.e. terms involving the components of $\mathbf{J}^{\mathrm{bf}}$, several terms are recognized to result in a constant contribution to the electronic energy. Terms involving the shift operators $l_\pm$ are responsible for the mixing of different electronic states. Since the first excited Σ-state lies much higher in energy ($44\,000\,\mathrm{cm}^{-1}$) than the electronic ground state, we neglect these terms. We also neglect the terms involving the anti-commutators of $l_\pm$ and $s_\pm$, since they do not affect the rotational structure. Furthermore, terms involving the square of the shift operators $s_\pm$ cannot contribute for states with $s = \frac{1}{2}$ while terms proportional to l_z^2 and s_z^2 only cause a shift of the overall energy. Therefore, the rotational structure of the energy level pattern can be described by the following approximate rigid rotor Hamiltonian:

$$H_{\mathrm{rr}} = \left(A - \frac{B+C}{2}\right) J_z^2 + \frac{B+C}{2} J^2 + \frac{B-C}{4}(J_+^2 + J_-^2) - 2\cos\theta A J_z(l_z + s_z)$$

$$+ 2(\cos^2\theta A + \sin^2\theta B) s_z l_z + \sin\theta A J_z(s_+ + s_-)$$

$$- \frac{\cos\theta B - C}{2}(J_+ s_+ + J_- s_-) - \frac{\cos\theta B + C}{2}(J_+ s_- + J_- s_+)$$

$$- \sin\theta B(l_z + s_z)(J_+ + J_-) - \sin\theta\cos\theta(A - B)(s_+ + s_-) l_z. \quad (64)$$

The matrix elements of this Hamiltonian are easily evaluated in the symmetrized basis set defined in equation (61). As expected, they are diagonal in the parity index η. The eigenvalues and eigenfunctions are determined by numerical diagonalization of the matrix representation of the Hamiltonian defined in equations (58) and (64). The resulting eigenfunctions are given in terms of the basis set

$$|JM\eta n\tau\rangle = \sum_{P,\omega} C_{P\omega}^{J\eta n\tau} |JMP\omega\eta\rangle \quad \text{and} \quad \omega = \lambda + \sigma. \quad (65)$$

4. Application to NO–X (X=Ne, Ar): $\tilde{X}^2\Pi$

4.1. *Perturbation theory and effective Hamiltonian*

Ideally, the experimental spectra are compared with the results of complete *ab-initio* treatments. In this way, deficiencies of the used potential surfaces or the applied methods for the bound state calculation can be assessed. On the other hand, it is usually not straightforward to relate discrepancies between experimental and calculated spectra to specific features of the potential or to different correction terms in the Hamiltonian. Therefore, it is highly desirable to generate such complementary information by defining an empirical Hamiltonian which incorporates various interactions represented by different parameters. In this approach, the parameters representing the results of a bound state calculation can be compared with parameters resulting from a fit of the experimental spectra. Differences are related directly to the corresponding interaction terms. Perturbation theory can be applied to construct the empirical Hamiltonian and to gain additional insight into the energy level structure of the complex. Such an approach was developed successfully by Green and Lester [84]. Since the matrix representation of the potential in equation (37) still contains diagonal elements, we can use the leading term with $\tilde{l} = 0$ to define a zeroth order stretch Hamiltonian which is used to determine the associated vibrational energy:

$$\left\{-\frac{\hbar^2}{2\mu}\frac{\mathrm{d}^2}{\mathrm{d}R^2} + V_{00}(R)\right\} U_{v_s}(R) = E_{\mathrm{vib}\,v_s}^{(0)} U_{v_s}(R)$$

$$\text{with} \quad E_{\mathrm{vib}\,v_s}^{(0)} = E_{\mathrm{tot}\,j\omega}^{JPv_s} - E_{j\omega}^{(\mathrm{BC})} - B(J(J+1) + j(j+1) - 2P^2). \quad (66)$$

In first order, only expansion terms of the average potential make a contribution to the energy. For the signed $(P\omega)$ basis set, we find for the energy $E_{\mathrm{tot}\,j\omega}^{JPv_s}$ an expression identical to the one given in equation (27). The electrostatic interaction splits the free rotor energy level (for a given j) into sublevels characterized by the product $P\omega$. Since

P is restricted to positive values, we expect $j+\frac{1}{2}$ different P levels. Each level will be split further into two levels corresponding to the different sign of ω. This results in a total of $2j+1$ levels.

For a given value of P, the main contribution to the ω splitting results from the leading term $V_{10}(R)$. Upon replacing in equation (27) $+\omega$ with $-\omega$, we find

$$(-)^{\omega}\begin{pmatrix} j & 1 & j \\ \omega & 0 & -\omega \end{pmatrix} V_{10}(R) = -(-)^{-\omega}\begin{pmatrix} j & 1 & j \\ -\omega & 0 & \omega \end{pmatrix} V_{10}(R). \tag{67}$$

Since the two ω-levels are shifted in first order by the same amount but in opposite directions, the splitting is proportional to $2\langle v_s|V_{10}(R)|v_s\rangle$. Because the contribution due to the term $V_{20}(R)$ is independent of the sign of P and ω, it cannot remove the degeneracy of the $\pm\omega$ levels. Thus, in the absence of a V_{10} term, the free rotor level $(j,|\omega|)$ is split into $J+\frac{1}{2}$ sublevels corresponding to the possible values of $|P|$.

Even if the degeneracy of the $\pm\omega$ levels is removed, each level is still two-fold degenerate in the quantum number ζ. As suggested by Green and Lester, the P-type doubling can be explained also within the framework of perturbation theory [84]. Since the matrix elements for Coriolis coupling (see equation (35)) of states with $P=P'=\frac{1}{2}$ and $\omega'=-\omega$ are linear in η, any perturbation resulting in P-type doubling must be of odd order in the Coriolis coupling. On the other hand, its matrix elements are not diagonal in ω so that other ω-changing perturbations such as spin uncoupling and the difference potential must be invoked for the perturbation theoretical treatment. While for states with $P=\frac{1}{2}$ the degeneracy can be removed by first-order Coriolis coupling, at least third-order Coriolis coupling must be invoked for levels with $P>\frac{1}{2}$. Because the lowest bound levels for NO–Ar involve basis states with $\omega=\pm\frac{1}{2}$ and $P=\frac{1}{2}$, we can explain the splitting by a mechanism involving the difference potential as well as the spin-uncoupling operator:

$$\langle J\tfrac{1}{2}\eta j\tfrac{1}{2}|H^{(1)}_{\mathrm{rot}}|J\tfrac{1}{2}\eta' j'-\tfrac{1}{2}\rangle\langle J\tfrac{1}{2}\eta j-\tfrac{1}{2}|V_{\mathrm{diff}}|J\tfrac{1}{2}\eta' j'\tfrac{3}{2}\rangle\langle J\tfrac{1}{2}\eta j\tfrac{3}{2}|H^{(1)}_{\mathrm{BC}}|J\tfrac{1}{2}\eta' j'\tfrac{1}{2}\rangle = (J+\tfrac{1}{2})C_1. \tag{68}$$

For levels with $|\omega|=P=\frac{1}{2}$, we expect a strong P-type doubling increasing linearly with $J+\frac{1}{2}$. Much smaller effects are expected for levels with $P>\frac{1}{2}$ [83]. For states with $P=\frac{3}{2}$, we have to invoke two additional Coriolis couplings: one to reduce P from $\frac{3}{2}$ to $\frac{1}{2}$ and one, in the last step, to increase P again by one unit. Because we pick up a factor $(J+\frac{1}{2})$ each time we apply the Coriolis coupling operator, the parity splitting of a $(P=\frac{3}{2})$-level is expected to vary as $(J+\frac{1}{2})^3$. Within the CD approximation, all Coriolis interactions are neglected and no P-type doubling results. In conclusion, we find that the ω-splitting is closely related to the odd expansion terms of the average potential while the P-type doubling involves contributions from the difference potential.

Applying the results from the perturbation theory outlined above, we expect the energy levels of the open shell complexes to be well described by an expression of the following type:

$$\begin{aligned} E^{JPv_s}_{\mathrm{tot}\,\omega} = {} & E_{Pv_b\,v_s} + BJ(J+1) - D[J(J+1)]^2 + \cdots \\ & - \frac{P\omega}{|P\omega|}\{V_0 + V_1(J+\tfrac{1}{2}) + V_2(J+\tfrac{1}{2})^2 + \cdots \\ & + \zeta[C^{\omega}_0 + C^{\omega}_1(J+\tfrac{1}{2}) + C^{\omega}_2(J+\tfrac{1}{2})^2 + \cdots]\}. \end{aligned} \tag{69}$$

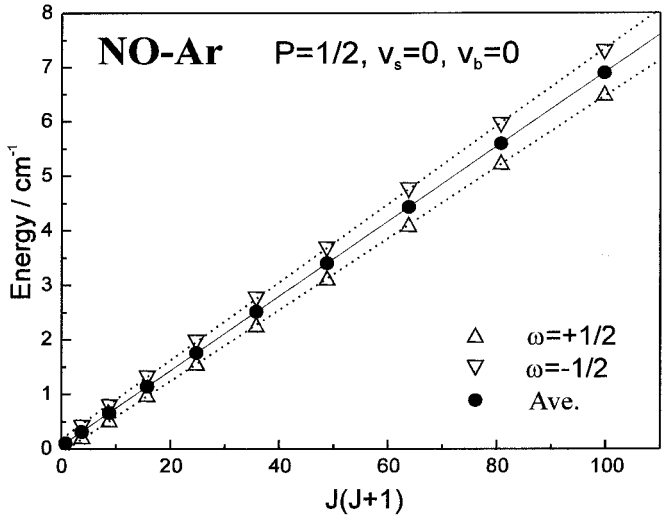

Figure 10. Bound state energies for the vibrational ground state of the NO–Ar complex. The open triangles represent the energy averaged over the two *P*-type components for $\omega = \pm\frac{1}{2}$. The solid circles represent the rotational energy.

The different constants for the complexes of NO with Ne and Ar are determined in a least squares fit of the energies calculated by Alexander in a full quantum mechanical bound state calculation [32, 35]. The results for NO–Ar are displayed in figures 10–12 and compiled in table 1. Using these constants, most energy levels are reproduced within 0.01 cm^{-1}. Slightly larger deviations occur for several levels with $J = \frac{1}{2}$. For a particular vibrational level, the main contribution to the energy is given by the rotational energy term. As can be seen in figure 10 for the energy levels of the NO–Ar complex, no centrifugal distortion effects are noticeable. In figure 11, we display the ω-splitting of the levels as a function of *J*. Within the CD approximation, the splitting is independent of *J* consistent with the results of first-order perturbation theory. On the other hand, the full calculation yields a pronounced linear *J*-dependence of the splitting. Since the two types of calculations differ only in the treatment of the Coriolis coupling, we conclude that the *J*-dependence in the ω-splitting is mediated by Coriolis coupling which in turn implies a contribution from the difference potential. This assessment is confirmed by the analysis of the rotational levels for the bending state corresponding to $P = \frac{3}{2}$ as shown in figure 12. For these states Coriolis coupling can only contribute in higher order resulting in a nearly constant ω-splitting and an extremely small *P*-type doubling.

The situation is quite similar for the NO–Ne complex [36]. Because this complex is less strongly bound, small centrifugal distortion effects become apparent already for intermediate *J* values. Apart from a small quadratic *J*-dependence, the ω-splitting is almost independent of *J* for all vibrational states. Again the *J*-dependence of the splitting is much larger for levels with $P = \frac{1}{2}$ than for levels with $P = \frac{3}{2}$. Similarly, the *P*-type doubling constants for the $P = \frac{3}{2}$ levels are considerably reduced compared to the ones found for the $P = \frac{1}{2}$ levels. Interestingly, we find these constants to be ω-dependent.

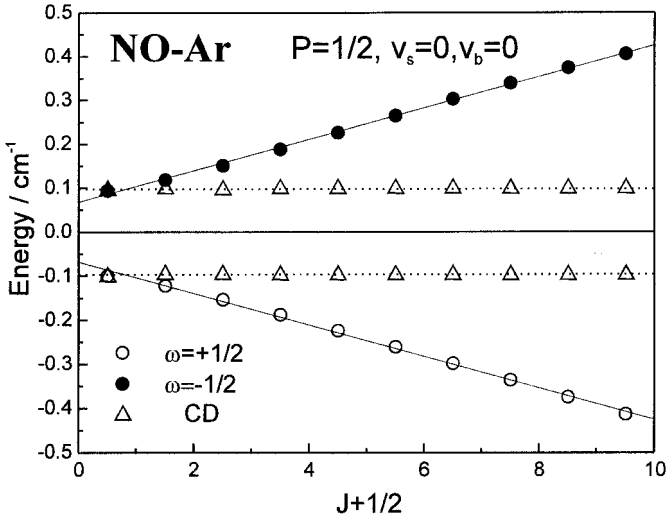

Figure 11. The ω-splitting of the rotational energy levels for the ground vibrational state of NO–Ar. Circles represent the result for the different ω levels. The triangles are the result for the CD approximation.

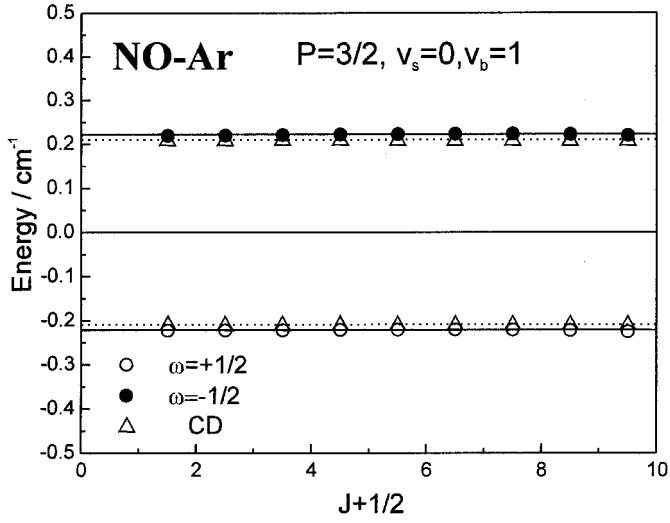

Figure 12. The ω-splitting of the rotational energy levels for the first excited vibrational state of NO–Ar with $P = \frac{3}{2}$. Circles represent the result for the different ω levels. The triangles are the result for the CD approximation.

Table 1. Constants (in cm^{-1}) for the effective Hamiltonian for the electronic ground state levels of the NO–Ar complex correlating with NO $X\,^2\Pi(v = 0)$. The constants are based on the results of the bound state calculations of [35].

Band	$E_{P v_b v_s}$	B	V_0	$V_1/10^{-2}$	$V_2/10^{-2}$	$C_0/10^{-2}$
A	0	0.0686	0.050	3.57	0.00	2.26
B	3.683	0.0689	0.221	0.00	0.00	0.00
C	14.310	0.0628	0.577	0.00	0.93	0.05

4.2. *One-photon linestrength*

The calculation of the intensity for a one-photon transition between two levels, $|i\rangle$ and $|f\rangle$ in a van der Waals complex has been discussed in detail previously [35, 82, 101]. Within the framework of first-order time-dependent perturbation theory, the intensity is given by the expression

$$I(i \to f) = C \sum_{M',M''} |\tilde{S}_{if}|^2 \quad \text{with} \quad \tilde{S}_{if} = \langle f|\boldsymbol{\mu}\cdot\mathbf{E}|i\rangle = \left\langle f \left| \sum_{m=0,\pm1} \mu_m^{(1)} e_m^{(1)^*} \right| i \right\rangle. \quad (70)$$

Here, we have expressed the dot product between the dipole moment operator $\boldsymbol{\mu}$ and the electric field vector $\mathbf{E}$ in terms of spherical tensor components. Because the involved wavefunctions depend on the electronic coordinates defined with respect to the mf frame, it is convenient to express the components of the dipole moment operator also in terms of its mf components. For this purpose, we first introduce its bf(2) components and then its mf components taking advantage of the transformation properties of spherical tensor operators (see, for example [102]):

$$\mu_m^{(1)}(\text{lab}) = \sum_k \mu_k^{(1)}(\text{bf}) D_{mk}^{(1)^*}(\hat{\boldsymbol{R}}) = \sum_{k\tilde{k}} \mu_{\tilde{k}}^{(1)}(\text{mf}) D_{k\tilde{k}}^{(1)^*}(\hat{\boldsymbol{r}}) D_{mk}^{(1)^*}(\hat{\boldsymbol{R}})$$

$$\text{with} \quad \hat{\boldsymbol{R}} = (\alpha, \beta, 0) \quad \text{and} \quad \hat{\boldsymbol{r}} = (\phi, \theta, 0). \quad (71)$$

Since, in our experiments, we work with initially unaligned ensembles and linearly polarized laser light, we choose our laboratory frame z axis along the direction of linear polarization of the laser. In this case, $e_0^{(1)} = E_z$ is the only non-vanishing tensor component. Furthermore, for an IR transition in a diatomic molecule involving two Π-states, the transition moment must be parallel to the internuclear axis yielding as the only non-vanishing component $\mu_0^{(1)}(\text{mf})$:

$$\mu_0^{(1)}(\text{lab}) = \sum_k \mu_0^{(1)}(\text{mf}) D_{k0}^{(1)^*}(\hat{\boldsymbol{r}}) D_{0k}^{(1)^*}(\hat{\boldsymbol{R}}). \quad (72)$$

In the following, we calculate the transition matrix elements $\tilde{S}_{if}$ within the CD approximation (see equation (45)) for which P is a good quantum number. Using the transformed mf transition moment operator of equation (72), we find

$$\tilde{S}_{if} = \sum_{n'j'\omega'} \sum_{n''j''\omega''} \sum_k \langle J'M'P'\zeta'j'\omega'|\mu_0^{(1)}(\text{mf}) D_{k0}^{(1)^*}(\hat{\boldsymbol{r}}) D_{0k}^{(1)^*}(\hat{\boldsymbol{R}})|J''M''P''\zeta''j''\omega''\rangle$$

$$\times \langle U_{P'n'}^{J'v'}(R) W_{j'\omega'}^{P'n'}(R) \frac{1}{R^2} U_{P''n''}^{Jv}(R) W_{j''\omega''}^{P''n''}(R)\rangle. \quad (73)$$

The different contributions to the matrix elements contain an integral which involves electronic and angular coordinates, and a Franck–Condon type integral over the stretch coordinate. While the latter can only be evaluated once the different radial coefficients are known, the angular part can be evaluated analytically. Using the definition of the $(P\omega)$-signed basis states, we find after some algebra

$$\sum_k \langle J'M'P'\zeta'j'\omega'|\mu_0^{(1)} D_{k0}^{(1)^*}(\hat{r}) D_{0k}^{(1)^*}(\hat{\boldsymbol{R}})|J''M''P''\zeta''j''\omega''\rangle$$

$$= \delta_{M'M''}[J'][J''][j'][j''](-)^{M'-\omega'}\mu_0^{(1)} \begin{pmatrix} J' & 1 & J'' \\ M' & 0 & -M' \end{pmatrix} \begin{pmatrix} j' & 1 & j'' \\ \omega' & 0 & -\omega' \end{pmatrix}$$

$$\times \frac{1+\zeta'\zeta''(-)^{J'+J''}}{2} \sum_k \left\{ \delta_{\omega'\omega''} \begin{pmatrix} J' & 1 & J'' \\ P' & -k & -P'' \end{pmatrix} \begin{pmatrix} j' & 1 & j'' \\ P' & -k & -P'' \end{pmatrix} \right.$$

$$\left. + \zeta'' \begin{pmatrix} J' & 1 & J'' \\ P' & -k & P'' \end{pmatrix} \begin{pmatrix} j' & 1 & j'' \\ P' & -k & P'' \end{pmatrix} \delta_{\omega'-\omega''} \right\}. \tag{74}$$

Here we have introduced the transition dipole matrix element involving states with $\lambda = 1 : \mu_0^{(1)} = \langle 1|\mu_0^{(1)}(\mathrm{mf})|1\rangle$. The 3$j$-symbols in equation (74) enforce the usual one-photon selection rules $\Delta J = 0, \pm 1$. Because the parity of the wavefunction is given by $\eta = \zeta(-)^{J-\frac{1}{2}}$, we find the parity selection rule:

$$1 + \zeta'\zeta''(-)^{J'+J''} = 1 - \eta'\eta'' \Rightarrow \eta' = -\eta''. \tag{75}$$

As expected for a one-photon transition, the parity of the involved states must change. Since the quantum number P in the $(P\omega)$-basis set is restricted to positive values, the last term in equation (74) can only contribute for $P' = P'' = \frac{1}{2}$ and $k = +1$ giving rise to a perpendicular transition. On the other hand, the first term is responsible for parallel ($k = 0$ and $\Delta P = 0$) or perpendicular contributions ($k = +1$ and $\Delta P = \pm 1$). In the molecular beam environment only the lowest vibrational level corresponding to $P = \frac{1}{2}$ is populated. Therefore, we need to consider only transitions with $P'' = \frac{1}{2} \rightarrow P' = \frac{1}{2}$ and $P'' = \frac{1}{2} \rightarrow P' = \frac{3}{2}$. For the latter case, we separate out the summation over the different basis states and define an R-dependent transition moment function $\mu_{n'n''}^{(3)}(R)$:

$$\mu_{n'n''}^{(3)}(R) = \sum_{j'\omega'} \sum_{j''} [j'][j''](-)^{-\omega'} \begin{pmatrix} j' & 1 & j'' \\ \omega' & 0 & -\omega' \end{pmatrix} \begin{pmatrix} j' & 1 & j'' \\ \frac{3}{2} & -1 & -\frac{1}{2} \end{pmatrix} W_{j'\omega'}^{P'n'} W_{j''\omega'}^{P''n''}. \tag{76}$$

The intensity can now be written in the following form:

$$I_{\frac{1}{2}\rightarrow\frac{3}{2}} = \frac{[J']^2[J'']^2\delta_{\eta'-\eta''}}{3} \begin{pmatrix} J' & 1 & J'' \\ \frac{3}{2} & -1 & -\frac{1}{2} \end{pmatrix}^2 [\mu_0^{(1)}]^2$$

$$\times \left| \sum_{n'n''} \left\langle U_{P'n'}^{J'v'}(R) \mu_{n'n''}^{(3)}(R) U_{P''n''}^{J''v''}(R) \frac{1}{R^2} \right\rangle \right|^2. \tag{77}$$

For the transition between levels with $P = \frac{1}{2}$, we have to take into account the parallel and the perpendicular contributions. In analogy with equation (76), we define the transition moments:

$$\mu_{n'n''}^{(1||)}(R) = \sum_{j'\omega'} \sum_{j''} [j'][j''](-)^{-\omega'} \begin{pmatrix} j' & 1 & j'' \\ \omega' & 0 & -\omega' \end{pmatrix} \begin{pmatrix} j' & 1 & j'' \\ \frac{1}{2} & 0 & -\frac{1}{2} \end{pmatrix} W_{j'\omega'}^{P'n'} W_{j''\omega'}^{P''n''} \tag{78}$$

and

$$\mu^{(1\perp)}_{n'n''}(R) = \sum_{j'\omega'}\sum_{j''}[j'][j''](-)^{-\omega'}\begin{pmatrix} j' & 1 & j'' \\ \omega' & 0 & -\omega' \end{pmatrix}\begin{pmatrix} j' & 1 & j'' \\ \frac{1}{2} & -1 & \frac{1}{2} \end{pmatrix} W^{P'n'}_{j'\omega'} W^{P''n''}_{j''-\omega'}. \quad (79)$$

The intensity distribution for this case is given by a superposition of contributions due to these two moments:

$$I_{\frac{1}{2}\to\frac{1}{2}} = \frac{[J']^2[J'']^2\delta_{\eta'-\eta''}}{3}[\mu^{(1)}_0]^2\left|\sum_{n'n''}\begin{pmatrix} J' & 1 & J'' \\ \frac{1}{2} & 0 & -\frac{1}{2} \end{pmatrix}\left\langle U^{J'v'}_{P'n'}(R)\mu^{(1||)}_{n'n''}(R)U^{J''v''}_{P''n''}(R)\frac{1}{R^2}\right\rangle\right.$$
$$\left. +\eta''\begin{pmatrix} J' & 1 & J'' \\ \frac{1}{2} & -1 & \frac{1}{2} \end{pmatrix}\left\langle U^{J'v'}_{P'n'}(R)\mu^{(1\perp)}_{n'n''}(R)U^{J''v''}_{P''n''}(R)\frac{1}{R^2}\right\rangle\right|^2. \quad (80)$$

Because there are two contributions to bands with $P' = P'' = \frac{1}{2}$, we can expect interference effects between different adiabatic bender states contributing to the CD wavefunction. The perpendicular component is responsible for transition between basis states with large coefficients for ω'' and $\omega' = -\omega''$ while the parallel component connects states which are dominated by expansion terms with $\omega' = \omega''$. For the case of identical potential surfaces correlating with different vibrational states of NO, e.g. NO($v = 0$) and NO($v = 2$), the perpendicular moment in equation (80) is very small resulting in weak Q-branches.

In order to simulate the rotational structure for transitions between different vibrational levels without explicit knowledge of the complete wavefunction, we calculate an approximate linestrength based on the adiabatic bender treatment. In this case the intensity is shown to be governed by a vibrational transition moment for the stretch vibration and a purely rotational contribution which is similar to the one for a symmetric top molecule. The involved matrix elements for the R-dependent transition moments $\mu^{(1\perp)}_{n'n''}$, $\mu^{(1||)}_{n'n''}$, and $\mu^{(3)}_{n'n''}$ are simply incorporated into overall scaling factors $C_{\omega'\omega''}$. Note that ω is only approximately a good quantum number in this treatment

$$I_{\frac{1}{2}\to\frac{3}{2}} = \frac{[J']^2[J'']^2\delta_{\eta'-\eta''}}{3}[\mu^{(1)}_0]^2\begin{pmatrix} J' & 1 & J'' \\ \frac{3}{2} & -1 & -\frac{1}{2} \end{pmatrix}^2$$

and

$$I_{\frac{1}{2}\to\frac{1}{2}} = \frac{[J']^2[J'']^2\delta_{\eta'-\eta''}}{3}[\mu^{(1)}_0]^2\left|\begin{pmatrix} J' & 1 & J'' \\ \frac{1}{2} & 0 & -\frac{1}{2} \end{pmatrix}C^{\parallel}_{\omega'\omega''} + \eta''\begin{pmatrix} J' & 1 & J'' \\ \frac{1}{2} & -1 & \frac{1}{2} \end{pmatrix}C^{\perp}_{\omega'\omega''}\right|^2. \quad (81)$$

The coefficient $C^{\perp}_{\omega'\omega''}$ is usually very small for $\omega' \neq \omega''$ because of the orthogonality of the adiabatic stretch vibrational wavefunctions. Nevertheless, this term allows us to test the perpendicular character of the transition.

At this point it is interesting to compare these results with the ones based on the rigid rotor approximation. Using the analogous signed $(P\omega)$-basis set for the rigid rotor, we can calculate the intensity for the one-photon transition. Because the involved wavefunctions depend on the electronic coordinates defined with respect to the mf frame, we must express the components of the dipole moment operator again in terms of its mf components. For this purpose, we first introduce its bf(3) components and then its mf components:

$$\mu_0^{(1)}(\mathrm{sf}) = \sum_k \mu_0^{(1)}(\mathrm{mf}) D_{k0}^{(1)^*}(\hat{\boldsymbol{r}}) D_{0k}^{(1)^*}(\hat{\boldsymbol{R}}) = \sum_k \mu_0^{(1)}(\mathrm{mf}) d_{k0}^{(1)}(\theta) D_{0k}^{(1)^*}(\hat{\boldsymbol{R}})$$

$$\text{with} \quad \hat{\boldsymbol{R}} = (\alpha, \beta, \gamma) \quad \text{and} \quad \hat{\boldsymbol{r}} = (0, \theta, 0). \tag{82}$$

The comparison with the corresponding transformation for the two-angle embedding case reveals that the third rotation through the Euler angle γ is identical to the first rotation of the mf frame through the angle ϕ within the bf(2) formalism.

In the following, we calculate the transition matrix elements $\tilde{S}_{if}$ for two different rigid rotor states $|J'M\eta'n'\tau'\rangle$ and $|J''M\eta''n''\tau''\rangle$. Using the transformed mf transition moment operator of equation (82), we find

$$\begin{aligned}\tilde{S}_{if} &= \sum_{kP'\omega'P''\omega''} C_{P'\omega'}^{J'\eta'\tau'} C_{P''\omega''}^{J''\eta''\tau''} d_{k0}^{(1)}(\theta) \langle J'MP'\omega'\eta' | \mu_0^{(1)}(\mathrm{mf}) D_{0k}^{(1)^*}(\alpha,\beta,\gamma) | J''MP''\omega''\eta''\rangle \\ &= \delta_{\eta'-\eta''}[J'][J''](-)^M \begin{pmatrix} J' & 1 & J'' \\ M & 0 & -M \end{pmatrix} \mu_0^{(1)} \sum_{P'\omega'p''\omega''} C_{P'\omega'}^{J'\eta'\tau'} C_{P''\omega''}^{J''\eta''\tau''} (-)^{-P'} \Bigg\{ \delta_{\omega'\omega''} d_{P'-P''0}^{(1)}(\theta) \\ &\quad \times \begin{pmatrix} J' & 1 & J'' \\ P' & P''-P' & -P'' \end{pmatrix} + \delta_{\omega'-\omega''} \eta'' (-)^{J''+\sigma''} d_{10}^{(1)}(\theta) \begin{pmatrix} J' & 1 & J'' \\ P' & -1 & P'' \end{pmatrix} \Bigg\}. \end{aligned} \tag{83}$$

In the last line of (83), we have made use of the fact that the second term can only contribute for $P' = P'' = \frac{1}{2}$. The overall intensity of the rotational line is found by substituting this result into equation (70) and summing over all magnetic sublevels:

$$\begin{aligned} I_{i\to f} = \frac{1}{3} \delta_{\eta'-\eta''} [J']^2 [J'']^2 [\mu_0^{(1)}]^2 \Bigg| \sum_{P'\omega'P''\omega''} C_{P'\omega'}^{J'\eta'\tau'} C_{P''\omega''}^{J''\eta''\tau''} (-)^{-P'} \Bigg\{ \delta_{\omega'\omega''} d_{P'-P''0}^{(1)}(\theta) \\ \times \begin{pmatrix} J' & 1 & J'' \\ P' & P''-P' & -P'' \end{pmatrix} + \delta_{\omega'-\omega''} \eta'' (-)^{J''+\sigma''} d_{10}^{(1)}(\theta) \begin{pmatrix} J' & 1 & J'' \\ P' & -1 & P'' \end{pmatrix} \Bigg\} \Bigg|^2 . \end{aligned} \tag{84}$$

The first d-function vanishes for a T-shaped complex, if $P' = P''$. Therefore, bands with $P' = P'' = \frac{1}{2}$ have exclusively perpendicular character. This is reasonable, since for $\theta = 90^\circ$, the transition moment in the monomer is perpendicular to the z-axis of the principal axis system which nearly coincides with the direction of $\mathbf{R}$.

Assuming P to be a good quantum number, we find an expression for the intensity very similar to the approximate linestrength derived for the bf(2) formulation. As before, we restrict the discussion to transitions starting in ground state levels with $P'' = \frac{1}{2}$. The rotational structure of perpendicular bands can therefore be approximated as follows:

$$I_{\frac{1}{2}\to\frac{3}{2}} = \delta_{\eta'-\eta''} [J']^2 [J'']^2 [\mu_0^{(1)}]^2 \Bigg| \sum_{\omega'} C_{P'\omega'}^{J'\eta'\tau'} C_{P''\omega'}^{J''\eta''\tau''} d_{10}^{(1)}(\theta) \begin{pmatrix} J' & 1 & J'' \\ \frac{3}{2} & -1 & -\frac{1}{2} \end{pmatrix} \Bigg|^2 . \tag{85}$$

The rotational structure of bands with $\Delta P = 0$ is determined by the interference of two different contributions. The relative magnitude of each contribution is determined by the d-function which introduces the structural dependence:

$$I_{\frac{1}{2}\to\frac{1}{2}} = \delta_{\eta'-\eta''}[J']^2[J'']^2|\langle\lambda'|\mu_0^{(1)}|\lambda'\rangle|^2\left|\sum_{\omega'} C_{P'\omega'}^{J'\eta'\tau'} C_{\theta''\omega''}^{J''\eta''\tau''}\right.$$
$$\left.\times\left\{\delta_{\omega'\omega''}d_{00}^{(1)}(\theta)\begin{pmatrix} J' & 1 & J'' \\ \frac{1}{2} & 0 & -\frac{1}{2}\end{pmatrix} + \delta_{\omega'-\omega''}\eta''(-)^{J''-\sigma'}d_{10}^{(1)}(\theta)\begin{pmatrix} J' & 1 & J'' \\ \frac{1}{2} & -1 & \frac{1}{2}\end{pmatrix}\right\}\right|^2. \tag{86}$$

For a T-shaped complex, the first term vanishes resulting in a purely perpendicular type transition. While the rigid rotor analysis in combination with the above linestrength was sufficient to analyse the rotational structure of the origin band of the first overtone transition in NO–Ar, the treatment completely failed for the transition to the first excited bending level [65].

If the expansion for each eigenstate is dominated by one coefficient corresponding to a particular value of ω, we find an expression for the approximate linestrength which is identical to the one derived within the bf(2) formalism (see equation (81)):

$$I_{\frac{1}{2}\to\frac{3}{2}} = \delta_{\eta'-\eta''}[J']^2[J'']^2|\langle\lambda'|\mu_0^{(1)}|\lambda'\rangle|^2\left|d_{10}^{(1)}(\theta)\begin{pmatrix} J' & 1 & J'' \\ \frac{3}{2} & -1 & -\frac{1}{2}\end{pmatrix}\right|^2 \tag{87}$$

and

$$I_{\frac{1}{2}\to\frac{1}{2}} = \delta_{\eta'-\eta''}[J']^2[J'']^2|\langle\lambda'|\mu_0^{(1)}|\lambda'\rangle|^2\left|\delta_{\omega'\omega''}d_{00}^{(1)}(\theta)\begin{pmatrix} J' & 1 & J'' \\ \frac{1}{2} & 0 & -\frac{1}{2}\end{pmatrix}\right.$$
$$\left.+\delta_{\omega'-\omega''}\eta''(-)^{J''-\sigma'}d_{10}^{(1)}(\theta)\begin{pmatrix} J' & 1 & J'' \\ \frac{1}{2} & -1 & \frac{1}{2}\end{pmatrix}\right|^2. \tag{88}$$

Since we assume ω to be a good quantum number, only one term will contribute in the last equation rendering the phase factor irrelevant.

The selection rules giving rise to the rotational structure are illustrated in figure 13. According to equation (69), the rotational levels are split into two ω-components each of which is split into two P-type doublets. Note the change in the ordering of the P-type pairs for the $\omega = \pm\frac{1}{2}$ levels. Allowed one-photon transitions require a change in the parity between the two states (see equation (75)). Therefore, Q-branch lines can only occur between levels which differ in the symmetry quantum number ζ. Lines of the different R-branches and P-branches exist only if the symmetry quantum number is conserved. Because of the ω-splitting, four different types of branches are possible the lines of which are conveniently labelled $\Delta J^{\mathrm{sign}(\omega')}_{\mathrm{sign}(\omega'')}$. Therefore, a Q_+^--line represents a transition between levels $\omega'' = +\frac{1}{2}$ and $\omega' = -\frac{1}{2}$ with $\Delta J = 0$. The inspection of figure 13 reveals that the spacing of the branches Q_+^+ and Q_+^- is determined by the ω-splitting in the excited state. Similarly, the spacing of the two Q_+^+ branches involving different parity levels, reflects directly the P-type doubling of that level. Furthermore, the splitting of the R_+^--lines is very sensitive to the J-dependence of the P-type doubling.

These features are illustrated in figure 14 which shows the first band of the complex NO–Ar in the region of the NO overtone. It is a parallel band ($\Delta P = 0$) with $P = \frac{1}{2}$. In the top part of the figure, we have labelled the rotational lines of the different rotational branches with $(J - \frac{1}{2})$ where J is the quantum number for the

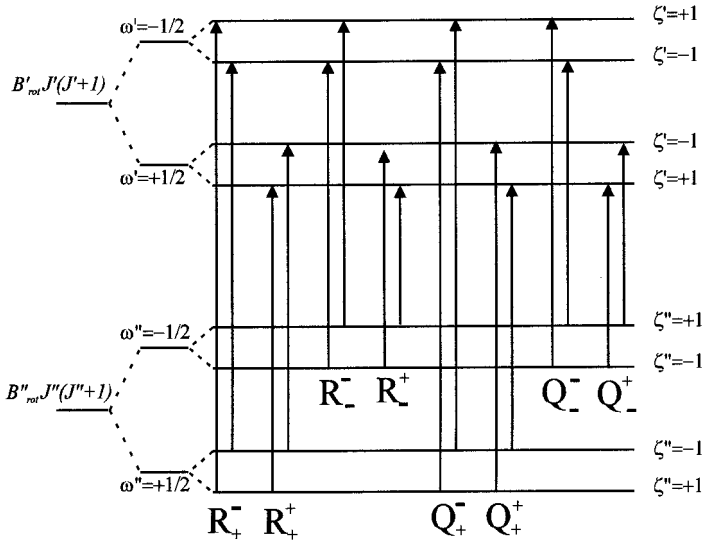

Figure 13. Possible one-photon transitions between different rotational levels of the NO–X complexes. Each level is labelled with the symmetry quantum number ζ.

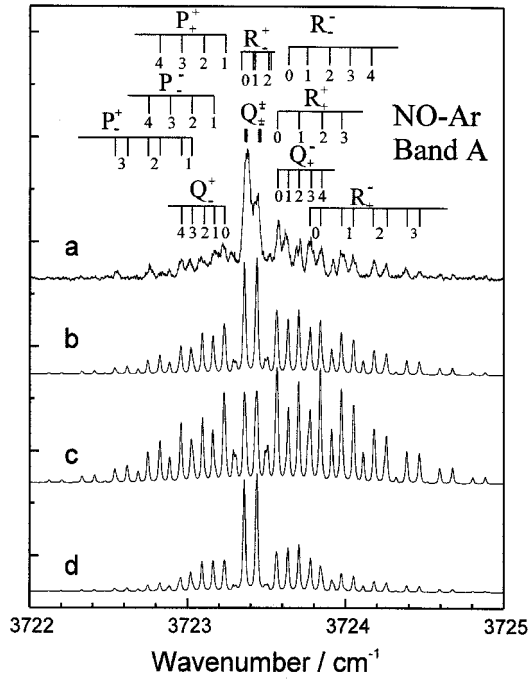

Figure 14. Comparison of band A with simulated spectra assuming different types of transition moments. See text for details.

total angular momentum. Clearly, the spectrum is dominated by two Q-branches split due to *P*-type doubling. Also the lines of the R_+^- branch are split into two parity components. in this case, we find the splitting to be independent of *J*. In general, branches starting in the upper ω-component are weaker in intensity due to the low

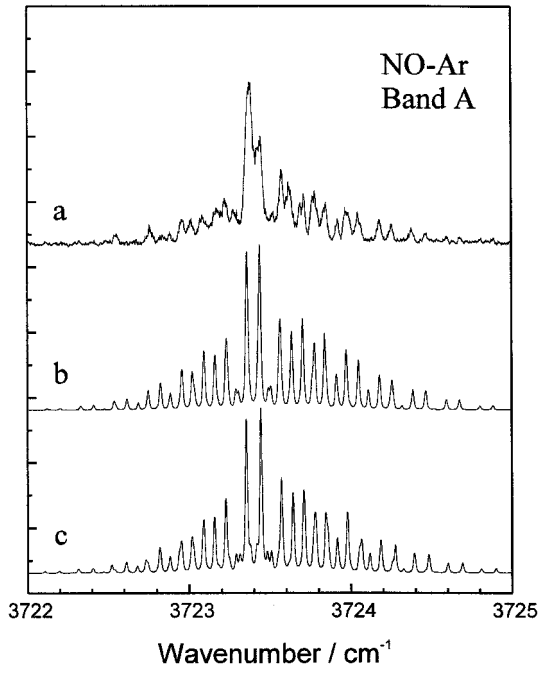

Figure 15. Comparison of band A with simulated spectra based on the results of (*c*) the *ab-initio* treatment and (*b*) the results of a fit.

beam temperature of about 1 K. In this figure, spectrum (*a*) represents the experimental data while spectrum (*b*) is calculated assuming an equal mixture of parallel and perpendicular transition moments. Spectra for pure transitions are shown as traces (*c*) (parallel) and (*d*) (perpendicular). In order to achieve better agreement with the experimental spectrum, we include all transitions with $\Delta\omega = 0, \pm 1$, thus implicitly assuming that ω is only approximately a good quantum number. The strong Q-branches that dominate the spectrum result from the perpendicular transition moment. Satisfactory agreement with the observed spectrum is found for an equal mixture of parallel and perpendicular character.

In Figures 15–17, we compare the experimental spectra (trace *a*) with calculated spectra based on a fit (trace *b*) to these spectra and a fit (trace *c*) to the *ab-initio* energy level of [35]. The resulting parameters are compiled in tables 1 and 2. The vibrational frequencies are determined by aligning the $Q_{\pm}^{\pm}$-branches with the corresponding feature for the experimental spectrum. The results for band A indicate that the predictions of the *ab-initio* calculation are in almost perfect agreement with the experimental data. A careful inspection reveals a slightly too large *P*-type doubling constant for the *ab-initio* treatment. No *P*-type doubling in the excited state is observed for the perpendicular band B as expected from the perturbation treatment in section 4.1. In this case, only a perpendicular component for the transformed transition moment is possible (see equation (77) or (87)). The associated vibrational energy predicted by the *ab-initio* calculation agrees within $0.1\,\mathrm{cm}^{-1}$ with the experimental value. The excited level represents the lowest bending level with $P = \frac{3}{2}$. Its energy is approximately given by the *a*-axis rotation of the complex: $b_{\mathrm{NO}}\hat{P}^2$. The fit to the experimental spectrum indicates slightly smaller values for the

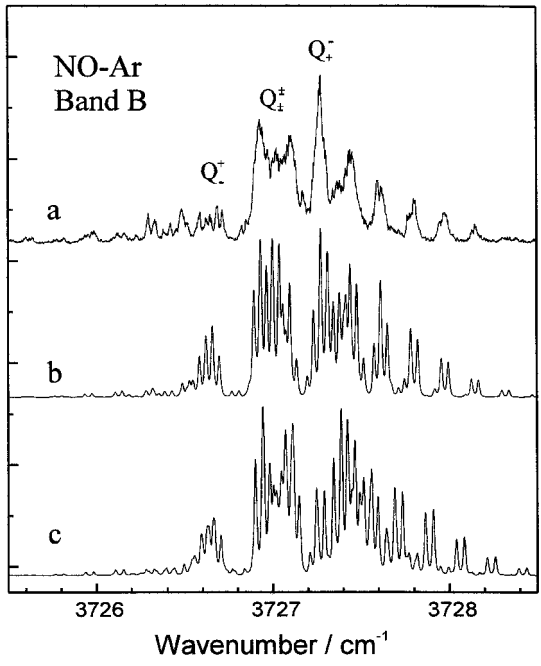

Figure 16. Comparison of band B with calculated spectra based on (*c*) the results of the *ab-initio* treatment and (*b*) the fit of the experimental spectrum.

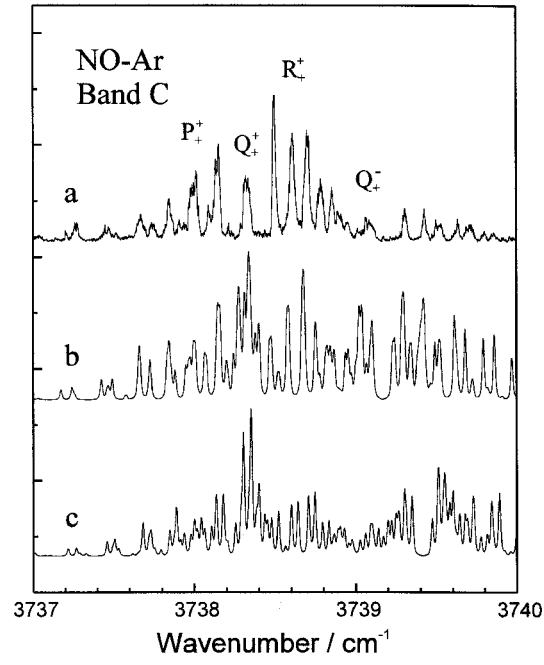

Figure 17. Comparison of band C with calculated spectra based on (*c*) the results of the *ab-initio* treatment and (*b*) the fit of the experimental spectrum.

Table 2. Constants (in cm^{-1}) for the effective Hamiltonian for the electronic ground state levels of the NO–Ar complex correlating with NO $X^2\Pi(v = 0)$. The constants are determined in a fit of the experimental spectra.

Band	$E_{P v_b v_s}$	B	V_0	$V_1/10^{-2}$	$V_2/10^{-2}$	$C_0/10^{-2}$
A	0	0.068	0.045	3.6	0.00	2.0
B	3.580	0.068	0.19	0.0	0.00	0.0
C	15.302	0.063	0.43	2.6	0.00	1.2

rotational constant and the ω-splitting. Since the rotational constant reflects the vibrationally averaged structure of the complex, a decrease in the rotational constant can result from changes towards a more T-shaped configuration or from the lengthening of the intermolecular bond distance. The former effect is also consistent with the smaller value found for the ω-splitting constant. For the parallel band C, again better agreement in the intensity distribution is found if an equal mixture of parallel and perpendicular components for the transformed transition moment is assumed. The band position is predicted by the *ab-initio* calculation within 1.1 cm^{-1}. From the position of the different Q-branches, in particular branches Q_+^+ and Q_+^-, we deduce that the predicted ω-splitting is too large while the predicted *P*-type doubling is underestimated. The major discrepancies can thus be related to the average potential. Nevertheless, the overall agreement between the two types of spectra is excellent confirming the high quality of the latest *ab-initio* set of potential surfaces determined for NO–Ar.

Similar results have been obtained also for the NO–Ne complex [36, 103]. While the spectra predicted by the complete *ab-initio* treatment reproduce the overall structure of the different observed bands extremely well, several finer details suggest again deficiencies of the original potential surfaces. In particular, the spacing between the different Q-branches is predicted to be too large due to an overestimation of the ω-splitting. Similarly, the comparison of the positions of R-branch lines suggests that the rotational constant is predicted too small. These deviations point towards small deficiencies of the average potential. On the other hand, the splitting of the R-branch lines indicates that the potential underestimates this splitting pointing towards some problem with the difference potential.

The results presented in this section demonstrate how the experimental spectra can be analysed in great detail employing an empirical Hamiltonian in combination with an approximate linestrength calculation. Such a treatment is also of great advantage for the comparison of results from a full *ab-initio* treatment with the experimental spectra. Obviously, a similar approach can be of great value for those open shell complexes for which no set of potential surfaces is available. In particular, spectra for complexes of NO with small molecules can be analysed in this way [104].

5. Rydberg state spectroscopy: NO*–X (X=Ne, Ar, Kr, Xe)

The large number of low lying Rydberg states of the NO monomer provides an ideal opportunity to study intermolecular interactions in electronically excited states. The fact that these states are well described by a single unpaired Rydberg electron outside of a closed shell ionic core (NO^+ : $X\ ^1\Sigma^+$), should facilitate the qualitative understanding of the relevant interactions. Owing to the variation in size of the various Rydberg orbitals, we expect different types of interactions to dominate. Two

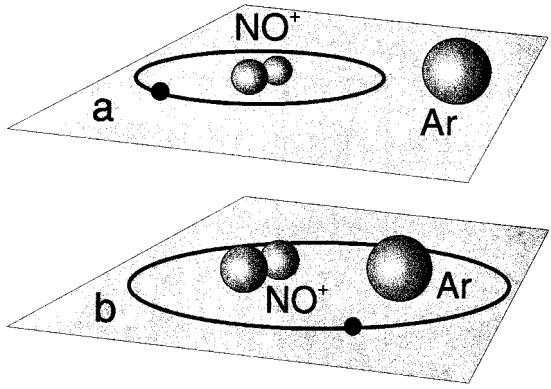

Figure 18. Schematic of the electron distribution in the NO–X complex for the situation that the corresponding Rydberg orbital is (*a*) smaller or (*b*) larger than the van der Waals radius of the rare gas atom.

extreme situations can be distinguished which are shown schematically in figure 18. If the Rydberg electron resides in an orbital which is smaller than the average van der Waals radius, mainly weak dispersion forces will be responsible for the interaction. In contrast, if the radius of the Rydberg orbital exceeds the van der Waals radius, we expect the interaction to be dominated by strong attractive induction forces due to the ionic core. For the latter case, we predict the complex to resemble the corresponding cationic complex. The size of the Rydberg orbital increases roughly as the square of the effective principal quantum number n^* which is determined from the position of the term T_n relative to the ionization limit I_p [95]

$$n^* = \left(\frac{R_\infty}{I_p - T_n}\right)^{1/2} \tag{89}$$

where R_∞ is the Rydberg constant.

The expectation value for the size in atomic units of the Rydberg orbital can be approximated by the corresponding value for the H-atom replacing the principal quantum number n with its effective value n^*:

$$\langle r_{nl} \rangle = \tfrac{1}{2}(3n^{*2} - l(l+1)). \tag{90}$$

Values for the related quantum defect $\delta = n - n^*$ and the radius r_{nl} for the low lying Rydberg states of NO are listed in tables 5 and 6. For a typical van der Waals radius, we can thus expect a transition from dispersion dominated bonding to ion-induced interactions within a particular Rydberg series. An estimate of the typical radius suggests that this transition occurs already for small values of n^*. Therefore, the low lying Rydberg states of NO are of particular interest in studying this transition. As a first approximation, we expect the variation in the bonding of the complex to be determined to a large extent by the electronic structure of the Rydberg state in the NO monomer. This approximation implies further that excited states of the complex can be identified with the corresponding monomer states. In the following, we will denote the excited states of the complex with the term label of the monomer to which a tilde is added. On the other hand, electronic state interactions have been identified already for the monomer. Thus the spectroscopic investigation of the excited states

of the complexes can provide insights into the way in which perturbations are affected by the complexed atom.

5.1. *NO monomer spectroscopy*

For the study of the Rydberg states of complexes of NO with various rare gas partners, we can approximate the character of the transition in the complex with the character of the corresponding monomer transition. Thus it is important to have a good understanding of the one-photon and two-photon spectroscopy involving different excited states of the NO monomer. One-photon absorption and emission spectra of the monomer have been studied extensively throughout the electromagnetic spectrum [105]. The ground state electron configuration of NO, $(1s\sigma)^2(1s\sigma^*)^2(2s\sigma)^2(2s\sigma^*)^2(2p\sigma)^2(2p\pi)^4(2p\pi^*)^1(2p\sigma^*)^0$, gives rise to the $X\,^2\Pi$ ground state. Rydberg states are generated by promoting the electron from the antibonding orbital π^* to a Rydberg orbital approximately characterized by atomic quantum numbers n and l. Several Rydberg series with different values of l converge to the Σ^+-ground state of the cation NO^+ located at about 9.6 eV. Since the first excited state of the ion lies at much higher energy, Rydberg series converging towards the ionic ground state exhibit little mixing with the series converging towards excited states of the cation.

The different Rydberg states are described well by the $^1\Sigma$- core of NO^+ and a singly occupied Rydberg orbital resulting in relatively simple spectra. According to the value of l, the atomic orbitals split into molecular orbitals characterized by the projection of the orbital angular momentum on to the diatom axis. Since the associated energies are very similar, it is customary to refer to the resulting states as the states derived form an *nl*-complex. For example, the 3p-orbital splits into a non-degenerate 3pσ-orbital and a doubly degenerate 3pπ-orbital giving rise to the states $D\,^2\Sigma$ and $C\,^2\Pi$ respectively. The present review is mainly concerned with the lowest Rydberg states that are derived from the complexes $3s(A\,^2\Sigma)$, $3p(D\,^2\Sigma, C\,^2\Pi)$, $3d(H'\,^2\Sigma, H\,^2\Pi, F\,^2\Delta)$ and $4s(E\,^2\Sigma)$. Their energy ordering is indicated schematically in figure 19. The exact energies of the derived states are influenced critically by various interactions. The large quantum defect of the $(n+1)$s-orbitals is responsible for a near-degeneracy with the *n*d-orbitals. For example, within the 3d complex, the mixing of the Π component with state $E\,^2\Sigma$, in combination with core penetration effects is responsible for the irregular ordering of the states derived from the 3d complex [106]. In addition, the Σ and Π components of the latter are strongly mixed due to *l*-uncoupling interaction. Since to a first approximation the Rydberg electron does not interact with the ionic core, the vibrational frequency and the rotational constants for the Rydberg states resemble the ones for the cation ($\nu_{NO^+} = 2376\,cm^{-1}$, $b_{NO^+} = 2.06\,cm^{-1}$) [107]. In contrast, valence states involve electron configurations in which a valence electron is promoted within the ground state configuration from a bonding to an unfilled antibonding orbital resulting in significantly reduced vibrational frequencies and rotational constants. Additional important homogeneous interactions have been identified between the Rydberg states $C\,^2\Pi$, $F\,^2\Delta$ and the valence states $B\,^2\Pi$, $B'\,^2\Delta$. The degree of interaction changes with vibrational level. For example, the vibrational levels ($C\,^2\Pi(v'=2)$, $B\,^2\Pi(v'=12)$) and ($C\,^2\Pi(v'=3)$, $B\,^2\Pi(v'=14)$) form strongly mixed pairs. The degree of state mixing depends critically on the rotational energy which tunes the overall energy in and out of resonance [108].

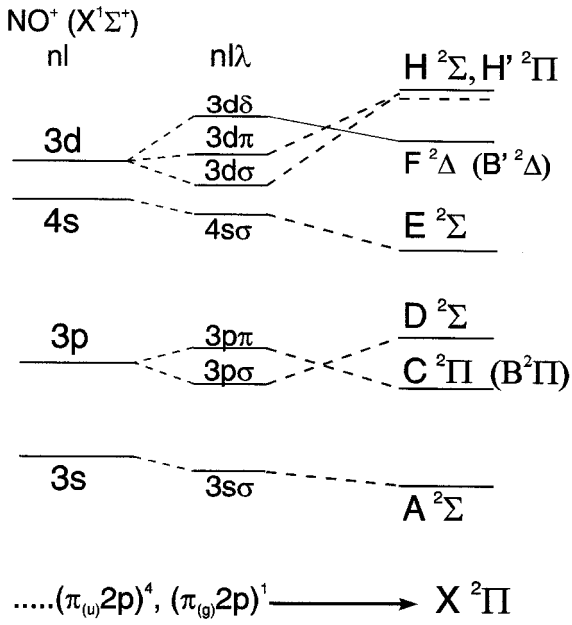

Figure 19. Energy ordering of the low lying Rydberg states of NO.

Most of the original spectroscopic work on NO was based on the analysis of the rotational structure of one-photon transitions between the different states discussed above. Higher Rydberg states have been investigated more recently using different multiphoton techniques, in particular multiphoton ionization spectroscopy [109, 110]. The rotational structure of a two-photon transition can be described in terms of the matrix elements of the two-photon absorption operator. The components of the latter are conveniently rearranged to form spherical tensor operators with well-known transformation properties. For excitation with linearly polarized light, only tensors of ranks 0 and 2 contribute to the linestrength. Furthermore, the kth component of the second rank tensor gives rise to transitions between electronic states with $\Delta\lambda = \pm k$ where λ represents the quantum number for the projection of the electronic orbital angular momentum onto the axis of the diatom.

5.2. *Two-photon linestrength*

In this section, we review briefly the two-photon spectroscopy of triatomic complexes containing an open shell diatom appropriate for the rigid rotor treatment described in section 3.3. For simplicity we restrict the discussion to excitation of an isotropic molecular ensemble with linearly polarized light. Within the framework of second-order time-dependent perturbation theory, it can be shown that the intensity for a non-resonant two-photon transition between levels i and f is given as follows:

$$I_{i\to f} = C \sum_{M',M''} |\tilde{S}_{if}|^2 \quad \text{with}$$

$$\tilde{S}_{if} = \left\langle f \left| \sum_{ab} \hat{e}^*_{1a}\hat{e}^*_{2b}T_{ab} \right| i \right\rangle \quad \text{and} \quad T_{ab} = \sum_k \left\{ \frac{\mu_a|k\rangle\langle k|\mu_b}{\omega_{ki} - \omega_2} + \frac{\mu_b|k\rangle\langle k|\mu_a}{\omega_{ki} - \omega_1} \right\}. \qquad (91)$$

Here we have expressed the transition matrix element in terms of the cartesian components of the two-photon absorption operator T_{ab} and the components of the polarization vectors $\mathbf{e}_1$ and $\mathbf{e}_2$ of the two involved laser fields. Their product defines the cartesian polarization tensor P_{ab}. In order to facilitate the transformation between different coordinate frames, we express the tensor product in equation (91) in terms of the product between the components of the spherical tensor operators $P_m^{(j)}$ and $T_m^{(j)}(\mathrm{sf})$. Assuming an isotropic molecular ensemble, we define the space-fixed z-axis along the direction of the linear laser polarization. The resulting polarization tensor $P_m^{(j)}$ has only non-vanishing components for $m = 0$, and $j = 0$ or $j = 2$. Consequently, only zeroth or second rank tensor components with $m = 0$ can contribute to the two-photon linestrength. Expressing the tensor components in terms of spherical tensors, we find

$$S_{if} = \left\langle f \left| \sum_j P_0^{(j)} T_0^{(j)}(\mathrm{sf}) \right| i \right\rangle \quad \text{and} \quad P_0^{(0)} = -\frac{1}{3^{1/2}}, \quad P_0^{(2)} = +\left(\frac{2}{3}\right)^{1/2}. \tag{92}$$

Since we assume that the diatom acts as a two-photon chromophore in the complex and that its electronic structure does not change significantly upon complexation, the two-photon transition in the complex will be carried by the same tensor components of the transition moment operator as the corresponding transition in the monomer. Therefore, we express the sf tensor components in terms of the corresponding components $T_{\tilde{k}}^{(j)}(\mathrm{mf})$ of the diatom defined in the bf(3) frame. In analogy with equations (72) and (82), we find

$$T_0^{(j)}(\mathrm{sf}) = \sum_k T_k^{(j)}(\mathrm{bf}) D_{0k}^{(j)^*}(\hat{\boldsymbol{R}}) = \sum_{k\tilde{k}} T_{\tilde{k}}^{(j)}(\mathrm{mf}) D_{k\tilde{k}}^{(j)^*}(\hat{\boldsymbol{r}}) D_{0k}^{(j)^*}(\hat{\boldsymbol{R}})$$

$$\text{with} \quad \hat{\boldsymbol{R}} = (\alpha, \beta, \gamma) \quad \text{and} \quad \hat{\boldsymbol{r}} = (0, \theta, 0). \tag{93}$$

Once the two-photon absorption characteristics (i.e. the non-vanishing tensor components of the associated monomer transition) are known, we can calculate an approximate cluster spectrum using the eigenfunctions of the rigid rotor model Hamiltonian defined in equation (65)

$$\tilde{S}_{if} = \sum_{jk\tilde{k}} \sum_{P'\omega' P''\omega''} C_{P'\omega'}^{J'\eta'\tau'} C_{P''\omega''}^{J''\eta''\tau''} P_0^{(j)} d_{k\tilde{k}}^{(j)}(\theta) \langle J'M'P'\omega'\eta' | T_{\tilde{k}}^{(j)}(\mathrm{mf}) D_{0k}^{(j)^*} | J''M''P''\omega''\eta'' \rangle. \tag{94}$$

In evaluating the matrix elements, we make use of the properties of the 3j-symbols, $\begin{pmatrix} \cdots \\ \cdots \end{pmatrix}$, representing the integrals over the Euler angles and of the selection rules for the electronic transition matrix elements, i.e. $\tilde{k} = \lambda' - \lambda''$ and $\tilde{k} = -(\lambda'' + \lambda')$:

$$\begin{aligned}
&\sum_{k\tilde{k}} d_{k\tilde{k}}^{(j)}(\theta) \langle J'M'P'\omega'\eta' | T_{\tilde{k}}^{(j)}(\mathrm{mf}) D_{0k}^{(j)^*}(\alpha, \beta, \gamma) | J''M''P''\omega''\eta'' \rangle \\
&= \frac{[J'][J'']}{2} (-)^{M-P'} \begin{pmatrix} J' & j & J'' \\ M & 0 & -M \end{pmatrix} (1 + \eta'\eta'') \sum_{k\tilde{k}} \left\{ \delta_{\sigma'\sigma''} \langle \lambda' | T_{\tilde{k}}^{(j)} | \lambda'' \rangle \begin{pmatrix} J' & j & J'' \\ P' & -k & -P'' \end{pmatrix} \right. \\
&\quad \left. \times d_{k\tilde{k}}^{(j)}(\theta) + \delta_{\sigma'-\sigma''} \eta' (-)^{J''+\lambda'+s-\sigma'-P'} \langle -\lambda' | T_{\tilde{k}}^{(j)} | \lambda'' \rangle \begin{pmatrix} J' & j & J'' \\ P' & k & P'' \end{pmatrix} d_{k\tilde{k}}^{(j)}(\theta) \right\}.
\end{aligned} \tag{95}$$

As expected, the parity of the two involved states must be preserved in a two-photon process. The intensity is found by taking the absolute value squared of S_{if} and summing over all basis states in equation (94). Summation over the magnetic quantum numbers yields the factor $(2j+1)^{-1}\delta_{jj'}$. The Kronecker delta ensures that no cross terms involving components of tensors of different rank contribute to the spectrum. In the presence of a zeroth and a second rank tensor, it must be regarded as the superposition of two independent spectra

$$I_{i\to f} = C[J']^2[J'']^2\delta_{\eta'\eta''}\sum_j \frac{P_0^{(j)^2}}{2j+1}\left|\sum_{P'\omega'P''\omega''} C^{J'\eta'\tau'}_{P'\omega'} C^{J''\eta''\tau''}_{P''\omega''}(-)^{-P'}\right.$$
$$\times\sum_{k\tilde{k}}\left\{\delta_{\sigma'\sigma''}\langle\lambda'|T^{(j)}_{\tilde{k}}|\lambda''\rangle d^{(j)}_{k\tilde{k}}(\theta)\begin{pmatrix} J' & j & J'' \\ P' & -k & -P''\end{pmatrix}\right.$$
$$\left.\left.+\delta_{\sigma'-\sigma''}\eta'(-)^{J''+\lambda'+s-\sigma'-P'}\langle-\lambda'|T^{(j)}_{\tilde{k}}|\lambda''\rangle\begin{pmatrix} J' & j & J'' \\ P' & k & P''\end{pmatrix} d^{(j)}_{k\tilde{k}}(\theta))\right\}\right|^2. \quad (96)$$

The spectrum due to the zeroth rank component consists of Q-branches only. Furthermore, it exists only for transitions between electronic states with the same component λ and the same total angular momentum projection

$$I_{i\to f} = C\frac{1}{3}[J']^2\delta_{\eta'\eta''}\left|\sum_{P'\omega'P''\omega''} C^{J'\eta'\tau'}_{P'\omega'} C^{J''\eta''\tau''}_{P''\omega''}\left\{\delta_{\sigma'\sigma''}\delta_{P'P''}\delta_{J'J''}\delta_{\lambda'\lambda''}\langle\lambda'|T^{(0)}_0|\lambda'\rangle\right.\right.$$
$$\left.\left.+\delta_{\sigma'-\sigma''}\eta'(-)^{J''+\lambda'+s-\sigma'-P'}\delta_{P'-P''}\delta_{J'J''}\delta_{\lambda'-\lambda''}\langle-\lambda'|T^{(0)}_0|\lambda''\rangle\right\}\right|^2$$
$$+C\frac{2}{15}[J']^2[J'']^2\delta_{\eta'\eta''}\left|\sum_{P'\omega'P''\omega''} C^{J'\eta'\tau'}_{P'\omega'} C^{J''\eta''\tau''}_{p''\omega''}(-)^{-P'}\right.$$
$$\times\sum_{k\tilde{k}}\left\{\delta_{\sigma'\sigma''}\begin{pmatrix} J' & 2 & J'' \\ P' & -k & -P''\end{pmatrix}\langle\lambda'|T^{(2)}_{\tilde{k}}|\lambda''\rangle d^{(2)}_{k\tilde{k}}(\theta)\right.$$
$$\left.\left.+\delta_{\sigma'-\sigma''}\eta'(-)^{J''+\lambda'+s-\sigma'-P'}\langle-\lambda'|T^{(2)}_{\tilde{k}}|\lambda''\rangle\begin{pmatrix} J' & 2 & J'' \\ P' & k & P''\end{pmatrix} d^{(2)}_{k\tilde{k}}(\theta)\right\}\right|^2. \quad (97)$$

5.2.1. *Two-photon absorption: axis-switching*

In considering different electronic transitions, it is important to consider the possibility that the principal axis system for the excited state differs from the one in the electronic ground state. In order to evaluate the transition matrix elements, all wavefunctions are referred to the principal axis system of the electronic ground state. A change in the averaged structure of the excited state implies that the associated PA' system is rotated by an angle τ with respect to the PA'' system. Therefore, it is necessary to represent the basis functions of the PA' systems (see equation (65)) as transformed PA'' functions. Using the transformation properties of the rotation matrix element $D^{(J')}_{MP'}(\hat{\boldsymbol{R}})$ under rotation, we find

$$D^{(J')}_{MP'}(\alpha',\beta',\gamma') = \sum_{\tilde{P}} D^{(J')^*}_{\tilde{P}P'}(0,\tau,0) D^{(J')}_{M\tilde{P}}(\hat{\boldsymbol{R}}') = \sum_{\tilde{P}} d^{(J')}_{\tilde{P}P'}(\tau) D^{(J')}_{M\tilde{P}}(\hat{\boldsymbol{R}}''). \tag{98}$$

Here the primed Euler angles $\hat{\boldsymbol{R}}' = (\alpha',\beta',\gamma')$ specify the orientation of the PA' frame with respect to the sf frame while the orientation of the PA'' frame is described by the double primed angles, i.e. $\hat{\boldsymbol{R}}'' = (\alpha'',\beta'',\gamma'')$. Since the triatomic complex is planar, the two frames are connected by a simple rotation around the y axis through an angle τ. The basis functions for the expansion of the excited state can now be written in terms of the transformed PA'' functions. Substituting equation (98) into equation (65) we find the transformed basis function

$$|J'M'P'\omega'\eta'\rangle = \frac{1}{\sqrt{2}} \sum_{\tilde{P}} \Big\{ d^{(J')}_{\tilde{P}P'}(\tau) |J'M\tilde{P}\rangle |n\lambda'\rangle |s\sigma'\rangle + \eta'(-)^{J'-P'+\lambda'+s-\sigma'} d^{(J')}_{-\tilde{P}-P'}(\tau) |J'M-\tilde{P}\rangle |n-\lambda'\rangle |s-\sigma'\rangle \Big\}. \tag{99}$$

The analogue of equation (96) takes on the form

$$I_{i\to f} = C[J']^2[J'']^2 \delta_{\eta'\eta''} \sum_j \frac{P_0^{(j)^2}}{2j+1} \Bigg| \sum_{P'\omega'P''\omega''} C^{J'\eta'\tau'}_{P'\omega'} C^{J''\eta''\tau''}_{P''\omega''} \sum_{k\tilde{k}\tilde{P}} (-)^{-\tilde{P}} d^{(j)}_{k\tilde{k}}(P) d^{(J')}_{\tilde{P}P'}(\tau) \times \Bigg\{ \delta_{\sigma'\sigma''} \langle \lambda' | T^{(j)}_{\tilde{k}} | \lambda'' \rangle \begin{pmatrix} J' & j & J'' \\ \tilde{P} & -k & -P'' \end{pmatrix} - \delta_{\sigma'-\sigma''} \eta' (-)^{J'+\lambda'+s-\sigma'-\tilde{P}} \langle -\lambda' | T^{(j)}_{\tilde{k}} | \lambda'' \rangle \times \begin{pmatrix} J' & j & J'' \\ -\tilde{P} & -k & -P'' \end{pmatrix} \Bigg\} \Bigg|^2. \tag{100}$$

The properties of the d-functions (see, for example [102]) ensure that, for $\tau = 0$, the sum over $\tilde{P}$ has contributions for only $\tilde{P} = P'$ and that the expression for the intensity reduces to that given in equation (96).

5.3. *The 3s complex (NO–X, X=Ar, Kr, Xe): $\tilde{A}\,^2\Sigma$*

The $A\,^2\Sigma$-state is the first member of the *n*s Rydberg series of the NO monomer. It is relatively weak in comparison with transitions to the members of the 3p complex. Nevertheless, the corresponding transition in several NO–X complexes has attracted much interest over recent years. Indeed the first spectroscopic detection of the NO–Ar complex was achieved using LIF [57]. In this study, only transitions to the $\tilde{A}$-state continuum were observed. More recently also bound–bound transitions have been detected using LIF or REMPI [58–61, 111, 112]. Although complexes with Xe and Kr have been detected using (1 + 1) REMPI [62], the analysis of the rovibrational structure has so far concentrated on the observed NO–Ar spectrum. For the state $\tilde{A}\,^2\Sigma$ of the latter complex, the origin is assigned to a feature located at 44 242 cm^{-1} blue shifted by about 43 cm^{-1} from the corresponding monomer origin. This close proximity in frequency to the much larger NO monomer rotational lines causes serious experimental difficulties which have been overcome only recently.

In combination with the ground state binding energy, Obi and co-workers derived a dissociation energy of about 44 cm^{-1} suggesting only a weak interaction with the cationic core [59]. This behaviour is not surprising since the A-state has a large quantum defect resulting in an expectation value for the radius of the Rydberg

orbital smaller than the van de Waals radius. In other words, the Rydberg electron resides in an orbital which allows it to screen effectively the charge of the NO^+ core.

Because of the very weak bond, one cannot expect the rigid rotor model of section 3.3 to be adequate in describing the rovibrational structure for this system. In particular, the large amplitude bending motion will be coupled strongly to the rotational motion of the complex. Sausa and co-workers applied a hindered rotor formalism to assign several features in the spectrum to the excitation of different bending levels [60]. The model Hamiltonian was originally used by Hutson to describe the correlation of the bending levels in a transition from a linear configuration through a freely rotating diatom to a strongly bound T-shaped complex [86]. The model is easily derived from the bender Hamiltonian introduced in section 3.2 (see equation (26)) by averaging the latter over the stretch coordinates. As a result of their analysis, Sausa and co-workers concluded that the effective bending Hamiltonian is dominated by a V_2-term while the V_1-term is very small. Unfortunately, the data were not sufficient to distinguish between a global minimum for the linear or the T-shaped configuration. In their recent investigation, Lozeille *et al.* employ the same hindered rotor model [111]. According to this analysis, the observed spectrum is a composite of at least two band systems: excitation to the vibrationless origin band and to the first intermolecular stretch level. Additional bands are assigned to excitation of combination bands involving different bending levels. For the vibrational ground state of the $\tilde{A}$-state, a negative V_2-term results in a linear configuration. In the first excited stretch level, the anisotropy is dominated by a positive V_2-term moving the global minimum of the $\tilde{A}$-state surface to the T-shaped configuration. In the latter case, the rotation of the NO moiety causes partially resolved rotational structure. As the authors point out, the concept of an effective rigid rotor structure is not appropriate and the rotational structure should be regarded as almost free rotation of the NO within the molecular plane (representing the bending vibration) or out of the molecular plane representing the *a* axis rotation.

5.4. *The 3p complex (NO–X, X=Ne, Ar, Kr, Xe): $\tilde{C}\,^2\Pi, \tilde{D}\,^2\Sigma$*

In the NO monomer, the 3p complex gives rise to the close lying Rydberg states, $C\,^2\Pi$ and $D\,^2\Sigma$ which are responsible for the NO δ– and ε-bands, respectively. Most of the experimental work for the complexes has concentrated on spectra involving the $C\,^2\Pi$-state. Nevertheless, weak band systems in the region of the ε-bands of the monomer are observed for the NO–Ar complex and assigned to the levels $\tilde{D}\,^2\Sigma(v' = 0, 1)$ [67, 69]. To date no corresponding data have been reported for other complexes.

Band systems correlating with the lowest vibrational levels of the NO $C\,^2\Pi$-state have been detected through $(2 + 1)$ REMPI for complexes with Ne [67, 70], Ar [17, 61, 66, 67, 69, 113], Kr [67, 68, 113], and Xe [67, 68, 113]. While, for complexes with Kr and Xe, only the band system involving the level $\tilde{C}^2\Pi(v' = 0)$ has been reported, band systems correlating with the NO vibrational level $v' = 0$–4 have been measured for complexes with Ne and Ar. The overall structure of all observed band systems is very similar with the exception of the spectra reported for NO–Xe. In this case the REMPI signal for NO–Xe appears in the Xe^+-channel. Up to date, this onset of charge transfer in the excited or ionic complex has prevented the unambiguous assignment of the intermolecular vibrations of this complex.

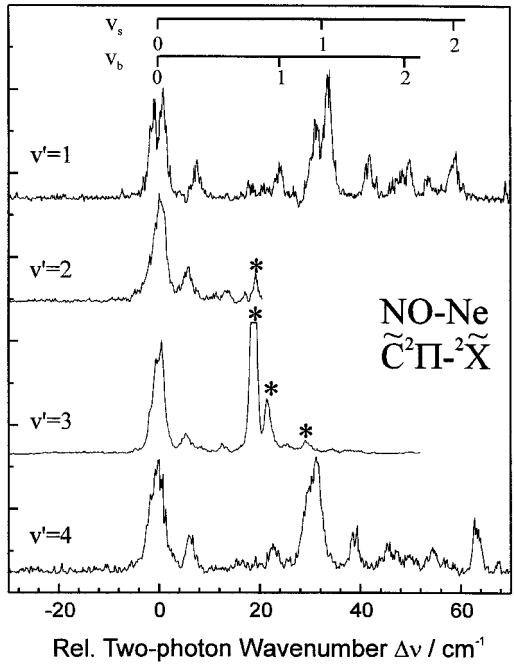

Figure 20. Spectra of the $\tilde{X} - \tilde{C}\,^2\Pi(v' = 1\text{-}4)$ transition in NO–Ne. Features marked with an asterisk are artefacts resulting from baseline shifts due to strong monomer transitions.

For the other complexes, a complete vibrational analysis was achieved only after understanding the rotational structure of the two-photon transition in these complexes [17, 70, 113]. As will be discussed below, the understanding of the rotational structure of the two-photon transitions is a prerequisite to the successful vibrational analysis of the spectra. This is especially important when the rotational energies are comparable to intermolecular vibrational energies. In the case of the NO($C\,^2\Pi$)–X complexes, the vibrational assignments are consistent with a dominant progression in the intermolecular stretch vibration and a nonlinear (almost T-shaped) vibrationally averaged structure. The dominance of the stretch progression is consistent with a significant reduction in the NO–X bond distance. Furthermore, we identified the blue satellites that accompany the members of the stretch progression as partially resolved rotational structures rather than hotbands or excitation to different bending levels. Additional weak bands are assigned to members of a progression in the bending vibration. The weak intensity of the members of this progression gives additional evidence for the near T-shaped configuration which implies unfavourable Franck–Condon factors for transitions with $\Delta v_b \neq 0$. Typical spectra for the excitation of different NO vibrational levels are shown in figure 20 and 21 where we have aligned the origins of the individual band systems for clarity.

The rotational structure of these spectra can be understood when we assume that the two-photon absorption process is confined to the NO unit of the complex. Since the C–X two-photon transition in the monomer is carried by two different tensor components, $T_0^{(0)}(\mathrm{mf})$ and $T_0^{(2)}(\mathrm{mf})$, the corresponding spectrum of the complex is a

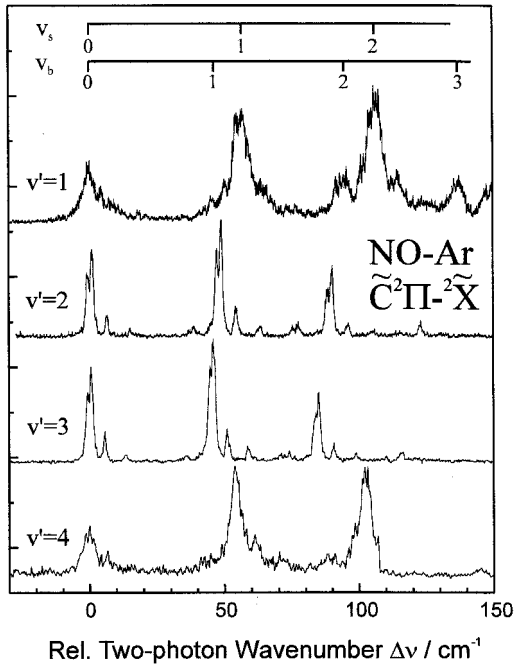

Figure 21. Spectra of the $\tilde{X} - \tilde{C}\,^2\Pi(v' = 1\text{-}4)$ transition in NO–Ar. Spectra recorded for $v' = 2$ and 3 show no indication of lifetime broadening due to predissociation.

superposition of two different spectra. The first spectrum consists of Q-branches only which cannot be resolved with the effective experimental resolution at the two-photon level of about $0.5\,\mathrm{cm}^{-1}$. Upon transformation to the PA system, the second rank component will be responsible for perpendicular transitions with $\Delta P = \pm 1, \pm 2$. In the case of a perfect symmetric top, we expect unresolved P-branches located at positions $(A - B)\Delta P^2$. Since only levels with $P'' = \frac{1}{2}$ are populated in the cold molecular beam environment, we find possible two-photon transitions to levels with $P' = \frac{3}{2}$ and $P' = \frac{5}{2}$. Therefore, we predict the unresolved rotational branches to be located on the blue side of the rotationless origin at frequencies $2(A - B)$ and $6(A - B)$. Since, for a near T-shaped complex, the a-inertial axis approximately coincides with the internuclear axis, the rotational constant A is given approximately by the rotational constant b_{NO} of the monomer while the constant B is very small and can be neglected in a first approximation. Using typical values for the NO monomer Rydberg states, we predict spacings of about 4 and $12\,\mathrm{cm}^{-1}$ which can be compared to the experimentally observed positions, e.g. for the band system Ar–NO $\tilde{C}\,^2\Pi(v' = 2)$: 4.8 and $13\,\mathrm{cm}^{-1}$ [17]. The slight increase in the experimentally observed value for the A constant compared to b_{NO} reflects either a deviation from the T-shaped configuration or a change in the rotational constant b_{NO} in the complex. Although the latter explanation seems to be very unlikley at first, we must have in mind that, in the monomer, the states $C\,^2\Pi(v')$ interact strongly with valence states $B\,^2\Pi(v')$. Therefore, the observed excited monomer levels must be regarded as mixtures which contain at least these two unperturbed states. The degree of mixing depends on the energy mismatch between the unperturbed states. It is thus conceivable that in the complex the energy mismatch is changed causing a reduction

in the $\tilde{B}$-state admixture. Since the latter state is characterized by a much smaller rotational constant, the effective rotational constant of NO can actually increase.

Evidence for this change in state mixing upon complexation can be deduced from a comparison of the intermolecular vibrational frequencies with the observed frequency shifts for the band origins. In table 3, we have compiled the term values and spectroscopic constants for the different band systems of NO $(\tilde{C}\,^2\Pi(v'))$-X (X = Ne, Ar). For comparison, we list in the first three columns the corresponding values for the NO monomer. The first entry refers to the position of the observed band while the second and third entries represent the term values after applying a first-order and second-order deperturbation procedure, respectively [108]. Beside the term values for the different cluster bands, we also list the frequency shift with respect to the monomer value (first-order perturbed values).

For both clusters, the frequency shifts and observed frequencies for the bands with $v' = 0, 1$, and 4 are very similar indicating that the intermolecular interaction changes very little as a function of NO vibration. In contrast, the shifts found for levels $v' = 2$ and 3, are further red shifted in the case of Ar while the corresponding bands for the Ne complex are shifted either to the blue or further to the red. This anomalous behaviour in the frequency shifts becomes also evident when either the observed monomer band positions or the positions resulting from second-order deperturbation are used. Within the Born–Oppenheimer approximation, the dissociation energy D_0' of the complex in the excited state can be derived from a cycle involving the dissociation energy D_0'' for the ground state and the observed frequency shift $\Delta\nu$: $D_0' = D_0'' - \Delta\nu$. Assuming the validity of the Born–Oppenheimer approximation, we must interpret the changes in the observed shifts in terms of changes in the binding energy. Alternatively, we can derive an estimate of the binding energy of the complexes from the observed intermolecular stretch frequencies, in particular fundamentals and overtones.

For the band systems of the NO–Ne complex correlating with the NO vibrational levels $v' = 2$ and $v' = 3$, only the first member of the stretch progression is observed experimentally due to serious baseline shifts caused by strong NO monomer lines in this region. In the case of NO $(v' = 2, 3)$-Ar, several members of the stretch progression are observed yielding frequencies which are noticeably smaller than the ones found for the other band systems (see figure 21). These reduced values of the

Table 3. Comparison of term values and spectroscopic constants (in cm^{-1}) for the vibrational bands NO$(\tilde{C}\,^2\Pi(v'))$-X (X = Ne, Ar) with the corresponding monomer values. See text for details

$\tilde{C}(v')$	NO(0)[a]	NO(1)[a]	NO(2)[a]	NO–Ne	$\Delta\nu(1)$	ν_s	NO–Ar	$\Delta\nu(1)$	ν_s
0	52 373	52 372	52 380	52 287[b]	−85	34	52 050[b]	−332	56
1	54 690	54 697	54 742	54 612[c]	−85	33	54 373[d]	−324	56
2	57 081	56 958	57 108	57 044[c]	+86	?	56 578[d]	−390	48
3	59 208	59 420	59 378	59 188[e]	−232	?	59 046[e]	−374	44
4	61 732	61 741	61 677	61 656[c]	−85	31	61 428[d]	−313	54

[a] Reference [108].
[b] Reference [67].
[c] Reference [70].
[d] Reference [17].
[e] This work.

stretch frequency indicate a decrease in the dissociation energy contradicting the values derived from the increased red shifts. Since in the NO monomer the vibrational levels $v' = 2$ and 3 of the state $C\,^2\Pi$ are most strongly mixed with levels of the state $B\,^2\Pi$, the data give strong support for the occurrence of complexation-induced changes in the homogeneous interaction between the C- and the B-states of the NO moiety within the complex.

As can be seen in figures 21 and 20, among the cluster bands correlating with different vibrational levels of the C-state, the band system correlating with NO $(C\,^2\Pi(v' = 1)) + Ar$ exhibits substantial broadening due to predissociation [17]. Although the signal level for this band is particularly weak, it is interesting to note that the bands assigned to the bending vibration are significantly enhanced in intensity indicating a weaker coupling to the dissociation coordinate. These findings have been confirmed in a recent study of Tsuji *et al.* [69]. As a possible explanation, these authors suggest predissociation via a lower lying vibrational level of the $\tilde{B}$-state as the dominant mechanism. Since most of the $\tilde{C}$-state vibrational levels are significantly mixed differences in the predissociation behaviour are attributed to the difference in Franck–Condon factors between the bound state wavefunction and the continuum state associated with the $\tilde{B}$-state. In table 4, we compare the term values for the different vibrational levels of the B-state obtained in a first-order deperturbation procedure [108]. Neglecting the dissociation energy for the $\tilde{B}$-state, the energy mismatch controlling the Franck–Condon factor is given simply by the term difference. For NO–Ar, we find indeed a minimum for the $\tilde{C}\,^2\Pi(v' = 1)$ thus indicating a fast predissociation process. Along this line of reasoning, noticeable predissociation can also be expected for $\tilde{C}\,^2\Pi(v' = 4)$ in agreement with our observation of reduced intensity and broadened rotational features (see figure 21). In the case of the NO–Ne complex, we also find a strong variation in the mismatch of the different term values. The smallest value is now found for the level $\tilde{C}\,^2\Pi(v' = 2)$ which is almost resonant with the B-state level $v' = 12$. As can be seen in figure 20, we do not observe any evidence for strong predissociation for any of the detected NO–Ne band systems. In order to rationalize the predissociation behaviour for NO–Ne, we must remember that, in the monomer, the levels $v' = 2$ and $v' = 3$ are most strongly perturbed by the B-state. Therefore, we expect the strongest effects for the state mixing in these levels upon complexation. Furthermore, the dissociation energy in the NO–Ne complex is comparable to the magnitude of the perturbation matrix

Table 4. Comparison of term values (in cm^{-1}) for the vibrational bands NO $(\tilde{C}\,^2\Pi(v'))$-X (X = Ne, Ar) with the values for the monomer state $B\,^2\Pi$. See text for details.

$B(v')$	NO(1)[a]	ΔE	NO–Ne	$\tilde{C}(v')$	NO–Ar	ΔE	$B(v')$	NO(1)[a]
6	51 425	862	52 287[b]	0	52 040[b]	615	6	51 425
9	54 203	409	54 612[c]	1	54 373[d]	170	9	54 203
12	56 878	166	57 044[c]	2	56 578[d]	584	11	55 984
14	58 564	624	59 188[e]	3	59 046[e]	482	14	58 564
17	61 103	553	61 656[c]	4	61 428[d]	325	17	61 103

[a] Reference [108].
[b] Refererence [67].
[c] Reference [70].
[d] Reference [17].
[e] This work.

elements for the B/C state interaction. It is therefore conceivable that the corresponding $\tilde{B}$-state level is shifted up in energy effectively closing this channel. This notion is consistent with the fact that in second-order deperturbation the level $\tilde{B}\,^2\Pi(v' = 12)$ is pushed up further to 56 899 cm^{-1}.

The $\tilde{D}$-$\tilde{X}$ spectra for NO–Ar reported by Miller and Cheng [67] and Tsuji *et al.* [69] are dominated by a long progression most likely in the stretching vibration. Although the observed vibrational frequency is very similar to the one found for the stretching vibration of the $\tilde{C}$-state, the dissociation energy derived from the observed red shift differs by more than a factor of two. In this respect, the system in the $\tilde{D}$-state resembles closely the strongly bound cation whose streching frequency (94 cm^{-1}) is substantially larger than the one found for the $\tilde{C}$-state (60 cm^{-1}) and the $\tilde{D}$-state (68 cm^{-1}). On the other hand, the expectation values for the radius of the Rydberg orbital in the two states are very similar (3.38 Å vs. 3.52 Å) [114]. Therefore, one would expect similar Rydberg behaviour for the interaction in these states.

Recently, Shafizadeh *et al.* proposed a global theoretical approach based on *ab-initio* calculations of the potential energy surfaces with A′ and A″ symmetry including configuration interaction [61]. For the NO–Ar complex, the study suggests that the monomer state $C\,^2\Pi$ forms a Renner–Teller pair split by about 4000 cm^{-1}. Furthermore, a strong interaction of the A′ component with the $D\,^2\Sigma$ state is predicted. The experimentally observed $\tilde{C}$-$\tilde{X}$ spectra are assigned to the A″ component. Owing to symmetry selection rules, this component cannot interact with the states correlating with the monomer state $D\,^2\Sigma$. The calculated spectrum has some resemblance with the observed spectra although details due to the rotational structure were not included. On the other hand, our rotational analysis is consistent with the pure C-state character of these bands as manifested by the presence of only two tensor components $T_0^{(0)}$ and $T_0^{(2)}$.

Additional theoretical work is clearly needed before the interaction involving these Rydberg states can be fully understood. In particular, a complete description should incorporate the interaction with the state $\tilde{B}\,^2\Pi$. Although this interaction was not included in the study [61], a global strategy for treating the excited states of the NO–X complexes is clearly the preferred choice. In particular, more accurate *ab-initio* calculations of the potential surfaces will be helpful in clarifying the electronic state character of the observed bands. Although the observed $\tilde{B}$-state and $\tilde{D}$-state band systems are very weak, new experimental spectra with improved resolution and signal-to-noise ratio will be extremely helpful. These should include spectra involving higher NO vibrational levels as well as complexes with different atomic partners.

5.5. *The 3d complex (NO–X, X=Ne, Ar):* $\tilde{F}\,^2\Delta, \tilde{H}\,^2\Sigma, \tilde{H}'^2\Pi, (\tilde{E}\,^2\Sigma)$

To date, (2 + 1) REMPI spectra involving electronic states correlating with the members of the 3d complex of the NO monomer have been observed only for NO–Ar [17] and for NO–Ne [70]. The spectroscopic constants and transition frequencies reported for the excited states of both complexes are summarized in tables 5 and 6. These tables contain also the data for the electronic ground state and the other Rydberg states discussed in the present article. Overview spectra of the wavelength region around 320 nm recorded on the appropriate parent cluster mass are shown in figure 22. The figure contains also the corresponding monomer spectrum recorded under similar molecular beam conditions. For the NO–Ne complex, spectra assigned to the states $\tilde{H}$ and $\tilde{F}$ are found to the red of the respective monomer transition. The $\tilde{F}$-state spectrum is shifted by 100 cm^{-1} to the red while the spectrum involving the

Table 5. Comparison of transition frequencies and spectroscopic constants (in cm^{-1}) for the different Rydberg states observed for the complex NO–Ar. See text for details.

State	NO	δ	r_{nl}(Å)	NO–Ar	ν_s	ν_b	D_0	Reference
$X\,^2\Pi$	0			0	20	15	88	[35]
$A\,^2\Sigma$	44 200	1.10	2.86	44 242	30	13/4	46	[111]
$C^2\Pi$	52 371	0.78	3.38	52 040	56	45	419	[17]
$D\,^2\Sigma$	53 292	0.74	3.52	52 338	69		1042	[69]
$F\,^2\Delta$	62 044	0.06	5.28	61 667	?	?	465	this work
$H'\,^2\Pi$	62 717	−0.02	5.65	61 940	82		865	this work
$E\,^2\Sigma$	60 864	1.19	6.27	60 364	78	57	588	[17]
NO^+	74 721			73 869	100	80	940	[116]

Table 6. Comparison of transition frequencies and spectroscopic constants (in cm^{-1}) for the different Rydberg states observed for the complex NO–Ne. Entries marked with an asterisk represent the result of an *ab-initio* calculation. See text for details.

State	NO	δ	r_{nl}(Å)	NO–Ne	ν_s	ν_b	D_0	Reference
$X\,^2\Pi$	0			0	15	8	35*	[36]
$A\,^2\Sigma$	44 200	1.10	2.86					
$C^2\Pi$	52 371	0.78	3.38	52 287	34	24	119	[67]
$D\,^2\Sigma$	53 292	0.74	3.52					
$F\,^2\Delta$	62 044	0.06	5.28	61 957	51	?	122	[70]
$H'\,^2\Pi$	62 717	−0.02	5.65	62 482	74	42	270	[70]
$E\,^2\Sigma$	60 864	1.19	6.27	60 738	50	39	161	[70]
$NO^+(X\,^1\Sigma)$	74 721				82*	41*	345*	[115]

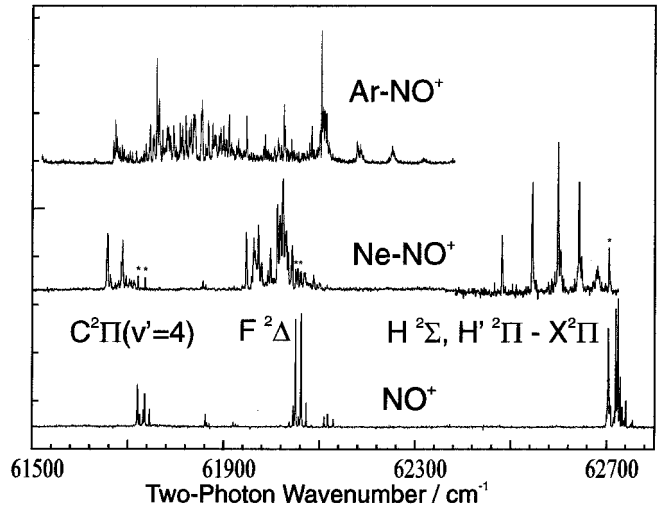

Figure 22. Overview spectrum for the region of excitation to the states derived from the 3d complex. The spectra are recorded by monitoring the appropriate parent ion mass.

$\tilde{H}$-state is shifted by about 200 cm^{-1}. The latter spectrum shows almost no rotationally resolved structure consistent with the fact that the corresponding monomer transition is dominated by a zeroth rank tensor component allowing only rotational Q-branches. The absence of extensive rotational structure indicates that the transition accesses mainly the Π-component. The observed spectrum is clearly dominated by a long vibrational progression assigned to the stretching vibration consistent with a substantial shortening of the NO–Ne bond. Using a simple Morse oscillator model, the determined harmonic and anharmonic constants suggest a binding energy of about 280 cm^{-1}. This value is in good agreement with the value 270 cm^{-1} derived from the experimentally observed red shift combined with the theoretical ground state dissociation energy $D_e = 35\,cm^{-1}$ of [36]. The comparison with the calculated bond energy $D_e = 345\,cm^{-1}$ of the corresponding NO^+–Ne complex [115] suggests that the interaction in the $\tilde{H}$-state is dominated by ionic interactions. This finding is consistent with the observed vibrational stretch and bend frequencies ($\nu_s = 74\,cm^{-1}$ and $\nu_b = 42\,cm^{-1}$) which are close to the values calculated in [115] for the ionic complex ($\nu_s = 82\,cm^{-1}$ and $\nu_b = 41\,cm^{-1}$). The observed Q-branches show a small splitting consistent with a deviation in the vibrationally averaged structure from the near T-shaped configuration. The deduced Jacobi angle of 60° is smaller than the value determined for the equilibrium configuration of the cation complex in the *ab-initio* calculation by Wright and co-workers [115]. In the case of NO–Ne, the band system located to the red of the X–F transition of the monomer is assigned to the excitation of the $\tilde{F}\,^2\Delta$ state. The structure of this band system is very different from the one found for other bands. Although no clear vibrational progression is obvious, we can distinguish two clumps of lines which might represent partially resolved rotational structure. So far the spectrum could only be analysed assuming two different vibrationally averaged structures corresponding to a near T-shaped configuration ($\theta = 85°$) and a near linear configuration ($\theta = 30°$) with an energy difference of about 5 cm^{-1}. The spectrum could then be reproduced assuming the excitation of two vibrational bands separated by 51 cm^{-1} most likely involving the intermolecular stretch coordinate. Considering the simplicity of the applied rigid rotor model, this assignment must be considered as tentative.

The spectrum in figure 22 also shows the intense band system involving the state $\tilde{C}\,^2\Pi(v' = 4)$ of NO–Ne. The corresponding band system for the NO–Ar complex is much weaker in intensity and shifted further to the red. An increased red shift is also observed for the band systems of NO–Ar involving the states $\tilde{F}$ and $\tilde{H}$. Unfortunately, the $\tilde{H}$-state is shifted so far to the red that it overlaps the band system correlating with the F-state. Furthermore, the spectrum exhibits very complicated rovibronic structure, so that we have not yet succeeded in analysing its rotational structure. On the other hand, the comparison in figure 23 of the one-colour REMPI spectrum (shifted to the red by 3724 cm^{-1}) with new IR-REMPI double resonance spectra is very revealing. Two IR-REMPI spectra are shown in the top part of the figure. Spectrum (*b*) is recorded with the IR laser fixed to a frequency which excites the complex to the level NO($v = 2$) but without excitation of any intermolecular vibration. On the other hand, spectrum (*a*) is recorded with the IR laser tuned to a transition to the first intermolecular bending level. While the former spectrum is almost identical to the one-colour REMPI spectrum, the latter exhibits only strong lines in the region of the $\tilde{F}$-state. As a possible explanation, we suspect that the Franck–Condon factor for excitation to the $\tilde{H}$-state from the first bending level is

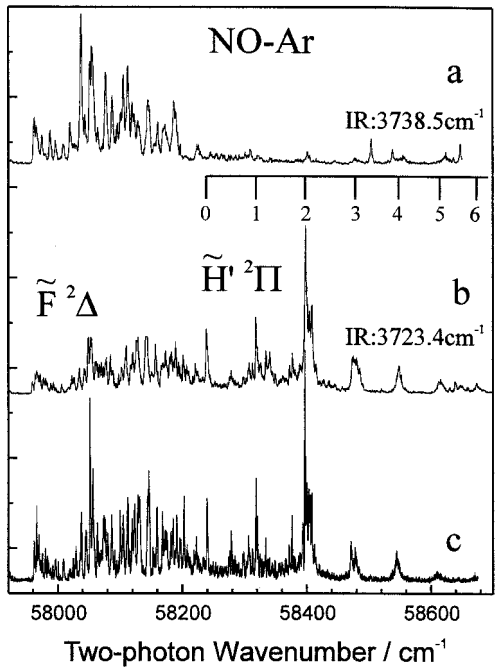

Figure 23. (2 + 1) REMPI spectrum of the $\tilde{X}$-$\tilde{F}$ and $\tilde{X}$-H transitions in NO(v'')-Ar. Spectrum (*c*) represents the one-colour REMPI spectrum for NO($v'' = 0$)-Ar shifted by 3724 cm^{-1}. The two top spectra are IR-REMPI double resonance spectra recorded at the indicated IR frequencies. Spectrum (*a*) is shifted 15 cm^{-1} to the blue. See text for details.

very small consistent with the assumption of a near T-shaped configuration similar to the one for the ground state. On the other hand, transitions to the $\tilde{F}$-state are allowed if this state strongly deviates from the T-shaped configuration so that the Franck–Condon factor with the first excited bending wavefunction of the ground state does not vanish. This gives some credibility to our results previously deduced for the NO–Ne complex (see above). If we accept this explanation, then we can assign the missing lines in the top spectrum of figure 23 to a progression in the stretch vibration of the $\tilde{H}$-state placing the origin at 61 940 cm^{-1}. Similar to the spectrum found for NO–Ne, the diffferent bands show almost no resolved rotational structure again consistent with a zeroth rank tensor component carrying the two-photon transition. The vibrational analysis yields a harmonic frequency of about 80 cm^{-1} and an anharmonicity constant of about 2 cm^{-1}. Using the Morse potential model, these data yield a dissociation energy consistent with the value of $D_0' = 867\,cm^{-1}$ derived from the experimental red shift. The first three members of the progression are very sharp and increase dramatically in intensity with increasing vibrational excitation indicating a substantial shortening of the intermolecular distance. Interestingly, higher members are very weak and broadened due to predissociation. The most likely mechanism is dissociation via the continuum of the $\tilde{F}$-state. A schematic view of the involved potentials is shown in figure 24. Using the bond energy for the $\tilde{F}$-state as derived from its red shift, we find that, in the absence of a barrier, dissociation becomes allowed for stretch levels $\tilde{H}(v' \geq 3)$ in perfect agreement with the experimental observation. Unfortunately the rotational analysis

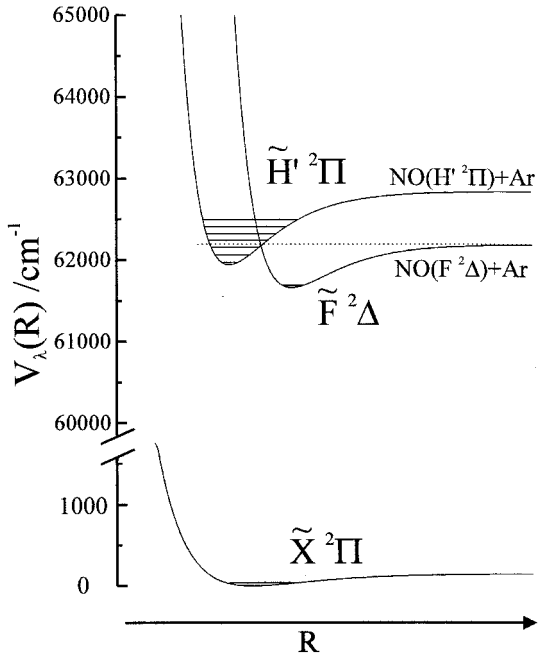

Figure 24. Schematic of the potential energy curves and vibrational levels for the states $\tilde{F}$ and $\tilde{H}$ for the NO–Ar complex.

of the $\tilde{F}$-state has not yet been achieved. It is even doubtful if the rigid rotor model will be suitable for this situation. If, as the IR-REMPI spectrum suggests, the $\tilde{F}$-state has a vibrationally averaged structure which deviates considerably from the T-shaped configuration, we expect intense transitions to excited bending levels. In this case the hindered rotor description is clearly the preferred model [86].

Because of the large quantum defect of the $(n+1)\sigma$ orbitals, there is a near resonance with the ndσ orbital resulting in a strong interaction of the associated states due to l-uncoupling [106]. Therefore, the H-state derived from the 3d complex interacts strongly with the second member of the ns Rydberg series: E $^2\Sigma$ and it is appropriate to discuss the associated states of the complexes in this context as well. Band systems in the vicinity of the E-state have been measured for complexes with Ne [70], Ar [17, 71], and Kr [117]. The spectra show some rotational structure which could be analysed in terms of the rigid rotor model. The analysis of the spectra for NO–Ar and NO–Ne indicates a vibrationally averaged structure close to the one predicted for the cationic complex. On the other hand, the vibrational frequencies and dissociation energies are significantly lower than found or predicted for the ionic species.

The presently available spectroscopic information on the different Rydberg states of the NO–Ar and NO–Ne complexes is compiled in tables 5 and 6. The tables contain also the expectation values r_{nl} for the size of the Rydberg orbitals calculated according to equation (90) and the quantum defect $\delta = n - n^*$ where n^* is determined from equation (89). The data clearly suggest the transition from dispersion dominated interaction for the weakly bound $\tilde{A}$-state to predominantly ionic interaction for the $\tilde{H}$-state. Nevertheless, several points are surprising and warrant further discussion.

(1) The great similarity in Rydberg character for the states of the 3p complex clearly contrasts the spectroscopic information accumulated for the corresponding states of the complexes with Ar and Ne. In the case of NO–Ar, the data indicate a binding energy larger than the one observed for the cation complex while the vibrational progression (possibly in the stretch coordinate) is consistent with a frequency similar to the one observed for the $\tilde{C}$-state.

(2) According to the size of the Rydberg orbitals, we expect for the states derived from the 3d complex a behaviour similar to the cationic complex. These expectations are only borne out for the Π component of the $\tilde{H}$-state. The band systems assigned to the $\tilde{H}$-state approach the cation limit for NO–Ar as well as for NO–Ne. Binding energies and vibrational frequencies agree within 20% with the corresponding values for $Ar–NO^+$ and $Ne–NO^+$, respectively. Constants for the $\tilde{F}$-states differ considerably from the values of the ionic complex. For example, the dissociation energies are smaller by more than a factor of two or three. In this context, it is interesting to include the results for the $\tilde{E}$-state. Although the Rydberg orbital is considerably larger, we find potential parameters very similar to the ones found for the $\tilde{F}$-state. In conclusion, the interaction in these Rydberg states must be very sensitive to the spatial orientation of the orbital as well as its spatial extent. For example, electrons occupying orbitals with significant s-character can penetrate deep into the core causing more efficient screening of the ionic core than electrons residing in highly aligned orbitals. Along this line of reasoning, we can understand the strong bindings in the observed Rydberg states with dominant Π-character. For the states $\tilde{C}$ and $\tilde{H}$, the observed bands are most likely due to excitation to the antisymmetric component (A''). In this case, the electron distribution is concentrated above and below the molecular plane exposing the ionic core to the atom even when the radius is smaller or comparable to the van der Waals radius.

6. Conclusions

In this article, we have reviewed the status of the spectroscopic characterization of the NO–Rg systems in their ground and excited states. While the information on the ground state interaction relied in the past mainly on scattering data, the application of IR-REMPI double resonance techniques has enabled us to measure different bend–stretch intermolecular vibrational levels with rotational resolution for the first time. Because the observed spectra are extremely sensitive to details of the potential surfaces, they provide a very sensitive test for current *ab-initio* treatments of these systems. Potential surfaces for NO–Ar and NO–Ne calculated at the CCSD(T) level are highly accurate predicting bound level energies within a fraction of a wavenumber. Additional physical insight is provided by using an empirical Hamiltonian describing the complexes as near symmetric tops with electronic structure.

Complexes involving NO are also of great interest because of the variety of electronically excited states of the NO monomer. While the experimental data for the ground state NO–X systems are well reproduced by *ab-initio* treatments, the situation for the excited states of these systems is clearly less advanced. The breakdown of the Born–Oppenheimer approximation further adds to the difficulties

resulting in the strong interaction of different electronic states. On the other hand, the observed spectra are simple enough that they provide important benchmarks for the study of molecular interactions in excited states of small systems. Naturally, full *ab-initio* treatments of these excited states should be the next step in the theoretical treatment of these systems. From an experimental point of view, we are still lacking information on the band systems involving higher NO vibrational excitation as well as information about states involving higher Rydberg states. These data will be important in identifying non-adiabatic effects and, in particular, complexation-induced changes in the electronic state mixing. Finally, complexes with other rare gases and with small molecules should represent the targets for future work.

Acknowledgements

We would like to thank Professor M. H. Alexander, Professor P. J. Dagdigian, and Professor T. G. Wright for many fruitful and stimulating discussions on the subject of this article. Professor M. H. Alexander kindly provided us with the results of the bound state calculation for NO–Ar and NO–Ne. Professor T. Heil deserves special thanks for stimulating the authors' interest in the application of concepts of classical mechanics towards the derivation of quantum mechanical Hamiltonians. Financial support from the National Science Foundation (grant CHE-9707670) is gratefully acknowledged.

References

[1] *Faraday Discuss. chem. Soc.*, 1982, **73**; 1994, *ibid.*, **97**.
[2] *Chem. Rev.*, 1988, **88**; 1994, *ibid.*, **94**; 2000, *ibid.*, **100**.
[3] Halberstadt, N., and Janda, K. C. (editors), 1990, *Dynamics in Polyatomic van der Waals Complexes* (New York: Plenum).
[4] Nesbitt, D. J., 1994, *A. Rev. phys. Chem.*, **45**, 367.
[5] Bacic, Z., and Miller, R. E., 1996, *J. phys. Chem.*, **100**, 12945.
[6] Heaven, M. C., 1992, *A. Rev. phys. Chem.*, **43**, 283.
[7] Heaven, M. C., 1993, *J. phys. Chem.*, **97**, 8567.
[8] Carter, C. C., Lee, H. S., McCoy, A. B., and Miller, T. A., 2000, *J. molec. Struct.*, **525**, 1.
[9] Meyer, H., 1995, *J. chem. Phys.*, **102**, 3110.
[10] Meyer, H., 1994, *J. chem. Phys.*, **101**, 6686.
[11] Meyer, H., 1994, *J. chem. Phys.*, **101**, 6697.
[12] Meyer, H., 1995, *J. phys. Chem.*, **99**, 1101.
[13] Meyer, H., 1995, *Molec. Phys.*, **84**, 1155.
[14] Meyer, H., 1994, *Chem. Phys. Lett.*, **230**, 510.
[15] Meyer, H., 1995, *J. chem. Phys.*, **102**, 3151.
[16] Meyer, H., 2001, Counterpropagating pulsed molecular beam scattering, in *Atomic & Molecular Beams: The State of the Art 2000*, edited by R. D. Campargue (Berlin: Springer).
[17] Meyer, H., 1997, *J. chem. Phys.*, **107**, 7732.
[18] Kim, Y, Fleniken, J., and Meyer, H., 1999, *J. phys. Chem. A.*, **103**, 6327.
[19] Nielson, G. C., Parker, G. A., and Pack, R. T., 1976, *J. chem. Phys.*, **64**, 2055.
[20] Nielson, G. C., Parker, G. A., and Pack, R. T., 1977, *J. chem. Phys.*, **66**, 1396.
[21] Green, S., and Zare, R. N., 1977, *Chem. Phys.*, **7**, 62.
[22] Alexander, M. H., 1982, *J. chem. Phys.*, **76**, 5974.
[23] Alexander, M. H., 1985, *Chem. Phys.*, **92**, 337.
[24] Orlikowski, T., and Alexander, M. H., 1983, *J. chem. Phys.*, **79**, 6006.
[25] Corey, G. C., and Alexander, M. H., 1986, *J. chem. Phys.*, **85**, 5652.
[26] Alexander, M. H., 1993, *J. chem. Phys.*, **99**, 7725.
[27] Yang, M., and Alexander, M. H., 1995, *J. chem. Phys.*, **103**, 6973.

[28] Islam, M., Smith, I. W. M., and Alexander, M. H., 1999, *Chem. Phys. Lett.*, **305**, 311.
[29] Orlikowski, T., and Alexander, M. H., 1984, *J. chem. Phys.*, **80**, 1506.
[30] Orlikowski, T., and Alexander, M. H., 1984, *J. chem. Phys.*, **80**, 4133.
[31] Alexander, M. H., 1999, *J. chem. Phys.*, **111**, 7426.
[32] Alexander, M. H., 1999, *J. chem. Phys.*, **111**, 7435.
[33] Lee, E. P. F., and Wright, T. G., 1998, *J. chem. Phys.*, **109**, 157.
[34] Klos, J., Chalasinski, G., Berry, M. T., Bukowski, R., and Cybulski, S. M., 2000, *J. chem. Phys.*, **112**, 2195.
[35] Kim, Y., Fleniken, J., Meyer, H., Dagdigian, P. J., and Alexander, M. H., 2000, *J. chem. Phys.*, **113**, 73.
[36] Alexander, M. H., Soldan, P., Wright, T. G., Kim, Y., Meyer, H., Dagdigian, P. J., and Lee, E. P. F., 2001, *J. chem. Phys.*, **114**, 5588.
[37] Thuis, H., Stolte, S., and Reuss, J., 1979, *Chem. Phys.*, **43**, 351.
[38] Thuis, H., Stolte, S., Reuss, J., van den Biesen, J. J. H., and van den Meijdenberg, C. J. N., 1980, *Chem. Phys.*, **52**, 211.
[39] Keil, M., Slankas, J. T., and Kupperman, A., 1979, *J. chem. Phys.*, **70**, 541.
[40] Casavecchia, P., Lagana, A., and Volpi, G. G., 1984, *Chem. Phys. Lett.*, **112**, 445.
[41] Beneventi, L., Casavecchia, P., and Volpi, G. G., *J. chem. Phys.*, **85**, 7011.
[42] Sudbo, A. S., and Loy, M. M. T., 1982, *J. chem. Phys.*, **76**, 3646.
[43] Andresen, P., Joswig, H., Pauly, H., and Schinke, R., 1982, *J. chem. Phys.*, **77**, 2204.
[44] Joswig, H., Andresen, P., and Schinke, R., 1986, *J. chem. Phys.*, **85**, 1904.
[45] Jons, S. D., Shirley, J. E., Vonk, M. T., Giese, C. F., and Gentry, R. W., 1992, *J. chem. Phys.*, **97**, 7831.
[46] Jons, S. D., Shirley, J. E., Vonk, M. T., Giese, C. F., and Gentry, R. W., 1996, *J. chem. Phys.*, **105**, 5397.
[47] Lin, A., Antonova, S., Tsakotellis, A. P., and McBane, G. C., 1999, *J. phys. Chem.*, **103**, 1198.
[48] Alexander, M. H., and Stolte, S., 2000, *J. phys. Chem.*, **112**, 8017.
[49] James, P. L., Sims, I. R., Smith, I. M. W., Alexander, M. H., and Yang, M., 1998, *J. chem. Phys.*, **109**, 3882.
[50] Alexander, M. H., 1999, *Faraday Discuss*, **113**, 437.
[51] Drabbels, M., Wodtke, A. M., Yang, M., and Alexander, M. H., 1997, *J. phys. Chem. A*, **101**, 6463.
[52] Klos, J., Chalasinski, G., Berry, M. T., Bukowski, R., and Cybulski, S. M., 2000, *J. chem. Phys.*, **112**, 2195.
[53] Suits, A. G., Bontuyan, L. S., Houston, P. L., and Whitaker, B. J., 1992, *J. chem. Phys.*, **96**, 8618.
[54] Bontuyan, L. S., Suits, A. G., Houston, P. L., and Whitacker, B. J., 1993, *J. phys. Chem.*, **97**, 6342.
[55] Yonekura, N., Gebauer, C., Kohguchi, H., and Suzuki, T., 1999, *Rev. scient. Instrum.*, **70**, 3265.
[56] Novick, S. E., Davies, P. B., Dyke, T. R., and Klemperer, W., 1973, *J. Am. chem. Soc.*, **95**, 8547.
[57] Langridge-Smith, P. R. R., Carrasquillo, E., and Levy, D. H., 1981, *J. chem. Phys.*, **74**, 6513.
[58] Miller, J. C., 1989, *J. chem. Phys.*, **90**, 4031.
[59] Tsuji, K., Shibuya, K., and Obi, K., 1994, *J. chem. Phys.*, **100**, 5441.
[60] McQuaid, M. J., Lemire, G. W., and Sausa, R. C., 1994, *Chem. Phys. Lett.*, **227**, 54.
[61] Shafizadeh, N., Brechignac, Ph., Dyndgaard, M., Fillion, J. H., Gauyacq, D., Levy, B., Miller, J. C., Pino, T., and Raoult, M., 1998, *J. chem Phys.*, **108**, 9313.
[62] Mack, P., Dyke, J. M., and Wright, T. G., 1998, *J. chem. Soc. Faraday Trans.*, **94**, 629.
[63] Mils, P. D. A., Western, C. M., and Howard, B. J., 1986, *J. phys. Chem.*, **90**, 3331.
[64] Mills, P. D. A., Western, C. M., and Howard, B. J., 1986, *J. phys. Chem.*, **90**, 4961.
[65] Kim, Y., Patton, K., Fleniken, J., and Meyer, H., 2000, *Chem. Phys. Lett.*, **318**, 522.

[66] Sato, K., Achiba, Y., and Kimura, K., 1984, *J. chem. Phys.*, **81**, 57.
[67] Miller, J. C., and Cheng, W. C., 1985, *J. phys. Chem.*, **89**, 1647.
[68] Miller, J. C., 1987, *J. chem. Phys.*, **86**, 3166.
[69] Tsuji, K., Aiuchi, K., Shibuya, K., and Obi, K., 1998, *Chem. Phys.*, **231**, 279.
[70] Fleniken, J., Kim, Y., and Meyer, H., 1998, *J. chem. Phys.*, **109**, 8940.
[71] Tsuji, K., Shibuya, K., and Obi, K., 1995, *Laser Chem.*, **15**, 157.
[72] Chergui, M., and Schwentler, N., 1992, *J. chem. Phys.*, **97**, 2881.
[73] Suzuki, T., Katayanagi, H., and Suzuki, T., 1997, *J. phys. Chem. A*, **101**, 6697.
[74] Cockett, M. C. R., 1998, *J. Electron. Spectros.*, **97**, 171.
[75] Bosenberg, W. R., and Guyer, D. R., 1992, *Appl. Phys. Lett.*, **61**, 387.
[76] Bosenberg, W. R., and Guyer, D. R., 1993, *J. opt. Soc. Am. B*, **10**, 1716.
[77] Pribble, R. N., and Zwier, T. S., 1994, *Faraday Discuss*, **97**, 229.
[78] Matsumoto, Y., Ebata, T., and Mikami, N., 1998, *J. chem. Phys.*, **109**, 6303.
[79] Amiot, C., Bacis, R., and Guelachvili, G., 1978, *Can. J. Phys.*, **56**, 251.
[80] Meyer, H., 1997, *J. chem. Phys.*, **107**, 7721.
[81] Fleniken, J., Kim, Y., and Meyer, H., 2000, *Chem. Phys. Lett.*, **318**, 529.
[82] Dubernet, M. L., Flower, D., and Hutson, J. M., 1991, *J. chem. Phys.*, **94**, 7602.
[83] Dubernet, M. L., Tuckey, P. A., and Hutson, J. M., 1992, *Chem. Phys. Lett.*, **193**, 355.
[84] Green, W. H., and Lester, M. I., 1992, *J. chem. Phys.*, **96**, 2573.
[85] Chakravarty, C., and Clary, D. C., 1991, *J. chem. Phys.*, **94**, 4149.
[86] Hutson, J. M., 1991, *Advances in Molecular Vibrations and Collision Dynamics*, vol. IA, edited by J. M. Bowman and M. A. Ratner (Greenwich, CT: JAI), p. 1.
[87] Kroto, H. W., 1992, *Molecular Rotation Spectra* (New York: Dover).
[88] Podolsky, B., 1928, *Phys. Rev.*, **32**, 812.
[89] Bunker, P. R., 1979, *Molecular Symmetry and Spectroscopy* (San Diego: AP), chap. 7.
[90] Hougen, J. T., 1962, *J. chem. Phys.*, **36**, 519.
[91] Watson, J. K. G., 1970, *Molec. Phys.,* **119**, 465.
[92] Howard, B. J., and Moss, R. E., 1971, *Molec. Phys.*, **20**, 147.
[93] Holmgren, S. L., Waldman, W., and Klemperer, W., 1977, *J. chem. Phys.*, **67**, 4414.
[94] Alexander, M. H., Gregurick, S., and Dagdigian, P. J., 1994, *J. chem. Phys.*, **101**, 2887.
[95] Lefebvre-Brion, H., and Field, R. W., 1986, *Perturbations in the Spectra of Diatomic Molecules* (New York: Academic).
[96] Tennyson, J., and Sutcliff, B. T., 1982, *J. chem. Phys.*, **77**, 4061.
[97] Brocks, G., van der Avoird, A., Sutcliff, B. T., and Tennyson, J., 1983, *Molec. Phys.*, **50**, 1025.
[98] Schmelz, T., Rosmus, P., and Alexander, M. H., 1994, *J. chem. Phys.*, **98**, 1073.
[99] Chang, B. C., Yu, L., Cullin, D., Rehfuss, B., Williamson, J., Miller, T. A., Fawzy, W. M., Zheng, X., Fei, S., and Heaven, M., 1991, *J. chem. Phys.*, **95**, 7086.
[100] Fawzy, W. M., and Hougen, J. T., 1989, *J. Molec. Spectrosc.*, **137**, 154.
[101] Yang, M., Alexander, M. H., Gregurick, S., and Dagdigian, P. J., 1995, *J. chem. Phys.*, **102**, 2413.
[102] Zare, R. N., 1988, *Angular Momentum: Understanding Spatial Aspects in Chemistry and Physics* (New York: Wiley).
[103] Kim, Y., Fleniken, J., and Meyer, H., 2001, *J. chem. Phys.*, **114**, 5578.
[104] Fawzy, W. M., Fraser, G. T., Hougen, J. T., and Pine, A. S., 1990, *J. chem. Phys.*, **93**, 2992.
[105] Miescher, E., and Huber, K. P., 1973, *Int. Rev. Sci., Phys. Chem. Ser. 2*, Vol. 3, edited by A. D. Buckingham and D. A. Ramsey (London: Butterworths), p. 37.
[106] Jungen, Ch., 1970, *J. chem. Phys.*, **53**, 4168.
[107] Huber, K. P., and Herzberg, G., 1979, *Molecular Spectra and Molecular Structure IV, Constants of Diatomic Molecules* (New York: Van Nostrand Reinhold).
[108] Lagerquist, A., and Miescher, E., 1958, *Helv. phys. Acta*, **31**, 221.
[109] Fredine, S., Gauyacq, D., Horani, M., Jungen, Ch., and Masnou-Seeuws, F., 1987, *Molec. Phys.*, **60**, 825.
[110] Pratt, S. T., Jungen, Ch., and Miescher, E., 1989, *J. chem. Phys.*, **90**, 5971.

[111] Lozeille, J., Gamblin, S. D., Daire, S. E., Wright, T. G., and Smith, D. M., 2000, *J. chem. Phys.*, **113**, 7224.
[112] Wright, T. G., Lozeille, J., Carter, C. C., and Miller, T. A., 2000, Abstract FA02, 55th Ohio State University International Symposium on Molecular Spectroscopy.
[113] Mack, P., Dyke, J. M., Smith, D. M., Wright, T. G., and Meyer, H., 1998, *J. chem. Phys.*, **109**, 4361.
[114] Barr, J. D., Dyke, J. M., Smith, D. M., and Wright, T. G., 1998, *J. Electron Spectros.*, **97**, 159.
[115] Lee, E. P. F., Soldan, P., and Wright, T. G., 1998, *J. phys. Chem. A*, **102**, 6858.
[116] Takahashi, M., 1992, *J. chem. Phys.*, **96**, 2594.
[117] Wright, T. G., Private communication.